Winter 12-22-2009

Spectroscopy and Energy Transfer of Molecular Transients: Hydrogen Isocyanide and the Ketenyl Radical

Michael J. Wilhelm
University of Pennsylvania, wilhelm@sas.upenn.edu

Recommended Citation

Wilhelm, Michael J., "Spectroscopy and Energy Transfer of Molecular Transients: Hydrogen Isocyanide and the Ketenyl Radical" (2009). *Publicly Accessible Penn Dissertations*. 75.
http://repository.upenn.edu/edissertations/75

Spectroscopy and Energy Transfer of Molecular Transients: Hydrogen Isocyanide and the Ketenyl Radical

Abstract

Energy transfer from molecular species has been a long standing topic of profound interest to the chemical physics community. It is worth noting however, that to date, most studies have preferentially focused on chemically stable molecular species. While the literature does contain numerous examples of energy transfer of small radical or chemically unstable species, there have been extremely few studies which have actually probed highly vibrationally excited species. This apparent lack of attention should not be confused with a lack of interest. On the contrary, given the prevalence of vibrationally excited radicals in complex chemical systems such as planetary atmospheres and combustion, it is highly desirable to gain a complete understanding of the energetic deactivation processes of these delicate species. More often than not, the limiting factor which prevents examination of such species is a lack of spectroscopic information which is necessary for the identification as well as modeling of the corresponding species.

In this thesis, we explore the use of time-resolved Fourier transform infrared emission spectroscopy, coupled with ab initio quantum chemical calculations, as a means of characterizing the vibrationally excited energy transfer dynamics from hydrogen isocyanide (HNC) as well as the ketenyl (HCCO) radical. It has been determined that each of these radical species can be generated in appreciable relative concentrations and with excess internal energy, following the 193 nm photolysis of specific stable molecular precursors. Through variation of the associated inert atomic collider species, and repeated spectral fitting analysis, it becomes feasible to obtain a measure the time-resolved average internal energy (as a function of the collider species), and hence a measure of the vibrational energy transfer efficiency of each radical species. It is observed that both HNC and HCCO exhibit enhanced vibrational energy transfer, for all average internal energies, relative to comparably sized stable molecular species. The roles and associated benefits of enhanced energy transfer of these radical species, to combustion chemistry (HCCO) as well as the interstellar medium (HNC), will be discussed.

Degree Type
Dissertation

Degree Name
Doctor of Philosophy (PhD)

Graduate Group
Chemistry

First Advisor
Hai-Lung Dai

Keywords
Energy transfer, photodissociation, radical spectroscopy, hydrogen isocyanide (HNC), ketenyl radical (HCCO), IR emission spectroscopy

Subject Categories
Physical Chemistry

SPECTROSCOPY AND ENERGY TRANSFER OF MOLECULAR TRANSIENTS: HYDROGEN ISOCYANIDE AND THE KETENYL RADICAL

Michael James Wilhelm

A Dissertation
In
Chemistry

Presented to the Graduate Faculties of the University of Pennsylvania
in
Partial Fulfillment of the Requirements for the
Degree of Doctor of Philosophy

2009

Professor Hai-Lung Dai: Supervisor of Dissertation

Professor Gary Molander: Graduate Group Chairperson

Dissertation Committee:
Professor Marsha Lester: Committee Chair
Professor Robin Hochstrasser: Reader
Professor Michael Topp: Reader

For my wife Justine.

Who, for the last few years, has patiently endured the uncommonly unique lifestyle that comes with being married to a graduate student.

Acknowledgments:

First and foremost, I wish to express my sincerest gratitude to my mentor and advisor, Hai-Lung Dai. I am most thankful for the independence he allowed me in all aspects of my research. While always ready with suggestions and challenges, Hai-Lung simply refused to dictate the course of my research (and by extension my thesis), forcing me to think for myself. In the end, he was successful in producing a scientist, rather than a clone.

Additionally, I wish to thank the members of my dissertation committee. Specifically, Professors Marsha Lester, Michael Topp, and Robin Hochstrasser for the many suggestions and challenges which were raised during my annual committee meetings, as well as the numerous thoughtful comments addressed in this thesis. Furthermore, in addition to Professors Andrew Rappe, Jeffery Saven, Feng Gai, and Arjun Yodh, all three members of my committee, at one point or another, also served as professors for my coarse work at Penn. I am grateful for the rigor and intensity that was universally applied to every lecture, whose lessons greatly aided my research.

I would also like make special mention of Drs. Matthew Tucker and Sara Mason, who served as personal mentors during my first year at Penn. Their guidance and friendship during that formidable transition period made all the difference, and I am forever indebted to them for that.

I also wish to thank the members of the Dai group, both past and present, who provided a welcoming work environment over the last six years. In particular, many of the experiments described within this thesis would not have been possible, or at least not nearly as successful, without the technical brilliance of Matthew Nikow in the laboratory. Additionally, I would like to thank Professor Jonathan Smith for mentoring and nurturing my interest in scientific (and basic) programming and for the numerous helpful discussions during the course of the energy transfer work. As well, I am grateful for the education I gained from daily conversations within the Dai group, both scientific and otherwise, with Grazia Gonella, Min Zhang, Jianqiang Ma, Jia Zeng, Wei Gan, Rosa (Yi-Hsuan) Chou, Jun Han, Susan Dounce, Shih-Hui Jen, Heather Eckenrode, James Garmirian, Tom Rockey, Laura Letendre, and William McNavage.

Last, but certainly not least, I wish to express my sincerest gratitude for the support from my family. In particular, to my parents James and Joan Wilhelm, as well as my brother Matthew and my sister Elizabeth, whose unending encouragement throughout my life made graduate studies a possibility. Finally, I absolutely must thank my wife Justine. Who, perhaps more than most, was made to endure the unpredictable lifestyle of graduate school. For her enduring patience and encouragement in all phase of my time at Penn, I am grateful.

ABSTRACT

SPECTROSCOPY AND ENERGY TRANSFER OF MOLECULAR TRANSIENTS: HYDROGEN ISOCYANIDE AND THE KETENYL RADICAL

Michael James Wilhelm

Hai-Lung Dai

Energy transfer from molecular species has been a long standing topic of profound interest to the chemical physics community. It is worth noting however, that to date, most studies have preferentially focused on chemically stable molecular species. While the literature does contain numerous examples of energy transfer of small radical or chemically unstable species, there have been extremely few studies which have actually probed highly vibrationally excited species. This apparent lack of attention should not be confused with a lack of interest. On the contrary, given the prevalence of vibrationally excited radicals in complex chemical systems such as planetary atmospheres and combustion, it is highly desirable to gain a complete understanding of the energetic deactivation processes of these delicate species. More often than not, the limiting factor which prevents examination of such species is a lack of spectroscopic information which is necessary for the identification as well as modeling of the corresponding species.

In this thesis, we explore the use of time-resolved Fourier transform infrared emission spectroscopy, coupled with ab initio quantum chemical calculations, as a means of characterizing the vibrationally excited energy transfer dynamics from hydrogen isocyanide (HNC) as well as the ketenyl (HCCO) radical. It has been determined that each of these radical species can be generated in appreciable relative concentrations and with excess internal energy, following the 193 nm photolysis of specific stable molecular precursors. Through variation of the associated inert atomic collider species, and repeated spectral fitting analysis, it becomes feasible to obtain a measure the time-resolved average internal energy (as a function of the collider species), and hence a measure of the vibrational energy transfer efficiency of each radical species. It is observed that both HNC and HCCO exhibit enhanced vibrational energy transfer, for all average internal energies, relative to comparably sized stable molecular species. The roles and associated benefits of enhanced energy transfer of these radical species, to combustion chemistry (HCCO) as well as the interstellar medium (HNC), will be discussed.

Table of Contents:

List of Tables:

Chapter 2:

Chapter 3:

Chapter 5:

***Chapter 6*:**

List of Figures:

***Chapter 1*:**

***Chapter 2*:**

***Chapter 3*:**

***Chapter 4*:**

***Chapter 5*:**

***Chapter 6*:**

Chapter 1

Time-Resolved Fourier Transform Infrared Emission Spectroscopy: Photodissociation Dynamics, Molecular Transients, and Energy Transfer

1.1 INTRODUCTION

The literature out of the chemical physics community over the last century is filled with numerous experimental and theoretical investigations, including countless review articles, focusing on the various mechanisms and efficiencies of molecular energy transfer [1]. In particular, there has been much interest in aromatic ring systems [1] at high internal energies as well as smaller di- and triatomic systems near the vibrational ground state [2]. One common theme throughout, is that most of the species examined have been chemically stable molecules. Radical species (or molecular transients), on the other hand, have received considerably less attention and are *typically* only ever probed in the lowest vibrational levels [3].

We note in passing that the definition of radical used throughout this thesis is modeled after that which was put forth by Gerhard Herzberg in his seminal text on radical spectroscopy [4]. Specifically, we define the term *radical* to mean any molecular species which has a fleeting existence under normal laboratory conditions. In other words, radicals are short lived molecules which may be either chemically (i.e. reactive) or physically ($E_{in} > D_e$) unstable [4]. It is often the case, particularly within organic chemistry circles, that radicals are defined as any chemical species possessing an unpaired electron (i.e. $S > 0$). However, as was pointed out by Herzberg [4], such a definition begins to run into trouble even for simple diatomic species such as O_2 (stable) and C_2 (unstable). Under this scheme, depending upon the occupied electronic state, either species (O_2 and C_2) could justifiably be characterized as both a radical ($S > 0$) and a non-radical ($S = 0$). More interestingly, species which exhibit electronic mixing could arguably be said to be composed of fractional radical character. In an effort to avoid such inconsistencies, we choose to adopt a working definition of *radical* that is more in line with that of a *molecular transient*; describing a short-lived molecular species regardless of the associated spin of the species.

It is important to note that the limited number of energy transfer studies involving radical species is not indicative of a lack of interest. On the contrary, given the ubiquitous presence of radicals in natural chemical systems such as combustion, the atmosphere, and the interstellar medium, it is highly desirable to obtain information regarding both the spectroscopic and dynamic signatures of the relevant species. The most prevalent issue associated with the study of radicals lies in the notion that they are typically very reactive (i.e. chemically unstable), and are often generated in low relative concentrations [4]. In this regard, it has historically been very difficult to experimentally characterize this class of species. Nevertheless, given the often exotic electronic properties of radical systems, it is possible that they could exhibit unique energy transfer behaviors. For example, it is reasonable to expect that the presence of an unpaired electron (or lone-pair set of electrons) could result in an enhanced attractive interaction between a donor and collider species, potentially yielding a weakly bound complex. The formation of such a collision complex suggests a longer lived collisional interaction and thus could manifest as an apparent enhancement of energy transfer efficiency.

1.2 ON ENERGY TRANSFER AND THE SPECTROSCOPY OF RADICALS

This laboratory has a well documented history of studying energy transfer as well as characterizing the vibrational spectral signatures of radicals [5-20]. In both cases, the associated species of interest are generated with ro-vibrational excitation in either of two ways: direct ultra-violet (UV) optical pumping in the case of energy transfer [5-13], and photodissociation of a specifically chosen molecular precursor for the generation and excitation of a desired radical species [14-20]. Regardless of the given experimental goal, the excited species are generated in the presence of a large backing pressure of an *inert* quenching species, typically 2-4 Torr of Ar relative to 1-10 mTorr of the species of interest, so as to induce collisional deactivation. Over time, the deactivation process causes the excited state population to cascade down the associated ro-vibrational manifold, and concurrently results in the emission of infrared (IR) photons whose energies reflect the potential energy surface (PES) of the associated species.

Given that the key observable, for both experiments, is an energetically evolving source of IR photons, time-resolved Fourier transform infrared emission spectroscopy (TR-FTS) serves as an ideal method for collecting the resulting IR radiation. In particular, TR-FTS (run in step-scan mode so as to allow for ns-μs temporal resolution) is used to record a series of time-resolved IR emission spectra which are characteristic of the energetic evolution of the excited molecule(s) of interest. Furthermore, TR-FTS is especially effective for the collection of IR emission following a photodissociation event in which there are typically numerous IR emitting species generated. As an example, in chapter 5 of this thesis we will find that the 193 nm photolysis of vinyl cyanide results in four main dissociation pathways, yielding *eight* distinct IR emitting species. The profound utility of TR-FTS for such a system resides in the notion that all transition frequencies (depending upon the frequency range of the detector employed) are collected at once, allowing for a complete characterization of a given photolysis system.

In a typical TR-FTS experiment, the resulting series of time-resolved IR spectra are characterized as exhibiting a number of features originating predominantly from the fundamental vibrational modes of the excited molecular species. At early times, when the prepared populations contain the highest internal energies, the observable features are often very intense and typically very broad. Additionally, depending upon the amount of internal energy and the degree of anharmonicity of the associated vibrational modes, the centers of the allowed transition frequencies are often observed to be shifted away from the fundamental frequencies to lower energies. As time progress however, and the relative number of collision events increases, both the intensity and spectral width of the resulting features begin to decrease. As well, contingent upon both the internal energy and anharmonicity of the various modes, the features begin to shift higher in energy towards the associated fundamental transition frequencies. At later times, typically following 15-25 μs (with an associated backing pressure of 4 Torr of Ar), the spectral features arrive at the fundamental transition frequencies and (as the vibrationally excited population decreases) the intensities of the features begin to decrease. For instance, it is observed that the ν_1 CH stretch mode of HCCO, when generated following the 193 nm photolysis of ethyl ethynyl ether, has a nascent transition band center frequency around 3100 cm^{-1}, and shifts to the fundamental at 3232 cm^{-1} upon collisional quenching.

For the characterization of the vibrational spectral signature of radicals, it is of interest to note that typically only the later time (i.e. low internal energy) spectra, near the vicinity of the associated $\nu_i : 0 \leftarrow 1$ transitions, which are employed in the final spectral analysis [14-20]. Granted, the rise time and associated decay profiles, obtained from all of the collected spectra, are actually used to positively identify primary dissociation fragments as well as confirm common origins for the observed spectral features. Nevertheless, in terms of the characterization of the actual IR signature of the radical, only the latest time spectra (after the various features have stopped shifting) are actually considered in the final analysis of the fundamental transition frequencies. The earlier time spectra, which contain a wealth of information regarding the excited vibrational state transitions of the radical, are usually discarded altogether [14,16-18].

Alternatively, in the case of energy transfer studies, each of the collected time-resolved spectra are examined with equal importance [5-13]. More to the point, each individual spectrum contains information regarding the population distribution and hence the average internal energy content of the species of interest. In this regard, one could easily argue that the earliest time spectra (associated with the highest internal energies) are of the greatest importance. However, in order to successfully obtain the encoded information concerning the average internal energies, it is necessary to fit the observed (excited) emission spectra, and hence requires quantitative information concerning the anharmonicities of the observed vibrational modes. Stable molecular species, typically containing less than four or five atoms, have historically been employed as fruitful laboratories to model much of the complexity of chemistry [21-26]. The limited number of interactions permits the generation of a tractable effective Hamiltonian from which spectroscopic studies can be used as an efficient probe of a desired effect. This utility of smaller molecules has resulted in a wealth of information recorded in the literature, including the characterization of spectral constants which has made much of our prior spectral modeling analysis feasible [5-13]. Conversely, comparatively little is known experimentally about the anharmonic spectral constants of radicals. As a result, while emission spectra from vibrationally excited radicals have been readily available [14-20], a near complete lack of information concerning the associated anharmonicity constants largely precludes the possibility of spectral fittings and hence likewise the possibility of energy transfer studies.

Incidentally, the 2003 release of the quantum chemistry suite of programs Gaussian [27-29] now allows one to routinely calculate the anharmonicity constants of reasonably sized polyatomic molecules. As a direct result, it is now conceivable to model the emission spectra from vibrationally excited radical species of interest. Application of the GAUSSIAN assisted model emission spectra to the experimental TR-FTS emission spectra thus provides an opportunity to measure the time-resolved average internal energy, and hence to probe the energy transfer efficiency of radicals. With the addition of this new theoretical tool, it is now possible to couple molecular energy transfer and radical spectral characterization studies. In the chapters which follow, we shall explore the vibrational energy transfer processes in the molecular transients hydrogen isocyanide (HNC) as well as the ketenyl (HCCO) radical.

1.3 A BRIEF TOUR OF FOURIER TRANSFORM SPECTROSCOPY

The various mathematical and engineering details specific to time-resolved Fourier transform spectroscopy have been recorded in painstaking detail many times over [30-34], so much so that it is often half heartedly joked that most accounts are at least partially plagiarized. Given the prominent role that TR-FTS plays in the various studies to be discussed throughout this work however, it would be negligent to not touch upon at least some of the more salient notions. Nevertheless, the interested reader is advised to consult the earlier texts on the subject, particularly the extensive body of work by Griffiths [30,33,34].

At the very core of TR-FTS spectroscopy resides the Michelson interferometer, from which it should become apparent that TR-FTS is an interference based method. In particular, TR-FTS exploits a conjugate Fourier relationship between the interference intensity signal $I(\delta)$ and the desired frequency (i.e. energy) dependent

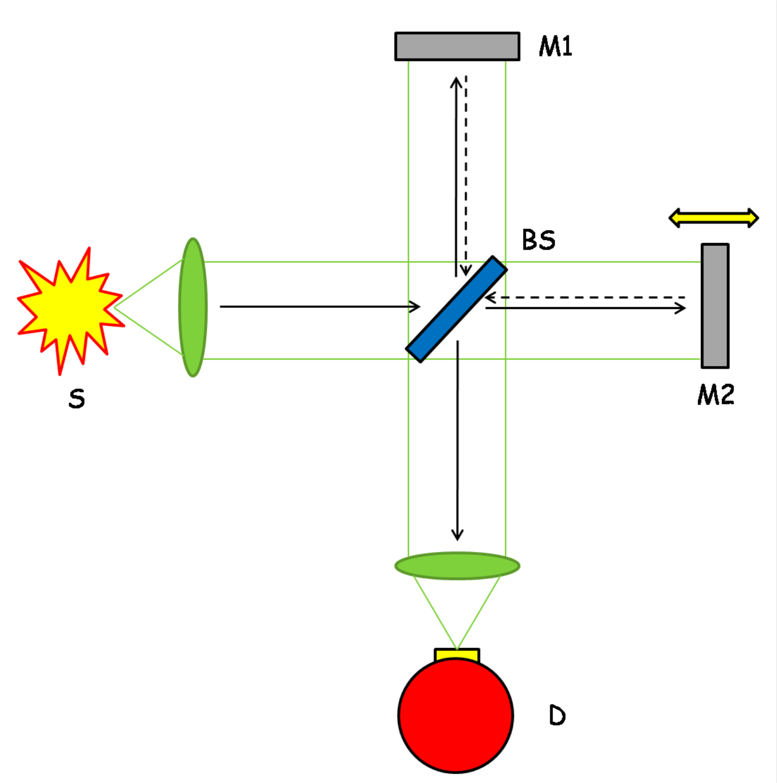

Figure 1.1
Typical representation of a Michelson interferometer composed of a source (S), detector (D), fixed mirror (M1), movable mirror (M2), and a 50% beamsplitter (BS).

signal $I(\nu)$ as [32]:

$$I(\nu) = \int_{-\infty}^{\infty} I(\delta)cos(2\pi\nu\delta)d\delta. \tag{1.1}$$

As depicted in figure 1.1, the general setup of a Michelson interferometer is composed of a source (S), a detector (D), two mirrors [one stationary (M1) and the other movable (M2)], as well as a 50% beamsplitter (BS). The relative displacement of the moveable mirror (M2) is encoded by the optical retardation length δ, which is initially set as zero (producing identical path lengths from the beamsplitter to the two mirrors) and increases over the course of a scan. Radiation to be detected from the source impinges upon the 50% beamsplitter where, as should be expected, half is directed to the stationary mirror (M1) and the remainder passes through to the movable mirror (M2). The radiation is then reflected back off of both mirrors, onto the 50% beamsplitter where a portion of the combined signal is directed back to the source and the remainder goes on to the detector. The generation and intensity of an interference pattern $I(\delta)$ at the detector (and beamsplitter) is governed by the relative displacement of the movable mirror (M2). For the initial equilibrium position of the movable mirror (i.e. with a zero path length difference, δ=0), the reflected signal intensity after the beamsplitter recombines in a fully constructive manner and yields a maximum signal intensity, $I(\delta)_{max}$. However, as the movable mirror shifts away from the zero displacement position ($\delta \rightarrow \infty$), the occurrence of destructive interference becomes more prominent and the signal intensity begins to decrease.

As mentioned briefly above, the experiments to be discussed in this thesis were performed in which the optical retardation length (δ) was systematically varied using the step-scan (or stop-scan) operational mode [32]. The key distinction between step-scan and conventional modes for time-resolved scans resides in the specific operation of the movable mirror. As should be inferred from the name, step-scan mode involves a discrete sampling of the interference signal at each available M2 position. Alternatively, conventional scan (or rapid scan) involves sampling the time-resolved signal while the movable mirror (M2) moves with a constant velocity appropriate for the time-scale of the event occurring at the source. As a result, the use of conventional scan to sample events with increasingly shorter lifetimes would necessarily require increasingly faster velocities for the movable mirror (M2). Step-scan mode, on the other hand, effectively eliminates mirror velocity as an experimental variable, and hence greatly increases the time-scales that can be probed with TR-FTS. Specifically, when employing step-scan mode, the attainable temporal resolution is limited solely by the response time of the electronics of the detection system.

In this laboratory, a pulsed UV laser is used to initiate either a photolysis reaction (typical for radical generation and characterization) or an optical pumping mechanism (for energy transfer studies) within a continuously flowing gas reaction cell. The UV pulse is used both to excite the gas-phase sample as well as an event trigger for the step-scan cycle. Following the arrival of the UV photolysis / excitation pulse, some portion of the molecules within the gas cell become ro-vibrationally excited,

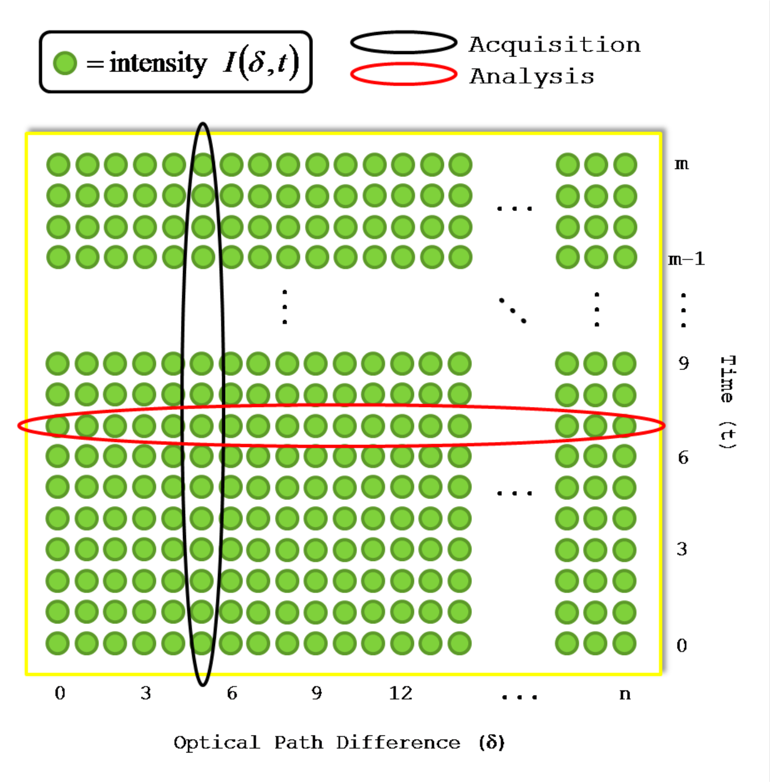

Figure 1.2
Cartoon representation of the interference matrix given as a function of time (t) and mirror displacement (δ). As noted, signal acquisition occurs along fixed mirror displacements as a function of time. Afterwards, analysis of the data (construction of the interferogram) occurs along fixed times as a function of mirror displacement.

and in the presence of the inert collisional species, begin to emit IR radiation as they cascade down their respective ro-vibrational manifolds. For a given mirror position (optical path difference), a discrete set of time-resolved interference intensities are recorded. After the movable mirror has sampled the total temporal range of interest, the next sequential UV pulse causes the mirror to be *stepped* to the next available position. The process repeats, discretely sampling time-resolved interference intensities at each mirror position, until all possible mirror positions have been completely sampled. Figure 1.2 portrays a cartoon representation of the initial set of raw experimental data, organized in an asymmetric ($\delta \times$ t) matrix of interference intensities. A sample slice taken along the mirror displacement (δ) axis, as a function of time, yields an intensity decay function. Alternatively, when analyzed along the temporal

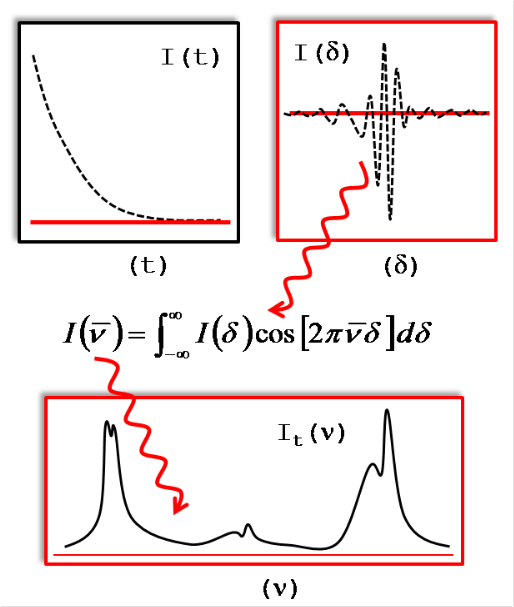

Figure 1.3
General two-dimensional representations of the interference signal, both as a function of time (t) as well as mirror displacement (δ). Following Fourier transformation into frequency space (energy space), a single interferogram yields a single spectrum.

axis (as a function of δ), a series of time-resolved interferograms are obtained.

Figure 1.3 pictorially showcases the full set of data analysis processes; beginning with the collection of a time-resolved decay and culminating in an IR emission spectrum. Once again, when the measured signal intensity is monitored along the temporal axis, a single signal decay $\mathrm{I}_{\delta}(\mathrm{t})$, for a given mirror displacement δ, is observed as a function of time. Alternatively, when that same signal is examined along the optical path difference (δ) instead, a time-resolved interferogram $\mathrm{I}_t(\delta)$ is obtained. Each associated time-resolved interferogram $\mathrm{I}_t(\delta)$ can then be Fourier transformed, using equation 1.1, into frequency-space, yielding the corresponding time-resolved IR emission spectrum, $\mathrm{I}_t(\nu)$. Ultimately, the discrete series of temporally resolved interference intensity decays yield a series of time-resolved interferograms. The complete series of time-resolved interferograms can subsequently be Fourier transformed to yield the corresponding series of time-resolved IR emission spectra.

1.4 A BRIEF LOOK AHEAD

This thesis is devoted to the experimental characterization of vibrational spectral signatures, as well as the examination of the vibrational energy transfer processes, of radical species at high internal energies. Following a methods chapter examining a novel use of two-dimensional correlation analysis as a means of signal-to-noise enhancement, the remaining four chapters will consist of two individual studies, each of which span two separate chapters. The initial focus shall be on the ground state ketenyl (HCCO) radical, generated from the 193 nm photolysis of ethyl ethynyl ether:

$$H_3CH_2C - O - CCH \longrightarrow H_3CH_2C^* + HCCO, \tag{1.2}$$

and the second on hydrogen isocyanide (HNC) following the 193 nm photolysis of vinyl cyanide:

$$H_2C = C(H) - CN \longrightarrow HCCH + HNC. \tag{1.3}$$

As each radical is generated following the photodissociation of a specific molecular precursor, each study will be broken down into a chapter detailing the photodissociation dynamics of the precursor (characterizing the vibrational signature of the radical of interest) as well as a chapter devoted to the spectral fittings of the observed emission spectra and the energy transfer properties of the given radical. The thesis will close with a brief chapter detailing the core conclusions observed throughout.

References:

1. I. Oref and D. C. Tardy, *Chem. Rev.* **90**, 1407 (1990);
   R. E. Weston Jr and G. W. Flynn, *Annu. Rev. Phys. Chem.* **43**, 559 (1992).
2. B. J. Orr and I. W. Smith, *J. Phys. Chem.* **91**, 6106 (1987).
3. B. Nizamov and P. J. Dagdigian, *J. Phys. Chem. A* **105**, 29 (2001);
   M. A. Blitz, M. Pesa, M. J. Pilling, and P. W. Seakins, *Chem. Phys. Lett.* **322**, 280 (2000).
4. G. Herzberg, *The Spectra and Structures of Simple Free Radicals, An Introduction to Molecular Spectroscopy* (Dover Publications, Inc., New York, 1971).
5. G. V. Hartland, D. Qin, and H-. L. Dai, *J. Chem. Phys.* **98**, 6906 (1993).
6. G. V. Hartland, D. Qin, and H-. L. Dai, *J. Chem. Phys.* **100**, 7832 (1994).
7. G. V. Hartland, D. Qin, and H-. L. Dai, *J. Chem. Phys.* **101**, 8554 (1994).
8. G. V. Hartland, D. Qin, and H-. L. Dai, *J. Chem. Phys.* **102**, 6641 (1995).
9. G. V. Hartland, D. Qin, and H-. L. Dai, *J. Chem. Phys.* **102**, 8677 (1995).

10. G. V. Hartland, D. Qin, H-. L. Dai, and C. Chen, *J. Chem. Phys.* **107**, 2890 (1997).

11. C. D. Pibel, E. Sirota, J. Brenner, and H-. L. Dai, *J. Chem. Phys.* **108**, 1297 (1998).

12. D. Qin, G. V. Hartland, and H-. L. Dai, *J. Phys. Chem. A* **104**, 10460 (2000).

13. D. Qin, G. V. Hartland, C. Chen, and H-. L. Dai, *Z. Phys. Chem. A* **214**, 1501 (2000).

14. L. Letendre, D-. K. Liu, C. D. Pibel, J. B. Halpern, and H-. L. Dai., *J. Chem. Phys.* **112**, 9209 (2000).

15. D-. K. Liu, L. T. Letendre and H-. L. Dai., *J. Chem. Phys.* **115**, 1734 (2001).

16. L. Letendre and H-. L. Dai., *J. Phys. Chem. A* **106**, 12035 (2002).

17. W. McNavage, W. Dailey, and H-. L. Dai., *Can. J. Chem.* **82**, 925 (2004).

18. M. J. Wilhelm, W. McNavage, R. Groller, and H-. L. Dai., *J. Chem. Phys.* **128**, 064313 (2008).

19. M. J. Wilhelm, M. Nikow, L. Letendre, and H-. L. Dai., *J. Chem. Phys.* **130**, 044307 (2009).

20. M. Nikow, M. J. Wilhelm, and H-. L. Dai., *J. Phys. Chem. A* **113**, 8857 (2009).

21. G. Herzberg, *Spectra of Diatomic Molecules, Molecular Spectra and Molecular Structure* (D. Van Nostrand Company, Princeton, NJ, 1939).

22. J. L. Steinfeld, R. N. Zare, L. Jones, M. Lesk, and W. Klemperer, *J. Chem. Phys.* **42**, 25 (1965).

23. H. Lefebvre-Brion and R. W. Field, *Perturbations in the Spectra of Diatomic Molecules* (Academic Press Inc.,Orlando, FL, 1986).

24. J. M. Smith, J. C. Bloch, R. W. Field, and J. I. Steinfeld, *J. Opt. Soc. Am. B* **12**, 964 (1995).

25. A. Shayesteh, S. Yu, and P. F. Bernath, *Chem. Eur. J.* **11**, 4709 (2005).

26. W. Xie, C. Harkin, and H-. L. Dai, *J. Chem. Phys.* **93**, 4615 (1990).

27. V. Barone, *J. Chem. Phys.* **120**, 3059 (2004).

28. V. Barone, *J. Chem. Phys.* **122**, 014108 (2005).

29. M. J. Frisch *et al.*, GAUSSIAN 03, Revision C.01, Gaussian, Inc., Wallingford, CT, 2004.

30. P. R. Griffiths and J. A. de Haseth, *Fourier Transform Infrared Spectrometry*, (Wiley-Interscience, Hoboken, New Jersey, 2007).

31. R. Bracewell, *The Fourier Transform and its Application*, (McGraw-Hill, New York, 1965).

32. T. J. Johnson and G. Zachmann, *Introduction to Step-Scan FTIR*, (Bruker Optik GmbH, Ettlingen, Germany, 2000).

33. P. R. Griffiths, *Chemical Infrared Fourier Transform Spectroscopy*, (John Wiley and Sons, New York, 1975).

34. P. R. Griffiths (Ed.), *Transform Techniques in Chemicstry*, (Heyden, London, 1978).

CHAPTER 2

Signal–to–Noise Enhancement in Time–Resolved IR Emission Spectra Through Two–Dimensional Correlation Analysis[†]

[†] The majority of this chapter has been published in the *Journal of Molecular Structure* **883–4**, 242 (2008).

2.1 Introduction

Prior usage of two–dimensional correlation analysis of IR emission from vibrationally excited transient species has lead to the characterization of several vibrational modes of the cyanooxymethyl (OCCN) radical [1] as well as the ketenyl (HCCO) radical [2]. Correlation analysis was used to analyze the similarity between features of different spectra based upon the principle that spectral features associated with the same species, though in different spectra, should share the same time history in their intensity. For example, in the case of the cyanooxymethyl radical, cross–correlation analysis was applied to a series of time–resolved Fourier transform infrared emission spectroscopy (TR–FTIRES) data sets, collected following the 193 nm photodissociation of three different molecular precursors. The spectral features associated with the same species in the three different systems should exhibit a positive correlation as they all have a similar, if not identical, time history represented by similar sets of phase information generated by the Fourier analysis. Subsequently, the spectral features associated with the same transient species can be identified.

In this example, as the core components of the signal present in each series of spectra exhibit a common temporal phase, the diagonal elements of the synchronous correlation map therefore become representative of the IR emission intensity common in all three spectral series. One key notion from this analysis is that the portions of IR emission intensity detected which exhibit non–common temporal phase evolutions, such as random noise with random intensity fluctuations in time or spectral peaks which are not common to all data sets, should be minimally represented in the resulting synchronous diagonal spectrum. This suggests that extraction of the diagonal elements of the synchronous correlation map should yield a spectrum that not only best represents spectral features common to all data sets examined, but should present with an overall enhanced signal to noise (S/N) ratio. In this study, we seek to compare and quantify the resulting S/N in the spectra as obtained through both self– and cross–correlation. Here, self–correlation represents a correlation in which a single series of time–resolved spectra is correlated against itself. Alternatively, by cross–correlation we refer to the correlation between two series of time–resolved spectra, each set from a different experiment.

It is well known that the S/N of a given spectral feature can be enhanced by a statistical factor of $\sqrt{n}$ simply by averaging n different spectra recorded for the same system. The resultant spectra from linear averaging will thus be used as a reference

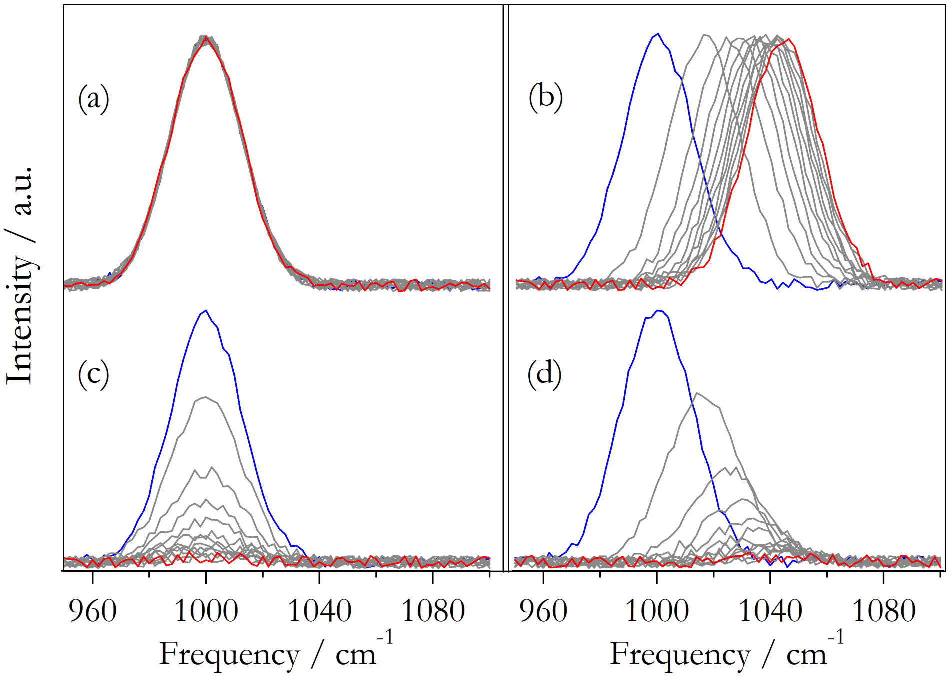

Figure 2.1
Synthetic spectral data sets containing a noise level defined by constant δ_{Noise} = *0.25. The four sets (a) no decay, no shift; (b) no decay, shift; (c) decay, no shift; (d) decay, shift each contains 25 spectra.*

for examining whether or not the synchronous correlation diagonal spectrum indeed produces superior S/N. In what follows, we will quantify the potential overall S/N enhancement obtained both through averaging and synchronous correlation analysis. The comparison will be made through analysis of artificially generated synthetic data sets containing controlled levels of random noise. Experimentally, TRFTIRES spectral features from ro–vibrationally excited molecular species are typically characterized by a maximal initial intensity, followed by decay and blue shift (due to anharmonicity) in frequency towards the fundamental frequency [3–6]. As a check against our experimental data, series of synthetic data sets will be generated so as to mimic the specific behaviors of experimental data including both an intensity decay as well as a shifting frequency band center.

2.2 THEORETICAL SPECTRA AND CORRELATION ANALYSIS

2.2.1 Synthetic spectra

Unique series of synthetic spectral data sets, each containing (n) spectra, were generated through repeated application of the following equation;

$$f_n(\nu) = \sum_{\nu} exp(-\tau\sqrt{n-1}) \times \left\{ \delta_{Noise} + \frac{I}{\sigma\sqrt{2\pi}} exp\left[-\frac{1}{2}\left(\frac{\nu_k + \Delta[n^{1/4} - exp(-\sqrt{n-1})] - \nu}{\sigma}\right)^2 \right] \right\} \tag{2.1}$$

where δ_{Noise} is the noise scale level which is used to add random noise ($0 < x_{Rnd} < 1$) to a gaussian function with band center (ν_k) and FWHM (σ). An intensity decay as well as a band–center frequency shift, which diminishes with time, can be imposed through non–zero values of the decay constant (τ) and shift constant (Δ), respectively.

As featured in Fig. 1, four unique synthetic spectral data sets containing signal exhibiting: (a) no decay and no shift; (b) no decay but with shift; (c) decay but no shift; and (d) both decay and shift, were generated. For each series considered, 25 spectra were created in which the noise scale level was set at ($\delta_{Noise} = 0.25$). For series exhibiting an intensity decay and/or a band center frequency shift, the decay constant was set at ($\tau = 1.0$) and the shift constant was set at ($\Delta = 20$).

Analysis is performed for each scenario using both self– and cross–correlation as well as averaging. By definition, cross–correlation (as well as cross–averaging) necessarily involves the analysis of two different sets of data. In this regard, it is therefore required that, for each signal behavior examined, a minimum of two spectral data sets must be generated. The core signal in both sets will be identical, but the random noise added will be unique, hence permitting the use of cross–correlation (and cross–averaging).

2.2.2 Synchronous correlation diagonal spectrum

The formal mathematical description of two–dimensional cross–spectral correlation has been detailed elsewhere [7]. The cross–spectral correlation analysis formalism was developed based on the general self–correlation analysis [8-15]. Briefly, the numerical representation of the synchronous correlation map is an ($\mathrm{n} \otimes \mathrm{n}$) symmetric matrix, in which n describes the frequency range sampled in the original spectral series. The term *synchronous correlation diagonal spectrum* refers to the synchronous correlation matrix elements for which ($n_1 = n_2$). As the resulting synchronous correlation diagonal spectrum is effectively composed of the product of intensity components from the correlated data sets, a physically meaningful representation is obtained only after taking the square root of the resulting synchronous correlation elements. Fig. 2 highlights the resulting synchronous correlation spectra obtained following cross–correlation analysis of the four unique synthetic data series.

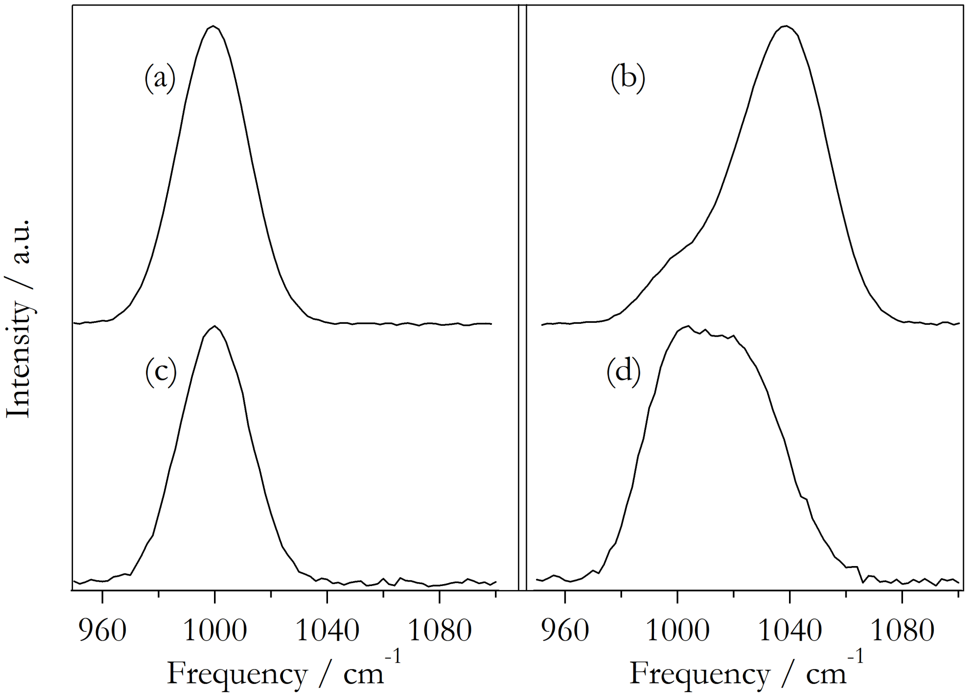

Figure 2.2
Resulting synchronous cross–correlation spectra following analysis of the four spectral series: (a) no decay, no shift; (b) no decay, shift; (c) decay, no shift; (d) decay, shift. Intensity in each spectrum has been normalized so as to permit qualitative comparison of the resulting noise levels.

Qualitatively, all resulting spectra appear to exhibit an enhanced S/N relative to the original data sets (see Fig. 1). Series which exhibit an intensity decay (c and d), however, seem to yield a decreased overall enhancement. In what follows, we examine the resulting S/N of the spectra obtained through both cross– and self–correlation as compared to simply taking the average of the same corresponding data sets.

2.2.3 Signal–to–noise

The S/N ratio of a spectrum is determined in the following manner. For each scenario considered, a series of noiseless spectra ($\delta_{Noise} = 0$) were generated as a basis for comparison. Each set of noiseless spectra was then used to generate a pair of noiseless resultant spectra; one through synchronous self–correlation and the other through linear averaging. The appropriate noiseless spectrum was then subtracted from the corresponding spectrum under examination, either the diagonal of the synchronous map or the linear average, the difference of which was used to define the noise. The absolute value of the noise intensity was then summed up and ratioed against the maximum intensity of the spectral feature yielding the measured S/N.

As an initial step, for each complete series of spectra, the S/N for each individual raw (pre–processed) spectrum was measured. The resulting collection of measured S/Ns was then averaged to yield a singular representative S/N for each complete series of 25 spectra. This averaged S/N is entered in Table 1 as the pre–processed S/N. Next, each unique data set with 25 spectra was processed either through linear averaging or correlation analysis. The S/N for each method of spectral processing was then determined. To avoid statistical fluctuation in the analysis we repeated this S/N determination six times for each different spectral processing method.

Table 2.1

S/N values following spectral processing for each of four synthetic data sets { [ND, NS] no decay, no shift; [ND, S] no decay, shift; [D, NS] decay, no shift; and [D, S] decay, shift }.

Data Set	Analysis	S/N	Φ_{SN}
ND, NS	Pre–processed	75	1.0
	Average (SELF)	377	5.0
	Correlation (SELF)	409	5.5
	Average (CROSS)	544	7.3
	Correlation (CROSS)	510	6.8
ND, S	Pre–processed	75	1.0
	Average (SELF)	333	4.5
	Correlation (SELF)	257	3.4
	Average (CROSS)	473	6.3
	Correlation (CROSS)	307	4.1
D, NS	Pre–processed	13	1.0
	Average (SELF)	66	5.0
	Correlation (SELF)	105	8.0
	Average (CROSS)	93	7.1
	Correlation (CROSS)	127	9.6
D, S	Pre–processed	13	1.0
	Average (SELF)	53	4.0
	Correlation (SELF)	91	6.9
	Average (CROSS)	76	5.8
	Correlation (CROSS)	105	8.0

The relative enhancement (Φ_{SN}) values listed refer to the improvement of S/N in comparison with the pre–processed spectrum. Average–SELF indicates linear averaging of 25 spectra; average–CROSS linear averaging of 50 spectra; correlation–SELF self–correlation analysis among the same set of 25 spectra; and correlation–CROSS cross–correlation among two different sets of 25 spectra each.

For each series analyzed, the six S/N measurements were all within a few percent of each other. Once again, the collected series of S/N measurements were then averaged to yield a representative measure, and recorded in Table 1. Since the cross–correlation process uses two sets of 25 spectra each, linear averaging was conducted with 25 and 50 spectra for comparison against self– and cross–correlation, respectively. The corresponding S/N values are labeled as average (self) and average (cross), respectively, in Table 1.

2.3 THEORETICAL SPECTRAL ANALYSIS

2.3.1 S/N enhancement via correlation vs. averaging

In general for all data sets considered, both correlation analyses as well as simple linear averaging yield superior S/N to that of the corresponding raw spectra in the preprocessed data sets. Fig. 3 shows a comparison of the spectrum obtained from cross–correlation treatment (the diagonal of the synchronous map) vs. the raw spectrum of the (no decay, no shift) series. The S/N after linear averaging of the static signal scenario (no decay, no shift), as expected, shows an enhancement by a factor of 5.0 after averaging 25 spectra and a factor of 7.3 after averaging 50 spectra. Correlation analyses of this series of spectra simply reproduce the S/N enhancement as observed in the linear averaging process. Correlation analysis of data without time–dependence (i.e. containing no phase information) therefore results in the same overall effect as averaging.

Averaging spectral data sets containing a shifting, nondecaying signal results in a diminishment of the S/N enhancement relative to the expected statistical result. The shifting frequency results in a broadened feature with a decreased signal intensity, which yields an overall enhancement of the noise.

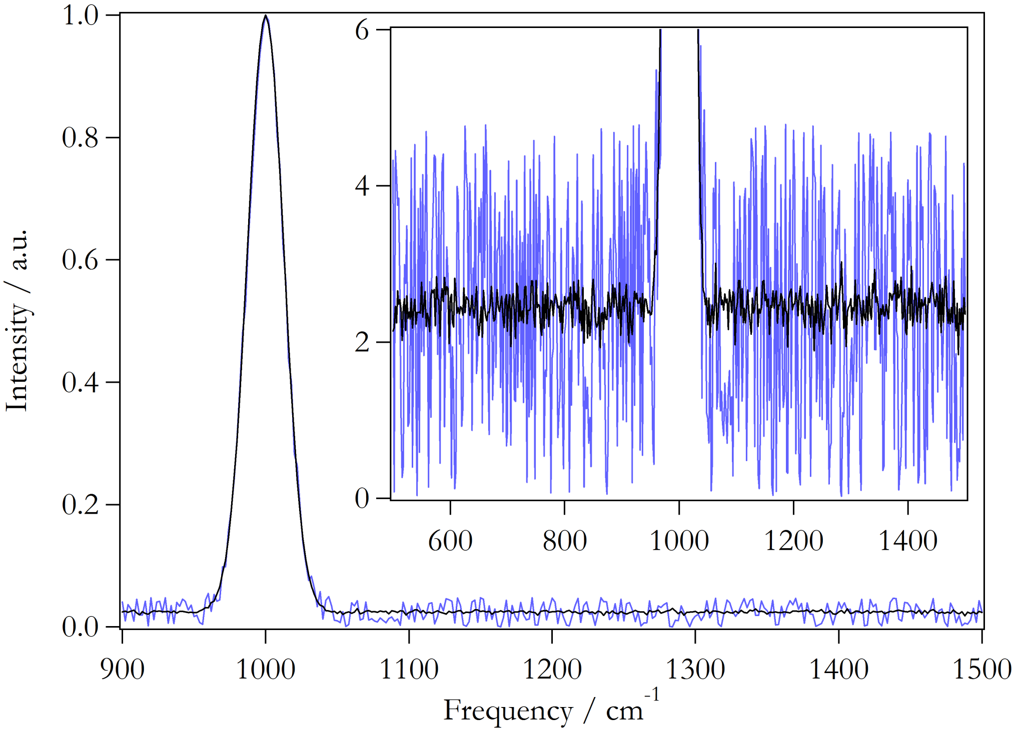

Figure 2.3
Overlay comparison of the synchronous cross–correlation diagonal spectrum (black) for the no decay, no shift series with the original preprocessed data (blue). An expanded view of the noise intensity range (0.0-0.06) has been included as an inset to further highlight the enhancement.

Concurrently, correlation analysis, both self– and cross–, result in an even worse, though still positive, overall S/N enhancement.

Correlation analysis works best for scenarios exhibiting time–dependent intensity decay. The time–dependence of the spectral intensity provides phase differences in the Fourier analysis which allows the correlation analysis to better differentiate the signal from the random noise. For both (decay, no shift) and (decay, shift) data sets, the correlation analyses result in better S/N than linear averaging, though the improvement is not substantial. Specifically, series which include intensity decay are shown to yield quantitatively superior enhancements on the order of $\sqrt{3}$ for self–correlation and $\sqrt{2}$ for cross–correlation as compared to the corresponding linear

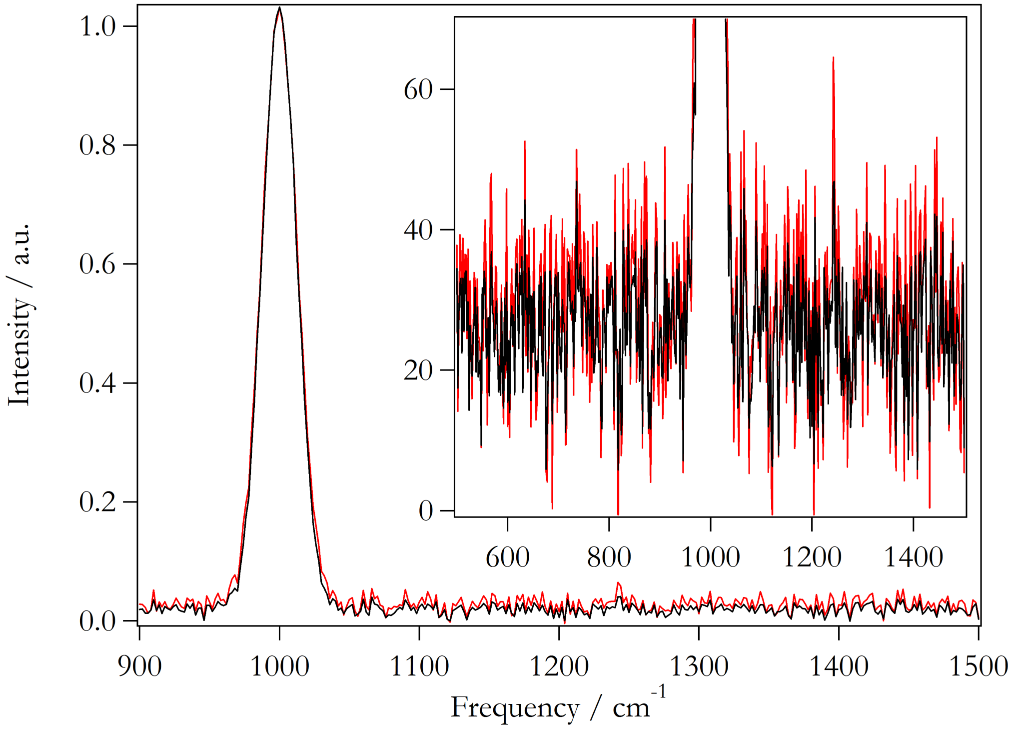

Figure 2.4
Overlay comparison of synchronous cross–correlation diagonal spectrum (black) for the decay, no shift series with the resulting average spectrum (red). An expanded view of the noise intensity range (0.0-0.068) has been included as an inset to further highlight the enhancement.

average results. Fig. 4 highlights this enhancement through a comparison of the resulting spectra obtained for cross–correlation/averaging of the series (decay, no shift). Also as expected, cross–correlation analysis always yields a superior enhancement over self– correlation analysis as the former involves twice the number of raw spectra. It is interesting to note that the observed enhancement for cross–correlation, relative to self–correlation, only scales as $\sqrt[4]{2}$. This observed enhancement can be rationalized by recalling that the physically meaningful representation of the synchronous correlation spectrum requires a square root correction. Therefore, it can be understood that the *raw* synchronous crosscorrelation spectrum will necessarily yield an observed enhancement, over the self–correlation spectrum, which is consistent with the statistically expected result.

Correlation analysis, as described herein, is best suited for dealing with data sets that exhibit an intensity decay without a frequency shift. With a time–dependent variation in intensity, there is a direct overlap of the Fourier components corresponding to the decay of the spectral intensity. Specifically, the intensity decay profile for each frequency component of the spectral feature is aligned in time. If, however, a band center frequency shift is included, there will necessarily be a partial–to–complete misalignment of the decay components which would result in a corresponding partial–to–complete (based upon the magnitude of the shift) mismatch of intensity decay constants in the correlation analysis. A simple way to imagine this would be consideration of the extreme case in which the magnitude of the shift was so great that there is zero overlap between each successive frequency band. For such a case, a very marginal enhancement of the S/N is expected. As the magnitude of the shift considered in our simulation was decreasing with time, there was always at least a partial alignment of the decay components and therefore always at least a partial positive correlation.

2.3.2 Effect of correlation/average on the spectral band shape

The overall qualitative appearance of the spectral feature resulting from correlation or averaging for series not exhibiting a frequency shift appears effectively identical. Conversely, this is not the case for series which exhibit a time–dependent frequency shift. As discussed above, any inclusion of a frequency shift was done so that the magnitude of the shift decreased with time. When such a data set is averaged, the resulting spectrum shows a well defined bias in intensity for the late time band frequency as there is effectively a clustering of signal due to the diminishment of the shift. As observed in Fig. 5, when that very same data set is correlated, either self– or cross–, a larger representation of the early time band appears in the resulting spectrum than in the averaged spectrum. As is particularly evident in the resulting

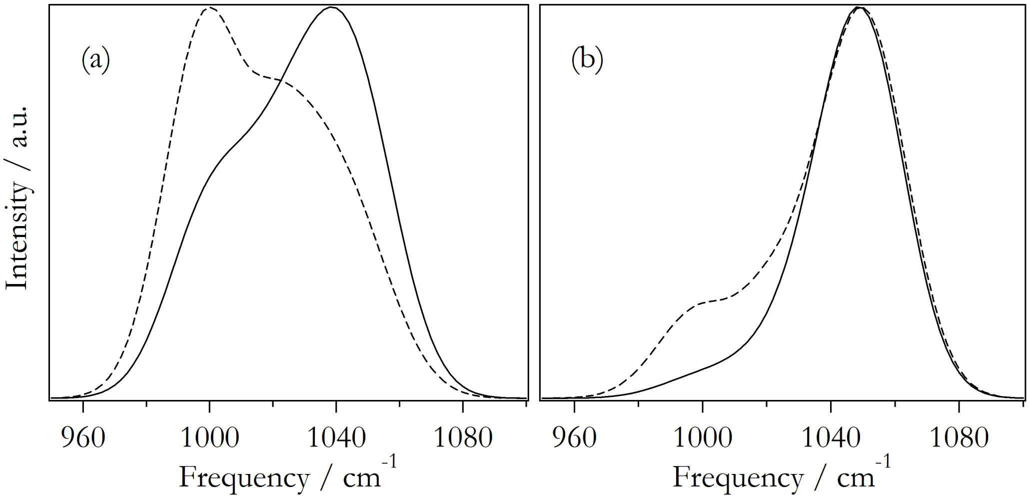

Figure 2.5
Spectra obtained following correlation analysis (dashed) and averaging (solid) of noiseless data sets: (a) decay and shift and (b) no decay and shift.

spectrum for the (decay, shift) series, it is clear that simply averaging the data results in the loss of almost all of the informational content contained in the earliest spectra. As well, for the (no decay, shift) series, the spectrum from correlation analysis conveys more earlier–time information content than the linear average spectrum.

2.4 Experimental spectra and analysis

As a final comparison, two series of TR–FTIRES spectral data sets, collected following the 193 nm photodissociation of ethyl ethynyl ether, were analyzed with both crosscorrelation and averaging. The time–dependent spectra were collected in two separate runs in which the evolving spectral features observed in each experiment are effectively identical, but the non–systematic noise is uniquely different. A more detailed description of the experimental setup has been given elsewhere [16,17]. Briefly, the output from an ArF excimer laser (λ = 193 nm, 20 Hz, 650 mJ/pulse) (Lambda Physik, LPX 200) was collimated through a photolysis cell. The sample typically contained 10-30 mTorr of precursor molecules and 4 Torr of Ar bath gas under constant flow conditions. Emission after the photolysis laser pulse was collected perpendicular to the laser propagation axis by a gold–mirror Welsh cell arrangement in the photolysis cell and then collimated and focused into the FTIR spectrometer by two KBr lenses that match the f/4 focusing characteristics of the spectrometer. The spectrometer (Bruker IFS 66/s) was equipped with an interferometer capable of time–resolved step–scan measurements and a mercury cadmium telluride detector (HgCdTe J15D14, EG&G Judson Technologies, 500 ns rise time, 75010,000 cm^{-1} spectral range). The spectral response of the HgCdTe detector was calibrated with a Globar® source which was modeled as a perfect blackbody.

Interferograms for this work were recorded at 50 ns time intervals averaging

100 laser shots per interferogram point for a total observation window of 20 μs. The time–resolved interferometric signal from the detector was amplified (10 x's) before reaching the transient digitizer (Spectrum PAD82a, 100/200 MHz), which was triggered by a fast photodiode that monitored the excimer output. Subsequent Fourier transform of each interferogram yields a time–resolved spectrum at every 50 ns. The spectral resolution was typically set between 6 and 12 cm^{-1}. Ethyl ethynyl ether is available commercially (Acros Organics, 50% weight stabilized in hexanes). The commercial sample was processed with several freeze pump thaw cycles before use and purity checked with FTIR absorbance spectroscopy.

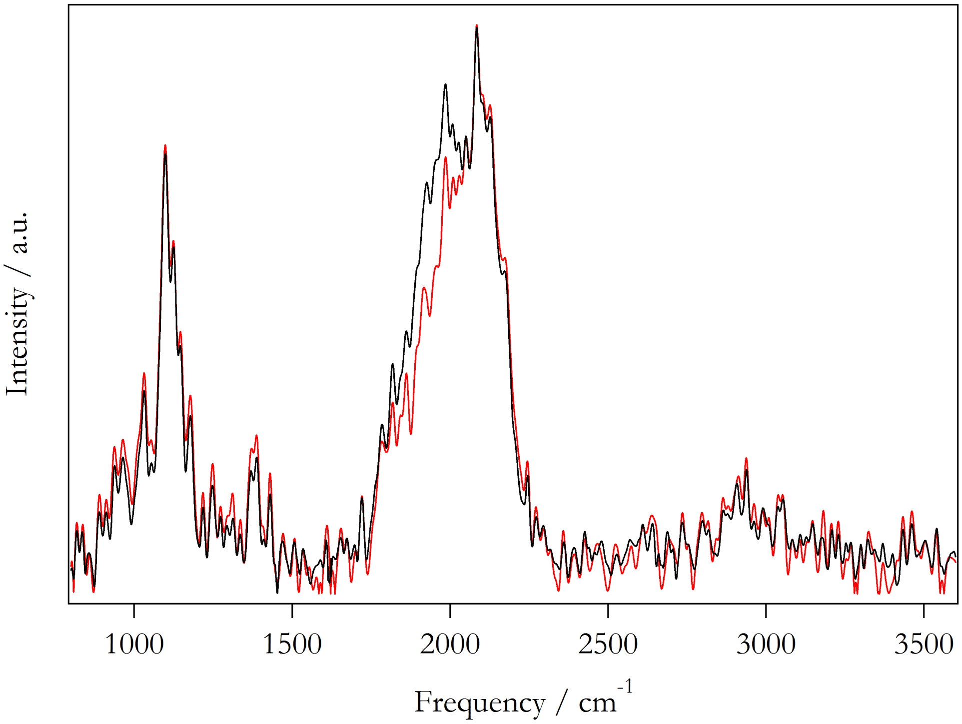

Figure 2.6
Comparison of the resultant spectra following cross–correlation (black) and averaging (red) of two sets of experimental time–resolved IR emission spectra collected following the 193 nm photodissociation of ethyl ethynyl ether.

The most prominent feature in the spectra, an asymmetric band around 2000 cm^{-1}, has been identified as a combination of emission features from the ketenyl (HCCO) radical as well as ro–vibrationally hot CO, generated from the unimolecular dissociation of hot HCCO [2,18,19]. As both HCCO and CO undergo collisional quenching, the intensity of the observed band decreases and the center frequency shifts closer towards the two respective vibrational fundamentals; 2023 cm^{-1} for HCCO [20] and 2143 cm^{-1} for CO. Additionally, a cluster of bands around 1100 cm^{-1}, assignable to the precursor cocktail (ethyl ethynyl ether and hexanes) [2], is observed to grow in over time. The precursor is minimally excited in its ro–vibrational degrees of freedom and hence its emission bands do not undergo an anharmonic blue shift.

Fig. 6 shows a comparison of the resultant spectra from both cross–correlation as well as averaging over the same series of spectra. The S/N of the correlation spectrum is clearly, though minimally, superior to that of the average resultant spectrum. This result is consistent with our expectations based upon the analyses of the synthetic data sets. Furthermore, as the HCCO + CO bands do exhibit frequency shift, it is understandable that the resultant features in the correlation spectrum appear more spread out than the corresponding features in the average spectrum. Concurrently, as the 1100 cm^{-1} band does not shift in frequency, this feature appears effectively identical in both spectra. The overall S/N enhancement, compounded with a more representative core spectral signal, suggests that correlation analysis yields a better representation of the original series of spectra.

2.5 CONCLUSION

Extraction of the diagonal elements of the synchronous correlation map, for both self– and cross–correlation, has been shown to yield a representative spectrum with superior S/N as compared to the original raw data set. Moreover it has been shown that the correlation spectrum yields superior S/N, as compared with the spectrum obtained from simple linear averaging, for spectral series exhibiting a time–dependent variation in signal intensity. This is likely due to the fact that the time–dependence provides additional phase information in the Fourier analysis which can be used to differentiate the core signal from the random noise which has no discernible phase information. The enhancement in S/N through correlation, as well as through linear averaging, diminishes when the spectral feature exhibits a time–dependent frequency shift. In addition to general effects on S/N, it was observed that the resulting correlation spectra yield a better overall representative spectral signal, as compared with linear averaging, for spectral data sets exhibiting a time–dependent frequency shift. Whereas simply averaging the raw data sets results in a loss of information contained in the earliest spectra, correlation analysis tends to preserve more of the core signature of the entire original series.

Acknowledgement

This work was supported in part by Basic Energy Sciences, U.S. Department of Energy, through Grant No. DEFG 02–86ER 134584.

References

1. W. McNavage, W. Dailey, H-. L. Dai, *Can. J. Chem.* **82**, 925 (2004).
2. M. J. Wilhelm, W. McNavage, R. Groller, H-. L. Dai, *J. Chem. Phys.* **128**, 064313 (2008).

3. G. V. Hartland, D. Qin, H-. L. Dai, *J. Chem. Phys.* **102**, 8677 (1995).
4. G. V. Hartland, D. Qin, H-. L. Dai, *J. Chem. Phys.* **107**, 2890 (1997).
5. D. Qin, G. V. Hartland, H-. L. Dai, *J. Phys. Chem. A* **104**, 10460 (2000).
6. D. K. Liu, L. Letendre, H-. L. Dai, *J. Chem. Phys.* **115**, 1734 (2001).
7. W. McNavage, H-. L. Dai, *J. Chem. Phys.* **123**, 184104 (2005).
8. I. Noda, A. E. Dowrey, C. Marcott, *Appl. Spectrosc.* **47**, 1317 (1993).
9. Y. Ozaki, Y. Liu, I. Noda, *Appl. Spectrosc.* **51**, 526 (1997).
10. H. Wang, R. A. Palmer, in: Y. Ozaki, I. Noda (Eds.), *Two-Dimensional Correlation Spectroscopy*, vol. 1, American Institute of Physics, Kobe-Sanda, Japan, 1999 (Chapter 4).
11. A. Matsushita, Y. Ren, K. Matsukawa, H. Inoue, Y. Minami, I. Noda, Y. Ozaki, *Vib. Spectrosc.* **24**, 171 (2000).
12. Y. M. Jung, B. Czarnecki-Matusewicz, Y. Ozaki, *J. Phys. Chem. B* **104**, 7812 (2000).
13. C. I. Morita, Y. Ozaki, I. Noda, *Appl. Spectrosc.* **55**, 1618 (2001).
14. S. Sasic, A. Muszynski, Y. Ozaki, *Appl. Spectrosc.* **55**, 343 (2001).
15. Z. W. Yu, L. Chen, S. Q. Sun, I. Noda, *J. Phys. Chem. A* **106**, 6683 (2002).
16. G. V. Hartland, W. Xie, H-. L. Dai, Rev. *Sci. Instrum.* **63**, 3 (1992).
17. L. Letendre, H-. L. Dai, I. A. McLaren, T. J. Johnson, *Rev. Sci. Instrum.* **70**, 18 (1999).
18. D. L. Osborn, *J. Phys. Chem. A* **107**, 3728 (2003).
19. M. J. Krisch, J. L. Miller, L. J. Butler, H. Su, R. Bersohn, J. Shu, *J. Chem. Phys.* **119**, 176 (2003).

20. K. G. Unfried, G. P. Glass, R. F. Curl, *Chem. Phys. Lett.* **177**, 33 (1991).

CHAPTER 3

Photodissociation of Ethyl Ethynyl Ether at 193 nm: The ν_1 CH Stretching Mode of the Ketenyl (HCCO) Radical[†]

[†] The majority of this chapter has been published in the *Journal of Chemical Physics* **128**, 064313 (2008).

3.1 INTRODUCTION

The ketenyl radical (HCCO) has received much attention recently for its importance in hydrocarbon combustion chemistry. Combustion of several commonly used hydrocarbons involves the HCCO radical. For example, HCCO is a critical intermediate in the oxidation of all C_2 hydrocarbons [1]. One such reaction in which HCCO is a key product is between acetylene and O(^3P) [1-6], a dominating reaction in the combustion of all fuels [1]. In the presence of molecular oxygen, the ketenyl radical is able to further react through one of two pathways [4]. The channel that results in the production of CO_2, predicted to account for 90% of the reactions of HCCO with O_2, has been proposed [4] as a new pathway for prompt CO_2 formation.

Of the many studies carried out on HCCO, only a handful have been on the spectroscopy of this radical. The first submillimeter wave study of the HCCO radical by Endo and Hirota nearly two decades ago found the radical to be a near prolate symmetric top with a large A–rotational constant and an asymmetry parameter near unity κ_{asym}=-0.9998 [7]. This study also revealed a spin–rotation splitting that exhibits a large K_a dependence, indicating interaction of the ground state with another low–lying electronic state. Of the five distinct types of Renner–Teller interactions [8], the case C interaction in which one potential curve is attractive, while the other is repulsive with respect to a bending coordinate, is best suited for describing HCCO. Its lowest energy Renner–Teller pair consists of the ground state with bent equilibrium geometry and a low–lying excited state with a linear geometry.

The vibrational mode that presumably has the strongest intensity, the ν_2 asymmetric–CCO stretch, has been experimentally determined through infrared flash kinetic spectroscopy [6] with its term value set at 2022.644 cm^{-1}. Furthermore, the ν_5 cis–CCH bend, the most Franck–Condon active mode, has been identified at 494

cm^{-1} in the photofragment yield spectrum of HCCO [9]. The other remaining vibrational modes are yet to be experimentally observed.

In terms of theoretical calculations, several studies [4,10-14], including the ones performed in our own laboratory using GAUSSIAN03 that are reported here, have been carried out on the HCCO electronic ground state. HCCO in the electronic ground state is shown to be a bent molecule with Cs symmetry. The $\tilde{A}(^2\Pi)$ state is predicted to be 3.4 kcal/mol above the minimum of the electronic ground state [12], while the $\tilde{a}(^4A")$ state is predicted to lie at 54.2 kcal/mol above the ground state [14].

Vibrational spectroscopy of radicals has been generally challenging due to the transient nature of radical species and because they are typically produced in small quantities. Time–resolved Fourier transform infrared emission spectroscopy (TR–FTIRES) has proven to be a versatile technique that can detect IR vibrational modes of a transient species with modest spectral resolution [15-20]. In this approach, the target radical is first produced with internal excitation from photodissociation of a selected precursor molecule. TR–FTIRES is then used to detect IR emission with temporal resolution from all the dissociation products that are vibrationally excited. Information on the time evolution of the intensity and frequency of the emission features, with the aid of comparison to theoretical calculations, can then be used to assign vibrational modes of the emitting species.

To successfully implement this experimental approach, an efficient way to produce ketenyl with sufficient internal excitation is needed. Previously, UV dissociation ($\lambda = 193nm$) of ketene has been used to produce HCCO [1,2,5,9,21-23]. However, among the various dissociation channels of ketene, the one resulting in the production of ketenyl has a quantum yield of only 0.107 [22]. Another method to produce HCCO has been through the reaction of $O(^3P)$ with acetylene [7]. As this process is relatively slow at room temperature, a key challenge has been getting enough reaction to occur within a short duration to produce an appreciable amount of ketenyl for detection. Furthermore, there is a competing channel producing methylene whose reactions and radiation make spectroscopic interpretation more complex. Hydrogen abstraction reactions from ketene by F, Cl, and OH have also been investigated, but these reaction channels were found to be unfavorable with negligible yields [7,24].

Recently, Krisch et al.[2], following the suggestion of Bersohn [25], demonstrated a new and efficient means to produce the HCCO radical through 193 nm dissociation of ethyl ethynyl ether (EEE). Their photofragment translational energy spectroscopy study found that the EEE precursor is a clean source of HCCO with a near–unit photodissociation quantum yield. Based on the bimodal translational energy distributions for the HCCO fragment, it was suggested that the ketenyl radical is produced in two different electronic states: 63% in the $\tilde{a}(^4A")$ state and 37% in the lower $\tilde{X}(^2A")/\tilde{A}(^2\Pi)$ states. The two lower electronic states lie very close to each other in energy and, thus, are listed together here. Up to 97 kcal/mol of energy may be available for internal excitation of the products after 193 nm photolysis of EEE. Additionally, Fockenberg performed a time–of–flight mass spectrometry study that sets the ketenyl quantum yield at $91 \pm 14\%$ [26]. Furthermore, in addition to the ketenyl and ethyl radical channel, two minor channels leading to the production of ethylene and ketene as well as acetylene and formaldehyde were observed. The dissociation channels of EEE based on the two studies can be summarized as

$$HCCO - CH_2CH_3 + h\nu(193nm) \rightarrow HCCO(\tilde{a}^4A'') + CH_2CH_3; \quad \Phi \sim 57\% \quad (3.1a)$$

$$\rightarrow HCCO(\tilde{X}^2A'') + CH_2CH_3; \quad \Phi \sim 33\% \quad (3.1b)$$

$$\rightarrow HCC(\tilde{A}^2\Pi) + OCH_2CH_3; \quad \Phi \sim 0\% \quad (3.1c)$$

$$\rightarrow HCCH + CH_3CHO; \qquad \Phi \sim 8\% \quad (3.1d)$$

$$\rightarrow CH_2CH_2 + CH_2CO; \qquad \Phi \sim 2\% \quad (3.1e)$$

In the following, we show results from the use of EEE as the precursor to photolytically produce HCCO and the detection of IR emission by time–resolved Fourier transform IR spectroscopy. Based on these observations/analyses, we present here the first experimental evidence of the detection of the ν_1 stretch mode of the HCCO radical.

3.2 EXPERIMENTAL

A more detailed description of the experimental setup has been given elsewhere [17,27]. Briefly, the output from an ArF excimer laser ($\lambda = 193nm$, 20 Hz, ≤50 mJ/ pulse) (Lambda Physik, LPX 200) was collimated through a photolysis cell mounted with two CaF_2 windows. The sample typically contained 10-30 mTorr of precursor molecules and 4 Torr of Ar bath gas under constant flow conditions. Pressure was monitored with a capacitance manometer (MKS Baratron, 0-10 Torr). Emission after the photolysis laser pulse was collected perpendicular to the laser propagation axis by a gold–mirror Welsh cell arrangement in the photolysis cell and then collimated and focused into the FTIR spectrometer by two KBr lenses that match the f/4 focusing characteristics of the spectrometer. The spectrometer (Bruker IFS 66/s) was equipped with an interferometer capable of time–resolved step–scan measurements, a mercury cadmium telluride (MCT) detector (J15D14, EG&G Judson Technologies, 500 ns rise time, 750-10,000 cm^{-1} spectral range), as well as an indium antimony (InSb) detector (J10D, EG&G Judson Technologies, 50 ns rise time, 1850-10,000 cm^{-1} spectral range). The internal cavity of the FTIR was continually flushed with a FTIR purge gas generator (75–45, Parker Balston). The spectral responses of the MCT and InSb detectors were calibrated with a Globar® source which was modeled as a perfect blackbody.

Interferograms for this work were recorded at 50-100 ns time intervals averaging 50-100 laser shots per interferogram point for a total observation window of 20 μs. The time–resolved interferometric signal from the detector was amplified (ten times) by a fast amplifier (Stanford Research Systems SR445, DC–300 MHz) before reaching the transient digitizer (Spectrum PAD82a, 100/200 MHz), which was triggered by a fast photodiode that monitored the excimer output. The InSb experiments included a transimpedance preamplifier (PA–9, EG&G Judson Technologies, 616 kHz) prior to the fast amplifier. The interferometer signal was monitored by a stand–alone oscilloscope (Tektronix TDS3052B) that was interfaced with the spectrometer. Subsequent Fourier transform of each interferogram yields a time–resolved spectrum at every 50-100 ns. Overall, the MCT system possessed a faster response time in which the 500 ns rise time of the detector was the limiting factor. To enhance the observed signal to noise resolution, the emission spectra (collected at 50-100 ns intervals) were averaged in bins over a total window of 500 ns. Alternatively, spectra from the InSb system, which were temporally limited by the transimpedance preamplifier with a response time of around 1600 ns, were averaged in bins over a total window of 1.7 μs. The spectral resolution was typically set between 6 and 12 cm^{-1}.

Ethyl ethynyl ether is available commercially (Acros Organics, 50% weight stabilized in hexanes). The commercial sample was processed with several freeze pump thaw cycles before use and the purity was checked with FTIR absorbance spectroscopy. EEE has an absorption cross section $\sigma_{193nm} = 7 \times 10^{-18}$ cm^2 / molecule, while the hexane stabilizer has a negligible absorption cross section $\sigma_{193nm} = 3 \times 10^{-22}\ cm^2$ / molecule [4]. Argon gas from the supplier (Spectra Gas, research grade, 99.9%) was used directly. Unphotolyzed sample was recollected after each experiment and frozen at liquid nitrogen temperature. This sample was then reclaimed and purified for further use.

3.3 Results

3.3.1 Time–resolved IR emission spectra

Figure 1 highlights representative IR emission spectra following the 193 nm photodissociation of EEE, as collected with the MCT detection setup. The time–resolved spectra contain emission features not only from IR active modes of vibrationally excited HCCO but also from other vibrationally excited species that may result from EEE fragmentation and subsequent reactions. Due to the effects of anharmonicity,many emission features in the earliest time slices, when the emitting species contain more internal energy, shift from the red side toward the fundamental transition frequency. This blueshift is more apparent in earlier time slices. As collisions occur, the IR emission collected at later times eventually arises from the fundamental transitions as the vibrationally excited molecules deactivate down the vibrational manifold to the ν=0 levels.

The most prominent feature in the IR emission spectra is a fast rising broad peak which spans from 1600-2300 cm^{-1}. Prior studies of the vibrational structure of HCCO suggest that a portion of this band likely contains contributions from the rovibrationally excited asymmetric CCO stretch of HCCO at 2023 cm^{-1} [6]. Additionally, the thermodynamics of the UV dissociation of EEE, as detailed by the

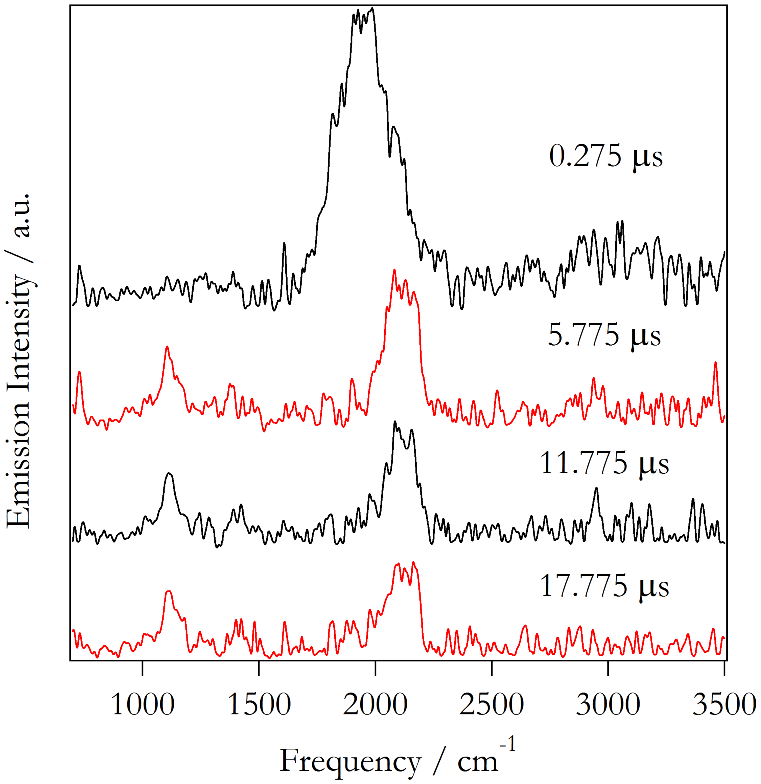

Figure 3.1
Representative time–resolved emission spectra following 193 nm dissociation of ethyl ethynyl ether as observed with a MCT detector. The intensity has been corrected with the detector spectral efficiency.

photofragment translational spectroscopy (PTS) study [2], suggests that HCCO is generated with sufficient internal energy to dissociate into CO and CH, with up to ν=3 vibrational population in the CO fragment. In light of this possibility, it is expected that the broad feature is likely a combination of rovibrationally excited HCCO and CO.

The next most notable feature is the slow rising band centered near 1110 cm^{-1}. Comparison with the static absorption spectra of a mixture containing both the precursor EEE and hexanes (as stabilizer) suggests a likely assignment of this feature, as well as other weaker features throughout the spectra, as vibrationally excited EEE. As evidenced through the late onset of this feature, the vibrational excitation of these molecules is resulted from either reaction of ketenyl with ethyl ethynyl ether or collision between these molecules with an excited photolysis product. Additionally, there is a broad progression of features spanning the CH stretching region. The presence of the low energy features from the precursor EEE (as well as its hexane stabilizer) suggests that there should be corresponding weak CH stretching activity, specifically in the 2880-2974 cm^{-1} region. However, due to low signal to noise

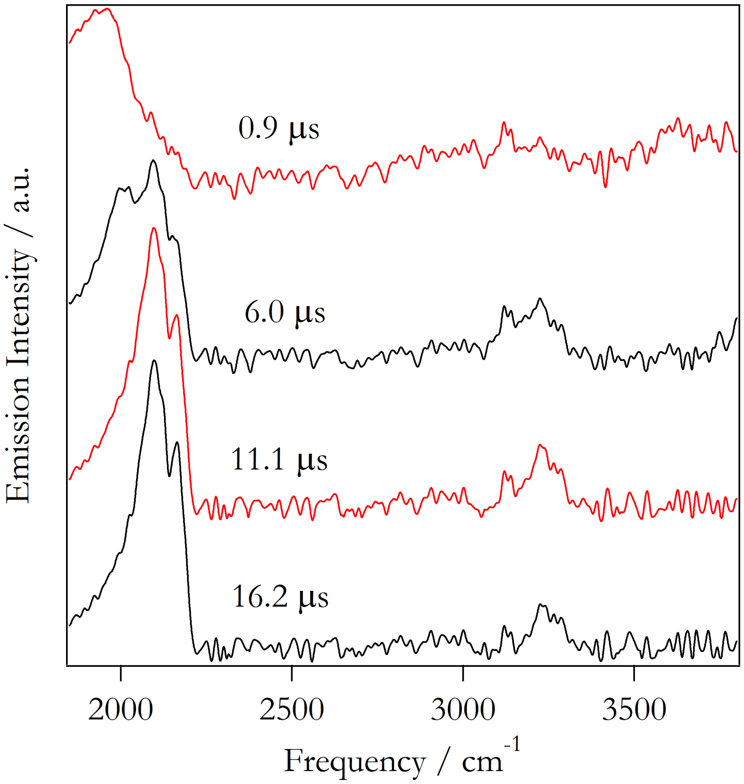

Figure 3.2
Representative time–resolved FTIR emission spectra following 193 nm photodissociation of ethyl ethynyl ether as observed with an InSb detector. The intensity has been corrected with the detector spectral efficiency.

(S/N) in this region, definitive assignments of these features, as well as any CH stretching feature from HCCO, are not made with these spectra.

Figure 2 highlights representative time–resolved spectra following the dissociation of EEE as collected with the InSb detection setup. As with the MCT experiments, the HCCO +CO bands spanning from 1600-2300 cm^{-1} are still the

Table 3.1
Summary of observed spectral features and assignment of origin in the TR–FTIRES spectra detected following 193 nm photolysis of EEE.

Frequency(cm^{-1})	Species	Dissociation channel
1024–1180	EEE + Hexanes	Precursor
1387	EEE + Hexanes	Precursor
2167	EEE + Hexanes	Precursor
2880–2978	EEE + Hexanes	Precursor
2143	CO	(1a) and (1b)
1379	CH_2CH_3	(1a) and (1b)
3000	CH_2CH_3	(1a) and (1b)
3037	CH_2CH_3	(1a) and (1b)
3131	CH_2CH_3	(1a) and (1b)
3289	HCCH	(1d)
3299	HCC	(1c)
3600–3800	HCC	(1c)
2023	HCCO	(1b)
3232	HCCO	(1b)

most prominent, though observation of the low energy tail has been lost due to the 1850 cm^{-1} cutoff of the InSb detector. New to the InSb spectra are two band systems which were unresolvable in the MCT spectra. There is an early rising broad (and weak) feature peaking at around 3600 cm^{-1} and continuing up to just below 3800 cm^{-1}, and another band spanning 3100-3300 cm^{-1}. The 3600 cm^{-1} band is assignable to the $\tilde{X}(00^0 0) \longleftarrow \tilde{A}(000)^1$ transition of the ethynyl (HCC) radical [28]. The region right below 3800 cm^{-1} is likely composed of unresolved vibronic transitions from higher vibrational levels of the $\tilde{A}^2\Pi$ state of HCC [28]. Of more interest is the band spanning 3100-3300 cm^{-1}. Immediately apparent is the CH_2 asymmetric stretch of the ethyl radical at 3130 cm^{-1} [29]. Additionally, there is a partially resolved peak at around 3230 cm^{-1} as well as a cluster of peaks which extend just above 3300 cm^{-1}. The mass spectrometry studies have shown that both HCCH [26] as well as HCC [2] are minor photoproducts in this dissociation, both of which possess transitions near 3300 cm^{-1}. As vibrationally excited ketenyl is the expected major product of this dissociation, coupled with the fact that the features of the ethyl radical appear well below 3200 cm^{-1}, the 3230 cm^{-1} peak is tentatively assigned as the ν_1 CH stretch of the ketenyl radical. Table I summarizes the observed features and assignments of origin in both MCT and InSb spectra.

3.3.2 Temporal dependence of the observed emission intensity

The emission features in the spectra may arise from the primary photolysis products as well as their secondary reactions that may generate vibrationally excited byproducts. Under the pressure conditions of the gas cell, secondary reactions do occur on the time scale of experimental observation. Emission from the primary photofragments or the secondary reaction products should have a different time dependence. The primary photofragment emission should have an immediate rise in intensity within the detector response time. The secondary reaction product emission will have a slower rise regulated by the collisional frequency and the reaction rate.

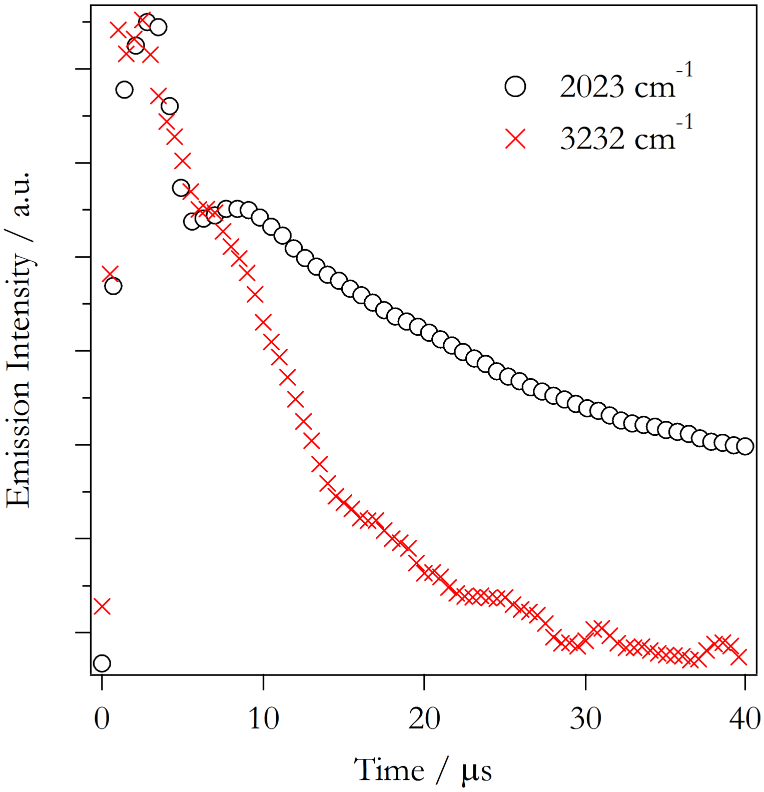

Figure 3.3
Integrated time profile of the 2023 cm^{-1} *(HCCO* ν_2*, ○) and the 3232 cm*$^{-1}$ *(*ν_1*, ×) features. Both features show a fast rise (on the time scale of the detection system) time followed by a moderately fast decay process. The 2023 cm*$^{-1}$ *feature also shows a slower secondary rise followed by a very slow decay from vibrationally excited CO.*

In order to differentiate the origin of the emission feature with respect to primary versus secondary reactions, we first define the time behavior of a given spectral feature. Since the spectral features often display shifts in frequency, we will use the intensity confined within a narrow spectral bandwidth that we assign with a particular feature for determining the temporal evolution. Intensity within this spectral bandwidth is integrated for each time slice and plotted as a function of time.

Figure 3 is a comparison of the time dependences of the two features likely originating from HCCO. The trace of circles ($\bigcirc$) is representative of the temporal dependence of the intensity of the 16002300 cm^{-1} feature with a focus on a 30 cm^{-1} window at around 2023 cm^{-1}. As expected from the results of the PTS study, the 16002300 cm^{-1} feature is clearly composed of two temporally distinct intensity evolutions. There exists a fast rise/decay feature, attributable to the ν_2 mode of HCCO, as well as a slower rise/decay feature originating from vibrationally excited CO. The trace of crosses ($\times$) is the integrated intensity time profile of the 3230 cm^{-1} feature which exhibits a singular temporal evolution. Of particular interest is the comparison of the time dependence of the 3230 cm^{-1} peak with that of the fast rise/ decay component of the 2023 cm^{-1} peak.

Both of these integrated time profiles have rise times on the order of a primary photolysis reaction limited by the detection system with a 1600 ns rise time. As mentioned above, a previous study [6] has identified the ν_2 mode of HCCO at 2023 cm^{-1}. Therefore, if the 3232 cm^{-1} feature is from HCCO, it is expected that it would share a common intensity temporal evolution with that of the ν_2 mode at 2023 cm^{-1}.

3.4 Two–Dimensional Correlation Analysis

It has been shown that two–dimensional (2D) correlation analysis can be used to reveal features that share similar time dependence in intensity in congested time–resolved FTIR emission spectra [30]. In the first application to TR–FTIRES spectra, 2D analysis was applied to decipher the correlation between spectra obtained using different precursors. The phase information of individual spectral features is embedded in the time dependence of the intensity and frequency of the spectral feature. The cross–spectral correlation analysis on the spectra acquired following the UV dissociation of three different precursor systems has lead to the identification of common featuresthe previously uncharacterized vibrational modes of the cyanooxymethyl (OCCN) radical [30].

In 2D correlation analysis, the synchronous correlation map is used to identify those spectral features which are common to both data sets. Specifically, the diagonal elements of the synchronous map, averaged over all sampled correlation sets, yield representative spectra of features common to all systems. As the noise in each of the spectra carries random phase information, only signals common to all systems appear in the spectrum extracted as the synchronous correlation diagonal elements. The second component of correlation analysis, the asynchronous map, aids in the determination of whether or not the given features originate from common sources. Of particular importance is the relative magnitude of off–diagonal features, both in the synchronous and the asynchronous correlation maps. Specifically, features from common sources should exhibit positive off–diagonal correlation in the synchronous map and zero off–diagonal correlation in the asynchronous map [30]. Deviation from this pattern is highly suggestive of accidental overlap, or simply features originating from unrelated emission sources.

In this study, 2D correlation was applied to the InSb data sets with the intent of enhancing the S/N ratio in the CH stretching region, specifically that of the 3200-3300 cm^{-1} band. Although all spectral data were acquired using a single precursor, cross correlation of the spectral sets obtained through different experiments allows suppression of noise and enhancement of the observed signal.

Cross–spectral 2D analysis was conducted through two different approaches: correlation analysis of spectra over selected temporal windows as well as that of spectra spanning the complete temporal profile. The first approach has the advantage of improving the S/N in intensity while retaining the information on frequency shift as a function of time for the spectral features. In this approach, each of four experimental data sets, spanning the 20 μs following the photolysis pulse, was partitioned

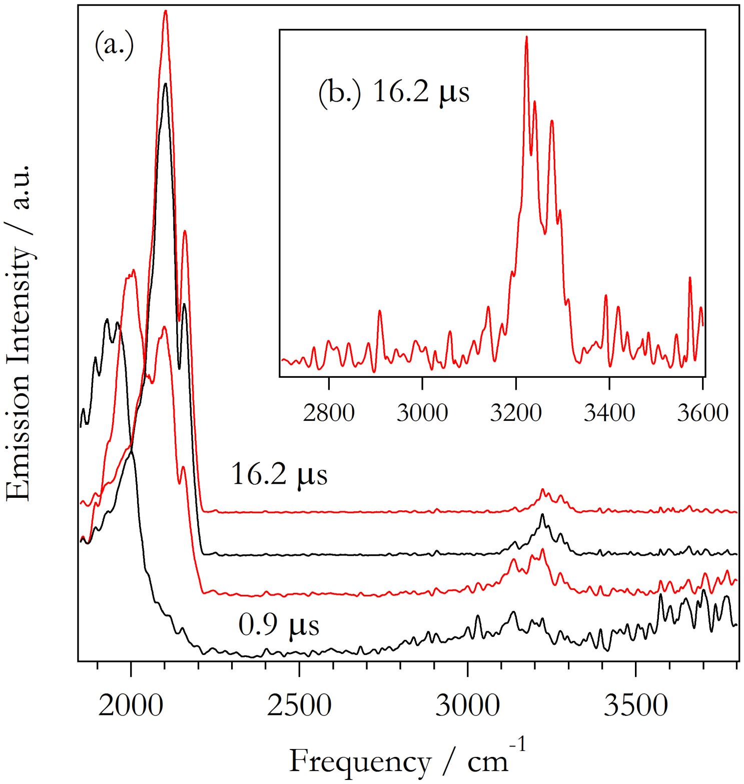

Figure 3.4
(a) Spectra at different times following photodissociation extracted as diagonals from the synchronous correlation maps. (b) Late time (16.2 μs) spectra of the CH stretching region magnified (30×'s) to show detail.

into ten 1.7 μs wide bins (in accordance with the temporal response time of the InSb detection setup). Each temporal bin was synchronously correlated with the associated temporal bin of the remaining three data sets. The diagonal elements of the synchronous correlation map, representing spectral features common to both data sets being correlated, were extracted and averaged over all four experiments to generate a new representative spectrum for each temporal bin. Figure 4(a) shows the averaged diagonal spectra extracted from the temporal bins at (0.9, 6.0, 11.1, and 16.2) μs following the dissociation. The spectra clearly reveal the appearances of the ethyl radical at 3000 cm^{-1} (CH_3 asymmetric stretch), 3030 cm^{-1} (CH_2 symmetric stretch), and 3130 cm^{-1} (CH_2 asymmetric stretch). Additionally, an asymmetric band centered at 3289 cm^{-1} and extending above 3300 cm^{-1} suggests the presence of minor populations of acetylene and ethynyl (C_2H) whose CH stretching fundamentals appear at 3289 and 3298 cm^{-1}, respectively [28,31]. Figure 4(b) highlights the CH stretching region of the extracted diagonal spectra from the 16.2 μs bin. Of particular interest is the enhanced clarity of the ν_1 CH stretch of HCCO, centered at 3232 cm^{-1}, which exhibits a blueshift of about 50100 cm^{-1} over the noted time span.

2D correlation analysis was also performed on data sets containing spectra from the InSb experiments which span the full 20 μs window of observation. Analysis of the asynchronous correlation map (Fig. 5) shows a broad off–diagonal asynchronous correlation corresponding to the HCCO + CO peak (1850-2200 cm^{-1}) with that of the CH stretching region spanning from 2800 to 3800 cm^{-1}. Upon closer examination, it is apparent that the asynchronous correlation associated with the 3200-3300 cm^{-1} band diminishes just below 2030 cm^{-1}, implying that this band is not asynchronously correlated with the ν_2 CCO stretch of ketenyl. The absence of an asynchronous correlation between these two bands indicates that these two features share a common temporal evolution and, hence, are likely originating from a common source. We note

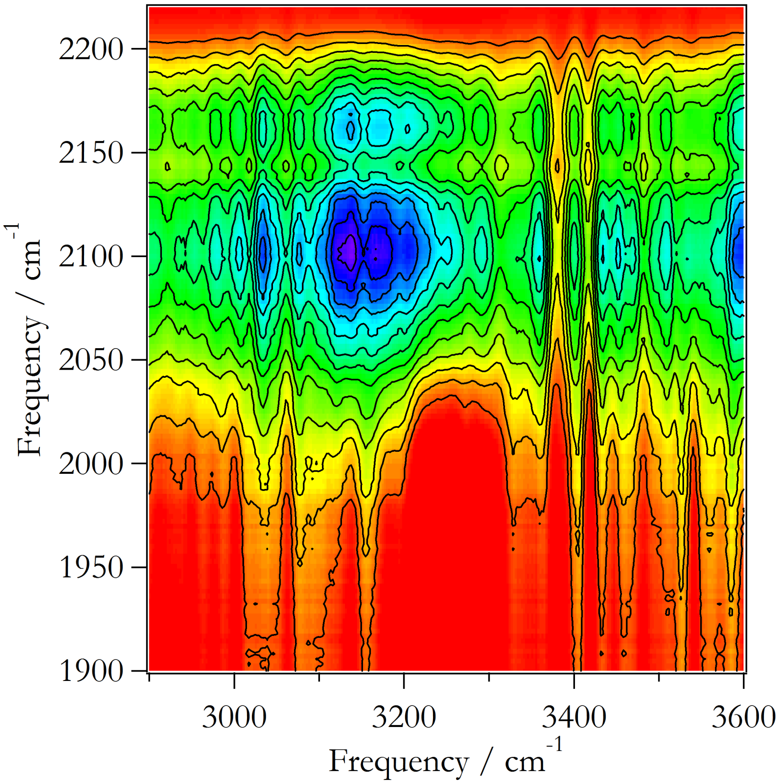

Figure 3.5

2D asynchronous correlation map of the InSb spectra highlighting the off–diagonal correlation between the HCCO+CO peak and the CH stretching region.

that the other features above 2800 cm^{-1} are all asynchronously correlated to the entire HCCO+CO peak.

3.5 DISCUSSION

3.5.1 Ab Initio *Calculations*

Theoretical calculations of the frequency, intensity, and even the anharmonicity of the unknown vibrational modes provide useful comparison with and guidance for spectral assignment. Two sets of theoretical calculations on HCCO($\tilde{X}^2A\prime\prime$) are presented here: one conducted in our laboratory using GAUSSIAN03 performed at the UB3LYP/EPR–III level of theory [10] and the other done by Szalay at the CCSD(T)/cc–pVTZ level [11]. New additions to the 2003 release of the quantum chemistry program

Table 3.2
Theoretical frequencies (cm^{-1}), with anharmonic corrections, transition dipole moments (D), and relative emission intensities (arbitrary units) of the vibrational modes of the HCCO ($\tilde{X}^2A''$) radical.

Mode	Description	$\nu_{1\leftarrow 0}$ (cm^{-1})	$\lvert\mu_{1\leftarrow 0}\rvert$(D)	Int (a.u.)	Method
1	CH Str.	3208	0.076	52.54	dft
		3233	0.068	43.65	cc
2	asy–CCO Str.	2053	0.256	100.00	dft
		2058	0.254	100.00	cc
3	sym–CCO Str.	1261	0.047	0.48	dft
		1248	0.040	0.34	cc
4	CCO bend	576	0.070	0.05	dft
		577	0.121	0.14	cc
5	CCH bend	385	0.492	0.46	dft
		473	0.433	0.81	cc
6	Torsion	539	0.047	0.02	dft
		530	0.039	0.01	cc

Density functional (dft) calculations were calculated at the UB3LYP / EPR–III level of theory in the GAUSSIAN03 *suite (Ref. 32). Coupled cluster (cc) calculations were performed by Peter Szalay (Ref. 11) at the CCSD(T) / cc–pVTZ level of theory.*

GAUSSIAN03 include the option to treat anharmonic portions of the potential energy with second–order perturbation theory (PT2) [32-34]. With PT2, it is possible to calculate the vibrational anharmonic constants χ_{ij} through theoretically evaluated higher order energy derivatives [34,35]. The vibrational term values can then be computed from the calculated harmonic frequencies and second–order anharmonic constants.

The fundamental transition frequencies, calculated from the anharmonically corrected term values, as well as the transition dipole moments and scaled emission intensities of the normal modes of ground state ketenyl are shown in Table II. In both calculations, it is evident that the ν_2 asymmetric CCO stretch is the strongest mode as observed through emission. Of the modes that are in the range of our detection systems, the ν_1 CH–stretch mode is predicted to be the next strongest at about one order of magnitude weaker than that of the ν_2 mode. We note the relatively good agreement with regards to both frequency and calculated intensities between the two calculations. The experimentally determined ν_2 frequency of 2023 cm^{-1} is in close agreement with frequencies calculated with anharmonic corrections, requiring a correction factor of only (0.98).

A comparison between the *ab initio* calculated emission spectrum and the experimentally measured emission spectrum is made in Fig. 6. The emission spectrum observed at 17.9 μs after the photolysis pulse (at which time, following Ca. 1000 collisions with Ar, the HCCO emission features are expected to be primarily fundamental transitions) is overlaid with the calculated emission transitions (expanded as Gaussian widths) from the coupled–cluster calculation. As noted in Table II, the calculated absorption intensities have been transformed into the associated expected emission intensities via the frequency cubed correction factor where the appropriate transition dipole moments, in units of debye, have been obtained from the calculated absorption intensities. It is important to keep in mind in comparing the calculated

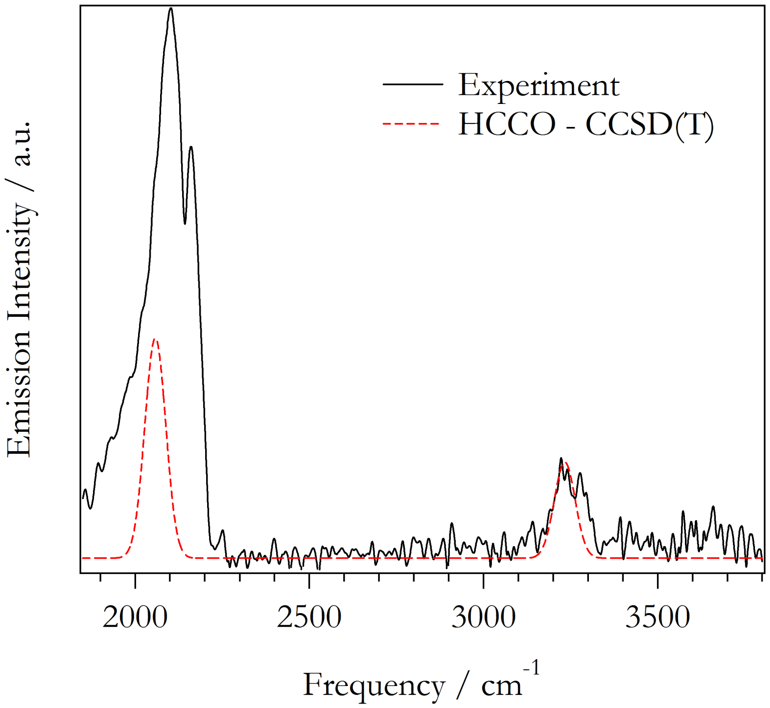

Figure 3.6
Comparison of the late time (17.9 μs) spectrum extracted as the square root of the synchronous correlation diagonal and a calculated IR emission spectrum based on the anharmonically corrected coupled–cluster calculation of Szalay (Ref. 11).

intensities with the observed spectra that the emission from vibrationally excited CO contributes to the observed emission intensity in the region of the ketenyl ν_2 stretch. Additionally, compared to the ν_1 mode of ketenyl, the ν_2 mode is a less energetic motion and as a result (within the assumption of a Boltzmann distribution for the excited molecules) should possess greater population and, hence, more intensity as compared with that of the ν_1 stretch. In light of these considerations, the apparent extra intensity of the ν_2 stretch in the observed spectra, as compared with the calculation, can be understood and both the frequency and intensity simulated from the calculations are, therefore, consistent with assigning the 3232 cm^{-1} peak in the experimental spectra to the ν_1 mode of HCCO. We note that the coupled–cluster calculation with associated anharmonic correction has coincidentally generated a numerical value identical to the value experimentally determined from the line shape fitting of the time–integrated spectra.

3.5.2 Emission Spectral Simulation

The enhanced resolution obtained through the synchronous correlation diagonal elements permits extraction of HCCO ν_1 CH stretch spectra with details sufficient for rotational contour analysis. Microwave spectroscopy has determined the rotational constants of the ground electronic state of HCCO [7]. Using the spectral constants from the GAUSSIAN03 calculation (harmonic frequencies, transition dipole moment, anharmonic constants, etc.) as well as the energy level expression and selection rules for a rigid–rotor/ harmonic oscillator, a simulated rotational contour can be generated. In this simulation, rovibrational transition intensities were modeled with a rotational temperature of 300 K as well as with the Hönl–London factors of a symmetric top molecule [36]. Furthermore, GAUSSIAN03 was used to determine the projection of the transition dipole moments of the normal vibrational modes of HCCO onto the molecular frame. It was determined that both the ν_1 and ν_2 modes should exhibit predominantly a–type transitions (K_a=0) with calculated b/a ratios of 0.401 and 0.129, respectively. Figure 7 shows a comparison of the late time (17.9 μs) experimental emission spectrum versus the simulated spectrum of the ν_1 CH stretching mode of HCCO. The vibrational term value in the simulation was left as an adjustable parameter in the simulation.

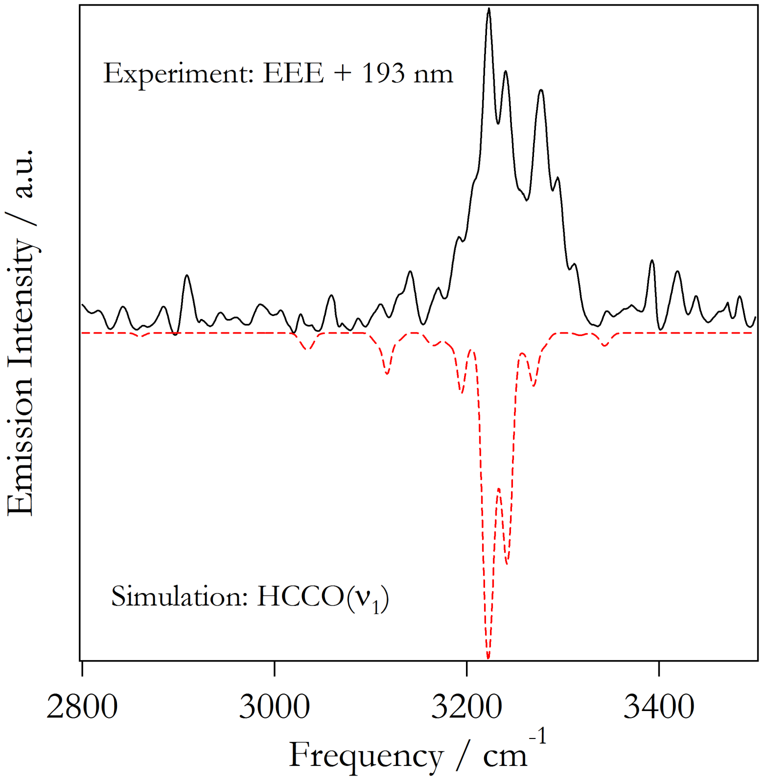

Figure 3.7
Comparison of the late time (17.9 μs) emission spectrum (solid line) and the rotational contour simulation (inverted dashed line) of the ν_1 *CH stretching mode of ketenyl.*

It was found that the simulated rotational contour matched well with that of the observed emission spectrum. Through comparison of the positions of the minimum intensity of the P and R branches of the simulated spectrum with those of the experimental spectrum, the term value was determined to be at 3232.3 cm^{-1} for the ν_1 CH Stretching mode of ketenyl.

3.5.3 Alternative IR Emitters For Features $> 3200\ cm^{-1}$

In addition to the primary photofragments HCCO and CH_2CH_3, mass spectrometry studies have shown that mass channels corresponding to C_2H [2] as well as C_2H_2, C_2H_4O, C_2H_4, and C_2H_2O [26 are also generated in minor quantities during the 193 nm photodissociation of EEE. The question now remains as to whether or not any of these species could be responsible for the observed peak at 3232 cm^{-1}. As the mass spectroscopy studies provide information regarding the mass and not the specific structure, it is important to consider transitions from all possible geometric combinations of the available mass fragments.

Both vibronic and rovibrational transitions of the ethynyl (C_2H) radical have been observed in the early time InSb spectra. Vibronic transitions appear as a broad series of features spanning above at 3600 cm^{-1} to just below 3800 cm^{-1}. The ν_1 CH stretch of ethynyl is well characterized and has been assigned with a band center at 3298 cm^{-1}, [28] which may account for the high energy portion of the broad feature spanning just above 3300 cm^{-1}. The time scale of the observation precludes the possibility of vinylidene [37] (H_2CC) from appearing in the InSb spectra. The ν_3 CH stretch of acetylene, however, would account for the remaining portion of the same high energy feature spanning just above 3300 cm^{-1}. The remaining species, with the exception of those containing OH, all possess fundamental vibrational transitions well below 3200 cm^{-1}. The ν_1 OH stretching modes of CH_2CHOH [38] and HCCOH [39] have been previously observed at 3633.5 and 3501.3 cm^{-1}, respectively, though there is no clear evidence of their presence in the collected spectra. The ν_2 CH stretch of HCCOH [39] appears at 3340 cm^{-1} and, hence, is also not an origin of the 3232 cm^{-1} peak.

3.6 Conclusion

The ν_1 CH stretch of the ketenyl radical has been identified in the time–resolved IR emission spectra, collected following the 193 nm photodissociation of EEE. Temporal evolution of the intensity of the observed feature has been found to be consistent with the time dependence of that of the previously characterized ν_2 asymmetric CCO stretch. This relation is also confirmed from a 2D correlation analysis of the time–resolved spectra. The observed frequency and intensity are also consistent with values obtained from *ab initio* calculations for the ν_1 CH stretch mode.

Time–resolved spectra with overall enhanced S/N were obtained through extraction of the diagonal elements of the synchronous correlation maps. In comparison with simulated rotational contour analysis, the vibrational term value of the fundamental transition was determined to be 3232 cm^{-1}.

Acknowledgement

This work is supported by Basic Energy Sciences, U.S. Department of Energy, through Grant No. DEFG 02–86ER 134584. William McNavage's participation in this study was funded through a NASA Earth System Science Fellowship (No. R–ESSF/03–0000–0110).

References

1. L. R. Brock, B. Mischler, and E. A. Rohlfing, J. Chem. Phys. 110, 6773 (1999).
2. M. J. Krisch, J. L. Miller, and L. J. Butler, J. Chem. Phys. 119, 176 (2003).
3. K. W. Sattelmeyer, Y. Yamaguchi, and H. F. Schaefer, III, Chem. Phys. Lett. 383, 266 (2004).

4. D. L. Osborn, J. Phys. Chem. A 107, 3728 (2003).
5. D. L. Osborn, D. H. Mordaunt, H. Choi, R. T. Bise, D. M. Neumark, and C. M. Rohlfing, J. Chem. Phys. 106, 10087 (1997).
6. K. G. Unfried, G. P. Glass, and R. F. Curl, Chem. Phys. Lett. 177, 33 (1991).
7. Y. Endo and E. Hirota, J. Chem. Phys. 86, 4319 (1987).
8. T. J. Lee, D. J. Fox, H. F. Schaefer, III, and R. M. Pitzer, J. Chem. Phys. 81, 365 (1984).
9. L. R. Brock, B. Mischler, E. A. Rohlfing, R. T. Bise, and D. M. Neumark, J. Chem. Phys. 107, 665 (1997).
10. W. McNavage, Ph.D. thesis, University of Pennsylvania, (2004).
11. P. G. Szalay,(private communication).
12. P. G. Szalay, J. Chem. Phys. 106, 436 (1997).
13. P. G. Szalay, G. Fogarasi, and L. Nemes, Chem. Phys. Lett. 263, 91 (1996).
14. C. Hu, H. F. Schaefer III, Z. Hou, and K. D. Bayes, J. Am. Chem. Soc. 115, 6904 (1993).
15. G. V. Hartland, D. Qin, and H. L. Dai, J. Chem. Phys. 107, 2890 (1997).
16. G. V. Hartland, W. Xie, D. Qin, and H. L. Dai, J. Chem. Phys. 97, 7010 (1992).
17. L. Letendre, H. L. Dai, I. A. McLaren, and T. J. Johnson, Rev. Sci. Instrum. 70, 18 (1999).
18. D. K. Liu, L. Letendre, and H. L. Dai, J. Chem. Phys. 115, 1734 (2001).
19. W. McNavage and H. L. Dai, Can. J. Chem. 82, 925 (2004).
20. I. Noda, A. E. Dowrey, and C. Marcott, Appl. Spectrosc. 47, 1317 (1993).

21. E. J. Feltham, R. H. Qadiri, E. E. H. Cottrill, P. A. Cook, J. P. Cole, G. G. Balint–Kurti, and M. N. R. Ashfold, J. Chem. Phys. 119, 6017 (2003).

22. G. P. Glass, S. S. Kumaran, and J. V. Michael, J. Phys. Chem. A 104, 8360 (2000).

23. D. H. Mordaunt, D. L. Osborn, H. Choi, R. T. Bise, and D. M. Neumark, J. Chem. Phys. 105, 6078 (1996).

24. J. Gruβdorf, J. Nolte, F. Temps, and H. G. Wagner, Ber. Bunsenges. Phys. Chem. 98, 546 (1994).

25. R. Bersohn, J. Chin. Chem. Soc. (Taipei) 49, 291 (2002).

26. C. Fockenberg, J. Phys. Chem. A 109, 7150 (2005).

27. G. V. Hartland, W. Xie, and H. L. Dai, Rev. Sci. Instrum. 63, 3 (1992).

28. R. Tarroni and S. Carter, J. Chem. Phys. 119, 12878 (2003).

29. The Ethyl Radical, 2004 (http://webbook.nist.gov).

30. W. McNavage and H. L. Dai, J. Chem. Phys. 123, 184104 (2005).

31. Acetylene, 2007 (http://webbook.nist.gov).

32. M. J. Frisch, G. W. Trucks, H. B. Schlegel et al., GAUSSIAN03, revision B.0.5. Gaussian, Inc., Pittsburgh, PA, 2003.

33. V. Barone, J. Chem. Phys. 120, 3059 (2004).

34. V. Barone, J. Chem. Phys. 122, 014108 (2005).

35. I. M. Mills, Molecular Spectroscopy: Modern Research, edited by K. N. Rao and C. W. Mathews (Academic, New York, 1972).

36. R. Zare, Angular Momentum: Understanding Spatial Aspects in Chemistry and Physics (Wiley–Interscience, New York, 1988).

37. K. M. Ervin, J. Ho, and W. C. Lineberger, J. Chem. Phys. 91, 5974 (1989).

38. CH_2CHOH, 2007 (http://webbook.nist.gov).

39. HCCOH, 2007 (http://webbook.nist.gov).

CHAPTER 4

Collisional Deactivation of Vibrationally Highly Excited Ketenyl Radicals Through Long–Range Attractive Interactions

4.1 INTRODUCTION

In the most general sense, combustion is the chemical process by which organic molecules (RH) are converted into carbon dioxide (CO_2) and water (H_2O) through reaction with molecular oxygen (O_2):

$$RH + O_2 + M \longrightarrow CO_2 + H_2O + M, \tag{4.1}$$

where M represents an excess backing pressure of an (inert) collider species (typically molecular nitrogen N_2). Clearly this is not a concerted process, but is rather the combined resultant of a number of chemical reactions. Of the numerous intermediate species formed, it has been well established that acetylene (HCCH) is an important gateway species in the combustion of both aliphatic and aromatic hydrocarbons [1,2]. What's more, as the main loss channel of acetylene (through reaction with $O(^3P)$ atoms) yields the ketenyl (HCCO) radical and atomic hydrogen (H) [2], the overall importance of HCCH is directly transferable to HCCO:

$$HCCH + O(^3P) \longrightarrow H + HCCO. \tag{4.2}$$

Furthermore, once HCCO is generated, it can then react with (O_2) to yield one of the final combustion products (CO_2):

$$HCCO + O_2 \longrightarrow H + CO + CO_2, \tag{4.3}$$

where CO and H then go on to react further to yield (H_2O) as well as more (CO_2).

Based upon reaction (3) alone, it is easily argued that ketenyl is a pivotal combustion intermediate. Nevertheless, it has been theorized by the Schaefer group

[3] that HCCO may play an even greater role in combustion, specifically through the electronic quenching of quartet methylidyne (CH) radical. As depicted in figure 4.1, it has been calculated [3] that the methylidyne radical (a common combustion intermediate) preferentially reacts with ground state CO (a byproduct of reaction (3)) to yield quartet state HCCO.

$$CH(a^4\Sigma^-) + CO(X^1\Sigma^+) \longrightarrow HCCO(a^4A''), \tag{4.4}$$

The zero-point energy of the quartet state of HCCO has been calculated to fall about 1 eV below that of the ground state bond dissociation energy (3.14 eV) [2,3]. In this regard, depending upon the nascent internal energy content of the quartet state HCCO formed in reaction (4), collision-induced intersystem crossing (CI-ISC) could yield vibrationally highly excited ground-state HCCO. What happens next is contingent upon the efficiency with which ground state HCCO transfers energy out of its internal degrees of freedom. If vibrational energy transfer is inefficient (as is typically the case for non-resonant transitions), the resulting HCCO will predominantly undergo unimolecular dissociation to yield ground state CH + CO. Alternatively, if energy transfer is efficient, vibrational quenching will be competitive with dissociation and the excited HCCO will cascade down the ro-vibrational manifold and survive to eventually react with (O_2) as in reaction (3).

In both cases, unimolecular dissociation and collisional quenching, HCCO is observed to play an extended role in the chemistry of combustion. In the former, additional transient HCCO is generated which quickly dissociates to yield ground state CH + CO. In the latter, a secondary (*meta-stable*) HCCO source is generated and eventually reacts to yield H, CO, and CO_2. In this regard, a complete understanding of the kinetics of combustion thus requires determining whether or not these two processes are competitive with one another. It is therefore highly desirable to characterize the efficiency of vibrational energy transfer in ground state HCCO.

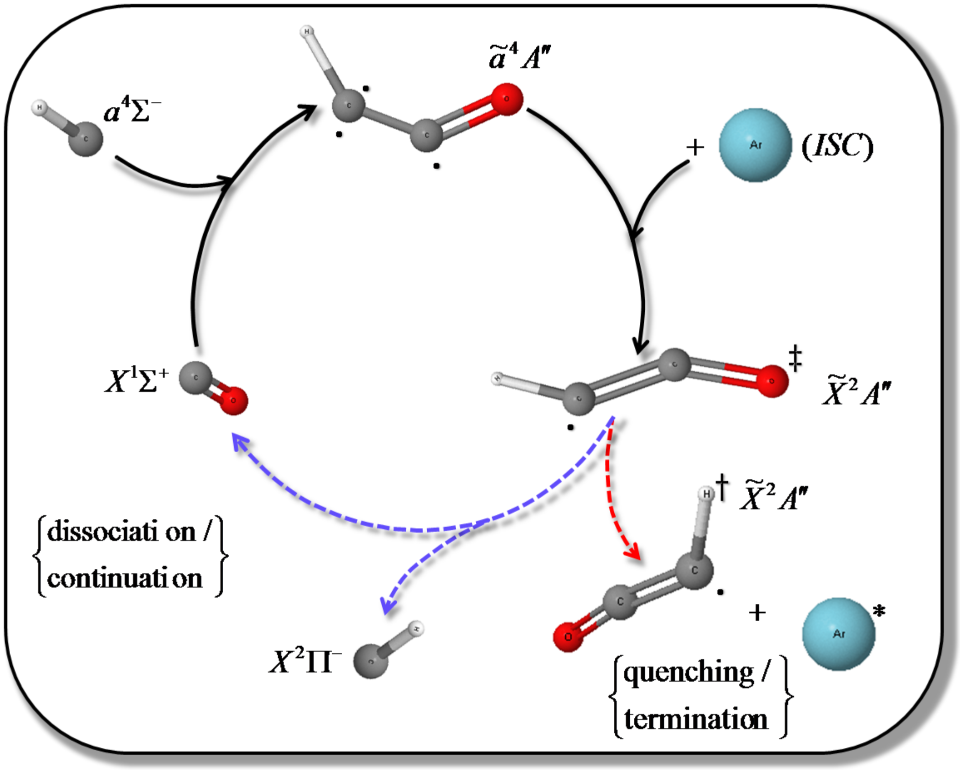

Figure 4.1 *Electronic quenching of the methylidyne (CH) radical via the quartet state of ketenyl (HCCO). Following collision induced intersystem crossing, vibrationally highly excited ground state ketenyl can then either dissociate (yielding ground state methylidyne radical and carbon monoxide); or (if vibrational energy transfer is efficient enough) it can be collisionally quenched.*

In chapter three of this thesis, we examined the 193 nm photolysis of ethyl ethynyl ether (EEE) as a clean photolytic source of ketenyl radicals. The dissociation reaction was monitored with microsecond time-resolved Fourier transform infrared emission spectroscopy (TR-FTIRES). As evidenced through a large anharmonic shift in the observed ν_1 CH stretch mode, it was concluded that the above reaction generated highly vibrationally excited ground state ketenyl radicals. Given that the photolysis produces HCCO with near unit quantum efficiency, the shifting CH signal is largely overlap free and hence serves as a convenient probe of the internal energy content of the radical. Furthermore, by selectively varying the identity of the associated collisional quencher, it is possible to examine the vibrational energy transfer processes of HCCO.

In what follows, we present a detailed study of the vibrational energy transfer processes of the ketenyl radical. While HCCO is a physically stable molecule (i.e. it possesses a non-zero bond dissociation energy), like most radical species it is chemically unstable (i.e. it is reactive). Thus, in an effort to limit the occurrence of secondary reactions, we exclusively employ inert rare-gas atomic species as collisional partners and hence only examine energy transfer through vibrational-to-translational (V-T) pathways. Ro-vibrational spectral modeling, using *ab initio* quantum chemical assisted anharmonic analysis, permits a quantitative measure of the temporal evolution of the internal energy content of the HCCO radicals. Additionally, variation of the rare-gas collider species provides measurable trends which can be analyzed within the context of an impulsive collisional deactivation model, quantified using a modified variant of Schwartz, Slawsky, and Herzfeld's (SSH) theory of vibrational relaxation [4]. We also explore the associated effect of long range attractive interactions on the vibrational energy transfer efficiency of the ketenyl radical.

4.2 EXPERIMENTAL

The experimental method employed in the current study has been described previously [5-7], as such only a brief summary will be given here. The output from an

ArF excimer laser ($\lambda = 193$ nm, 20 Hz, ≤ 50 mJ/pulse) (Lambda Physik, LPX 200) was collimated through a photolysis cell mounted with two CaF_2 windows. The sample typically contained 10-30 mTorr of sample (ethyl ethynyl ether) and 2-4 Torr of an inert atomic collider gas (helium, neon, or argon) under constant flow conditions. Pressure in the cell was monitored with a capacitance manometer (MKS Baratron, 0-10 Torr). Emission after the photolysis laser pulse was collected perpendicular to the laser propagation axis by a gold-mirror Welsh cell arrangement in the photolysis cell and the collimated and focused into the FTIR spectrometer with two KBr lenses that match the f/4 focusing characteristics of the spectrometer. The spectrometer (Bruker IFS 66/s) was equipped with an interferometer capable of time-resolved step-scan measurements and an indium antimony (InSb) detector (J10D, EG&G Judson Technologies, 50 ns rise time, 1850-10,000 cm^{-1} spectral range). The internal cavity of the FTIR was continually flushed with a FTIR purge gas generator (75-45, Parker Balston).

The spectral response of the InSb detector was calibrated with a *Globar*® source which was modeled as a perfect blackbody. Interferograms for this work were recorded at 500 ns time intervals averaging 50-100 laser shots per interferogram point for a total observation window of 50 μ s. The time-resolved interferometric signal from the detector was initially passed through a transimpedance preamplifier (PA-9, EG&G Judson Technologies, 616 kHz) and then amplified (ten times) by a fast amplifier (Stanford Research Systems SR445, DC-300 MHz) before reaching the transient digitizer (Spectrum PAD82a, 100/200 MHz), which was triggered by a fast photodiode that monitored the excimer output. The interferometric signal was monitored on a stand-alone oscilloscope (Tektronix TDS3052B) that was interfaced with the spectrometer. Subsequent Fourier transform of each interferogram yields a time-resolved spectrum at every 500 ns. To further enhance the observed spectral resolution, spectra were synchronously cross correlated [8] to yield representative spectra spanning 1.0 μ s intervals. The spectral resolution was typically set as 12 cm^{-1}.

Ethyl ethynyl ether (EEE) is available commercially (Acros Organics, 50% weight stabilized in hexanes). The commercial sample was processed with several freeze pump thaw cycles before use and the purity was checked with FTIR absorbance spectroscopy. At 193 nm, EEE has a strong absorption cross section $\sigma_{193nm} \sim 7{*}10^{-18}$ cm^2/molecule, while the hexane stabilizer has a negligible absorption cross section of $< 3 * 10^{-22}$ cm^2/molecule [9]. Helium, Neon, and Argon gases from the supplier (Spectra Gas, research grade, 99.9%), were used directly. Unphotolyzed sample was recollected after each experiment and frozen at liquid nitrogen temperature. This sample was then reclaimed and purified for further use.

4.3 Results and Analysis

4.3.1 Time-resolved IR emission spectra:

Chapter three of this thesis detailed the time-resolved emission spectra obtained following the 193 nm photolysis of ethyl ethynyl ether [10]. The collected spectra exhibit two main groups of features; one low energy feature near 2000 cm^{-1} and the other spanning various portions of the CH stretching region. In agreement with the prior photofragment translational energy spectroscopy (PTS) study of *Krish et al.* [11], the majority of the observed signal is assignable to the ketenyl radical. Of key importance for the current study, it was observed that the ν_1 CH stretch of HCCO undergoes a substantial anharmonic shift with an onset around 2700 cm^{-1} and continues up to the measured fundamental at 3232 cm^{-1}; indicating that the nascent radicals were generated with a massive amount of internal energy. In addition to HCCO, other key features observed in the spectra include vibrationally excited carbon monoxide (CO, generated from the secondary dissociation of rovibronically excited HCCO) as well as electronically excited ethynyl (HCC) radical. The majority of the signal arising from the ethynyl radical originally appears in the $\tilde{X} \leftarrow \tilde{A}$ electronic transitions spanning 3600-3800 cm^{-1}, after which there is a near constant presence of the ground state ν_1 CH stretch fundamental near 3298 cm^{-1}.

As mentioned in the previous chapter, there is some minor overlap between the fundamental CH stretch transitions of both HCCO and ethynyl. However, given

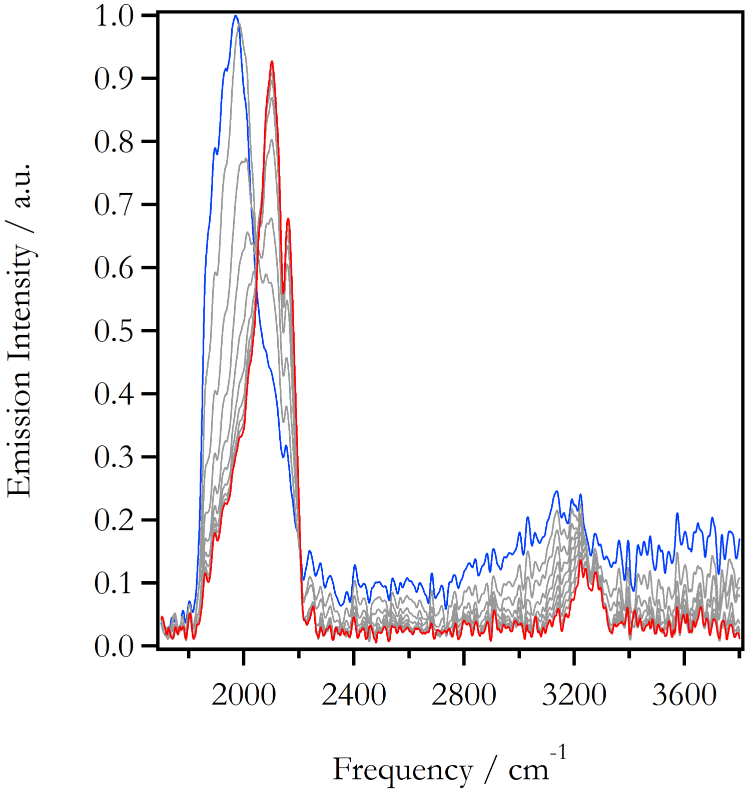

Figure 4.2
Time–resolved emission spectra following the 193 nm photolysis of ethyl ethynyl ether. The earliest and latest spectra have been highlighted in blue and red, respectively, to showcase the temporal dependence of the observed features.

the low energy origin of the ethynyl signal, the observed overlap is limited to the fundamental transition and has no significant effect on the anharmonic portions of the ν_1 CH stretching transitions of the HCCO spectrum. Alternatively, the low energy cutoff of the InSb detector limits the collection of high energy transitions originating from the ν_2 asymmetric CCO stretch of HCCO; whose fundamental lies at 2023 cm^{-1}. This experimental limitation, coupled with the observed anharmonically shifting CO feature, suggests that any signal arising from the ν_2 mode of HCCO will likely be completely convoluted with diatomic CO. Nevertheless, the relatively clean (overlap free) signal originating from the extremely anharmonic ν_1 CH stretch transitions of HCCO serve as a novel probe of the internal energy of the radical. Furthermore, the time-resolved nature of the experiment permits the opportunity to examine the evolution of the nascent internal energy and hence characterize the energy transfer properties of this open-shelled species. In the interest of restricting secondary reaction, we limit our examination to vibrational-to-translational (V-T) energy transfer via the inert rare-gas colliders helium (He), neon (Ne), and argon (Ar). To that end, the photolysis reaction was repeated and a set of time-resolved spectra were collected under near identical conditions save that the identity of the collisional quencher was varied. Figure 4.2 portrays a representative set of emission spectra obtained using Ar as a collisional quencher in which the earliest and latest spectra have been highlighted in blue and red, respectively. As should be expected, variation of the collisional collider does not change the features that are observed, but rather alters the relative temporal evolutions of those features.

4.3.2 Photodissociation product population distributions:

It has been well established that an anharmonically shifting feature observed in time-resolved emission spectra can be used to measure the internal energy content of the associated species [12-16]. The core of the analysis relies on the ability to calculate the associated vibrational manifold up to the experimentally appropriate internal energy using both the harmonic (ω_i) and anharmonic ($\chi_{ij}, y_{ijk}, z_{ijkl}...$) spectral constants obtained from high resolution spectroscopic studies. For each available energy level, a transition frequency is obtained as the energy difference between a given level and the corresponding lower energy level as defined by appropriate selection rules. Additionally, it is assumed that the intensity of the individual transitions follow the harmonic scaling rule (e.g. $I^{em}_{\nu-1\leftarrow\nu} = \nu I^{em}_{0\leftarrow1}$) [17]. Once the allowed transition frequencies and intensities have been determined, a calculated emission spectrum can be obtained by imposing a population distribution $P(E_j)$ over the calculated energy levels:

$$S(\nu) = \sum_j P(E_j) I^{em}_j g(\nu), \tag{4.5}$$

where I^{em}_j refers to the emission intensity of a given transition from energy level E_j and $g(\nu)$ is a convolution function (typically a Gaussian or Lorentzian) which provides a spectral width to each transition. Prior examples from this lab include the modeling of nitrogen dioxide (NO_2) [12], sulfur dioxide (SO_2) [14], and carbon disulfide (CS_2) [13] in energy transfer studies as well as deuterated acetylene (DCCD) and hydrogen isocyanide (HNC) following the photodissociation of perdeuterated vinyl cyanide and vinyl cyanide, respectively [18].

In our original emission modeling studies [12-16], the collected spectra possessed features containing only vibrational resolution. As a result, the calculated emission spectra were modeled as pure vibrational transitions. The bandwidth and shape of the various features were treated as Gaussian functions whose width matched that of the associated infrared absorption transitions. In more recent studies however, while complete rotational resolution is not practical, at least partial resolution of the rotational contours is observed. For these spectra, the calculated emission bands are generated as the sum of the available rovibrational transitions. Intensities for each rovibrational transition permitted by the ($\Delta\nu = -1,\ \Delta J = 0, \pm 1,\ \Delta K = 0, \pm 1$) selection rules were calculated as [18]:

$$I^{em}_{\nu,J,K} = L_{\upsilon}\nu^{4}_{n,m}|\mu_{0\leftarrow 1}|^{2}S^{PQR}_{J,K}exp\left(\frac{-hcE_{\upsilon,J,K}}{k_{B}T_{rot}}\right), \tag{4.6}$$

in which $\nu_{n,m}$ corresponds to the frequency of the (m←n) rovibrational transition, $|\mu_{0\leftarrow 1}|$ the fundamental transition dipole moment, $S^{PQR}_{J,K}$ are the symmetric top Hönl-London factors [19], and L_{υ} is the vibrational line strength factor defined by the harmonic scaling rule [17]. As in prior studies [18], a constant rotational temperature (T_{rot}) of 300 K is used throughout to model the rotational distribution. This assumption is not invoked to suggest that the nascent species are generated in rotational equilibrium. On the contrary, it is quite possible that the associated species are initially created with rotational temperatures many times larger than a room temperature distribution. The validation of such an assumption comes in to play through the wide distribution of initially available vibrational states. The earliest times, well before the species of interest is rotationally quenched through inert gas collisions, correspond to the point of the largest vibrational temperature and hence the point at which the rotational temperature is least discernable. The rotational contour is only partially resolved after a large number of inert collisions, at which time the rotational distribution is effectively quenched. As further justification of this point, figure

4.3 shows a comparison of the calculated emission spectra for the ν_1 CH stretch of HCCO at various vibrational temperatures (internal energy distributions) with fixed rotational temperatures of 300 K versus 1,000 K. As expected, for low vibrational temperatures (consistent with late times) a variation of the rotational temperature is very apparent. Alternatively, for high vibrational temperatures (consistent with early times) an apparent invariance of rotational temperature is observed. Thus, for TR-FTIRES data at least, the rotational temperature is only measurable at later

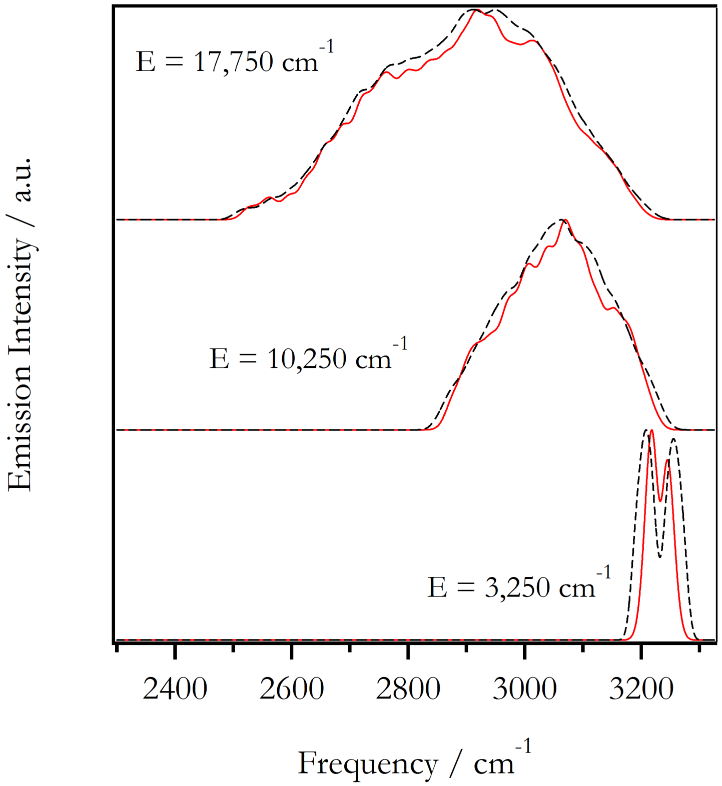

Figure 4.3

Calculated emission spectra of the ν_1 CH stretch of HCCO modeled with increasing internal energies (vibrational temperature distributions) for static rotational temperatures of 300 K(red, solid line) and 1,000 K (black, dashed line).

times after the vibrational temperature has been quenched. However, as the rotational temperature quenches so much faster than the vibrational temperature, we feel justified in using a global rotational temperature of 300 K.

When modeling systems to high internal energies, or simply any system for which rotational degrees of freedom have been included, the number of available transitions quickly becomes prohibitively cumbersome to work within the context of a spectral fitting routine. One simplifying solution that we have found useful is to partition all of the available transitions into equally spaced 500 cm^{-1} wide energy bins. Invoking an assumption of equal population of all levels within a given bin, a representative energy bin spectrum can be constructed by summing over all allowed transitions and dividing through by the total number of transitions. Such a procedure allows one to convert a series of many thousands of transitions into a series of (depending upon the maximal internal energy considered) many tens of transitions, which is much more tractable to work with. The resulting series of bin spectra can then be used to model the measured time-resolved spectra through any of the simple nonlinear least-squares fitting procedures.

4.3.2.1 Modeling IR emission from HCCO ν_1:

Closed-shell molecular species, typically containing less than four or five atoms, have historically been employed as fruitful laboratories to model much of the complexity of chemistry [20-25]. The limited number of interactions permits the generation of an tractable effective Hamiltonian from which spectroscopic studies can be used as an efficient probe of a desired effect. This utility of smaller molecules has resulted in a wealth of information recorded in the literature, including the characterization of spectral constants which has made much of our prior analysis feasible. For the current study however, as is so often the case for polyatomic radicals, comparatively little is known experimentally about the spectral constants of HCCO. In particular, at present only three of the six fundamental vibrational modes of HCCO have been experimentally measured [10,26,27]. Additionally, while there have been numerous theoretical studies examining the spectroscopy of HCCO (and radicals in general), rovibrational anharmonic constants are rarely (if ever) reported in the literature. As such, it becomes necessary to turn to commercially available theoretical programs as a means to supplement the missing experimental values necessary to generate a representative spectral manifold. Following the work of Barone [28,29], there are now methods available within the quantum chemistry program GAUSSIAN [30] that permit examination of the anharmonic portions of the potential energy surface through second-order perturbation theory (PT2). In particular, PT2 allows the calculation of the second-order vibrational anharmonic constants (χ_{ij}) via theoretically evaluated higher order energy derivatives.

For the current study, the anharmonic vibrational constants (χ_{ij}) of ground state HCCO were calculated at the UB3LYP / aug-cc-pVQZ level of theory. The resulting constants yielded vibrational term values that were in excellent agreement with both the available experimental as well as high-level theoretical data, providing further confidence for their use. Using equations 4.1 and 4.2, a theoretical rovibrational manifold of HCCO was generated for energies up to 20,000 cm^{-1} above the zero point energy. As discussed previously, while the collected emission spectra show the presence of both the ν_1 CH and ν_2 asymmetric CCO stretch of ketenyl, only the ν_1 mode is unobstructed by transitions from other species. Our simulation will therefore focus solely on the emission spectra of the ν_1 CH stretch mode. Using the calculated spectral manifold of the available HCCO rovibrational levels, transitions allowed by the rigid-rotor / harmonic oscillator selection rules: ($\Delta\nu = -1$, $\Delta J = 0, \pm1$, $\Delta K = 0, \pm1$) will be used to calculate the ketenyl emission spectra. Additionally, it is important to note that one of the key results of the PTS study [11] was that HCCO was generated in two distinct energetic distributions, one high recoil distribution (low internal energy) and one low recoil distribution (high internal energy). To account for the possibility that the observed emission spectra are the result of two distinct energetic distributions of HCCO, a bimodal distribution was initially applied in the fitting routine. Specifically, the population distribution was modeled as the sum of a low-energy distribution defined by a temperature and a high energy Gaussian function:

$$P(E_j) = \frac{\alpha_1}{\sqrt{2\pi}} exp\left(\frac{-E_j}{k_B T_{vib}}\right) + \frac{\alpha_2}{\sqrt{2\pi}\sigma} exp\left(\frac{-(E_j - \langle E\rangle)^2}{2\sigma^2}\right), \tag{4.7}$$

in which α_1 and α_2 are relative scaling factors, T_{vib} is the vibrational temperature describing the low energy distribution, and $\langle E\rangle$ and σ define the Gaussian function of the high energy distribution. Nevertheless, when the above dual population distribution is employed, it is observed that only a single population (described by a vibrational temperature) is required to fit the measured emission spectra. This suggests that either the dual populations observed in the PTS study are simply unresolvable by TR-FTIRES, or that one of the two distributions was simply lost to secondary reaction or dissociation.

Using the first term of equation 4.3, the time-resolved spectra were fit to a series of vibrational temperatures. As in prior studies [18], each vibrational distribution can be directly related to an average energy; yielding the average internal energy as a function of time. Figure 4.4 is a contour plot of the internal energy distribution of ketenyl, measured as a function of time, when quenched by Ar. We note however that, given the nature of the experiment, time is actually a poor metric of comparison when considering the different collisional frequencies of the three colliders. Rather, it is more instructive to discuss the energetic evolution in terms of the number of collisions. When the associated average energies are plotted as a function of the number of collisions, it is found that the evolution of the internal energy can be well described by a double exponential function. This observation is reasonable given that there are two seperate sources of ground state HCCO, namely nascent $\tilde{X}^2$ HCCO as well as $\tilde{X}^2$ HCCO resulting from intersystem crossing from nascent $\tilde{a}^4$ HCCO. Extrapolation

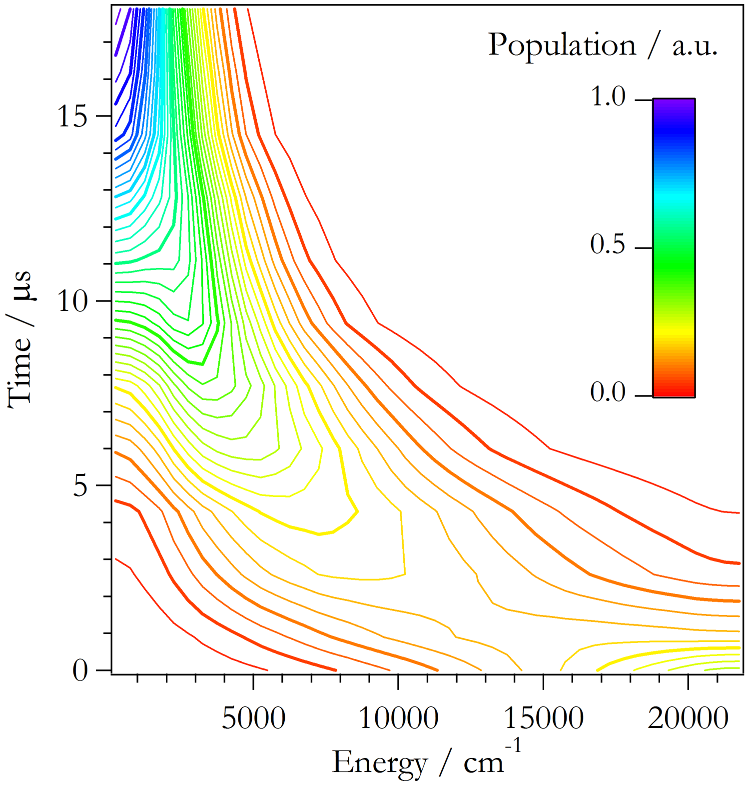

Figure 4.4
Evolution of the measured internal energy of HCCO as a function of the time.

of the functional form back to the zero-collision region, for all three inert colliders, yields a common nascent HCCO internal energy of about 20,100±500 cm^{-1} (2.49±0.1 eV). Figure 4.5 highlights the comparison of the measured evolution of the HCCO internal energies for the series of rare-gas colliders. It is observed that Ne is the most efficient collider, as evidenced by the fastest decrease in internal energy, followed next by He and finally Ar.

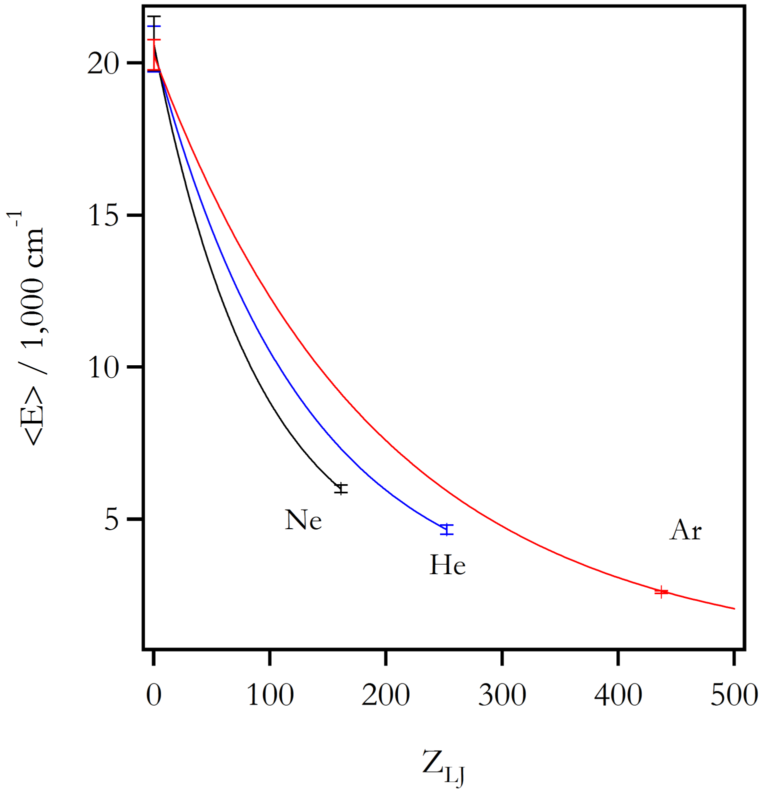

Figure 4.5
Measured results of the average internal energy of HCCO, as a function of the number of rare-gas collisions, for each of the three colliders He, Ne, and Ar.

4.3.2.2 Calculation of $\langle \Delta E \rangle$ versus $\langle E \rangle$:

The time-dependant average internal energy of the ketenyl radical can be directly related to the number and efficiency of the various collisions the radical encounters [15], i.e.:

$$d\langle E \rangle = \sum_m Z_{LJ}(m) P_m \langle \Delta E \rangle_m dt, \tag{4.8}$$

in which $Z_{LJ}(m)$ is the Lennard-Jones collisional frequency, P_m is the partial pressure, and $\langle \Delta E \rangle_m$ is the average energy lost per collision of species (m). For the current study, the radical of interest is generated through the photolysis of the precursor species ethyl ethynyl ether. More specifically, the photolysis cell contains about 4,000 mTorr of the rare-gas collider (either He, Ne, or Ar) and 10 mTorr of the precursor cocktail (50% ethyl ethynyl ether, 50% hexanes). For the current setup, only about ca. 10% of the ethyl ethynyl ether undergoes photolysis, yielding at most about 0.5 mTorr of photofragments (of which about 90% will correspond to ketenyl and ethyl radicals [31]). Furthermore, the PTS [11] results suggest that HCCO is generated in two distinct energetic distributions; 37% in a stable high recoil distribution, and 63% in a low recoil distribution which is expected to undergo secondary dissociation (following intersystem crossing from the $\tilde{a}^4$ state). In this regard, the calculated partial pressure of the rare-gas (Rg) collider is about (9,000 - 24,000) times greater than HCCO, implying the time-dependence of the internal energy of the radical will clearly be dominated by the rare-gas collisions, and hence:

$$d\langle E \rangle \approx Z_{LJ}(Rg) P_{Rg} \langle \Delta E \rangle_{Rg} dt. \tag{4.9}$$

Once again, the number of collisions ($Z_m = Z_{LJ}(m) P_m t$) is a much more useful tool for describing the energetic evolution as a function of the various colliders, hence the average energy lost per collision can be derived as:

$$\langle \Delta E \rangle_{Rg} = \frac{d\langle E \rangle}{dZ_{Rg}}. \tag{4.10}$$

The utility of the above equation is that we have already shown that the average internal energy, for each inert collider, can be expressed in closed form as an analytical (differentiable) function in Z_{Rg}. Differentiation with respect to Z_{Rg} therefore yields an experimental measure of the average energy lost per collision:

$$\langle \Delta E \rangle_{Rg} = -\left\{ \tau_1 A_1 exp\left(-\tau_1 Z_{Rg}\right) + \tau_2 A_2 exp\left(-\tau_2 Z_{Rg}\right) \right\}, \tag{4.11}$$

for each of the three colliders examined.

Similar to the results of figure 4.5 above, figure 4.6 highlights the average energy lost per collision as a function of internal energy for the three colliders. Once again, it is observed that the rare-gas colliders show a seemingly nonsensical reduced mass trend in that Ne is measured to be the most efficient collider followed by He then Ar. Additionally, as contrasted against prior studies of similar sized closed-shell molecules [12-16], V-T energy transfer is observed to be extremely efficient with values of $\langle \Delta E \rangle > 10\ cm^{-1}$ for all measured internal energies. We note that efficient V-T energy transfer has been observed in prior studies of excited radical species. In particular, the UV absorption study by Damm *et al.* examined the collisional deactivation of vibrationally highly excited benzyl ($C_6H_5CH_2$) radicals with Ar. When their reported data is reinterpreted in terms of the average energy lost per collision, it is observed that the benzyl radical (when quenched with Ar) compares favorably with our measured results for the ketenyl radical. Figure 4.7 compares the energy transfer efficiency of benzyl and ketenyl; while the two radicals exhibit

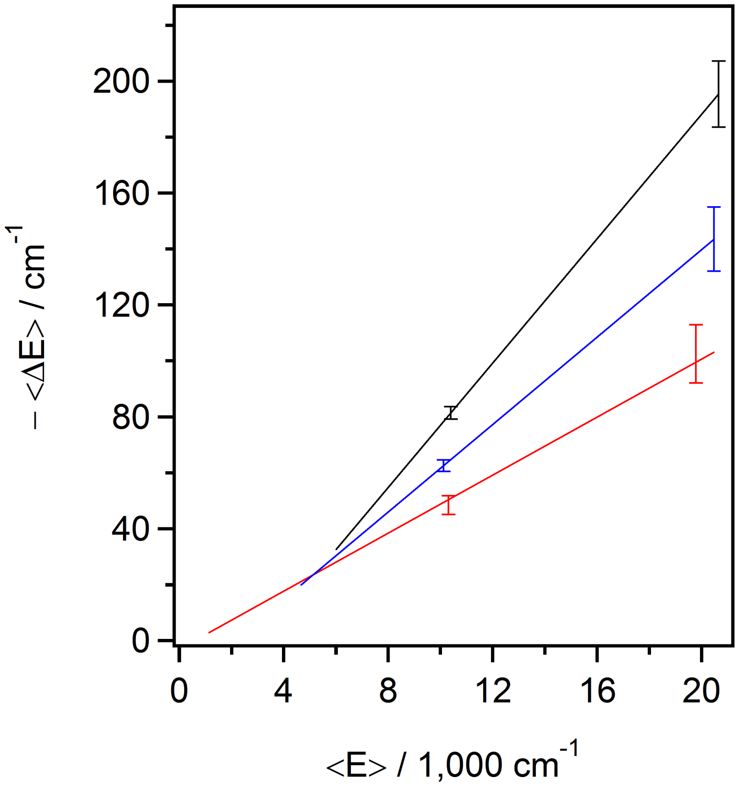

Figure 4.6
Measured results of the average HCCO internal energy lost per collision with the various rare-gas colliders (He, Ne, Ar), as a function of the average HCCO internal energy.

similar $\langle \Delta E \rangle$ magnitudes, benzyl is found to be more efficient due (very likely) to the greater availability of low energy bending motions. Furthermore, compared with earlier studies of closed-shell species [12-16], there is no apparent *onset* of enhanced $\langle \Delta E \rangle$ efficiency. Previously, it has been observed that enhanced $\langle \Delta E \rangle$ efficiency is directly related to electronic coupling [15] which shows up in the $\langle \Delta E \rangle$ vs. $\langle E \rangle$ plot as a distinct *elbow* in which the efficiency increases at the energetic onset of the electronic state. For the current case of the ketenyl radical however, there is a distinct relative enhancement of $\langle \Delta E \rangle$ for all values of $\langle E \rangle$ but with an constant linear trend.

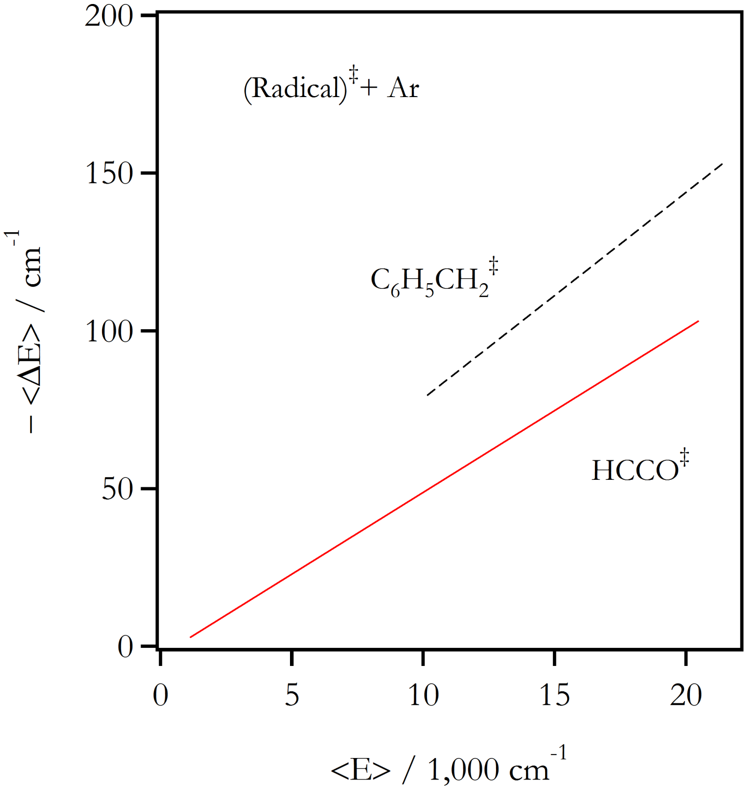

Figure 4.7
Comparison of the average internal energy lost per collision with Ar for the ketenyl and benzyl radicals. The benzyl radical data was derived from figure 7 of Damm et al. *[32] as follows: The average energy (as a function of the number of Lennard-Jones collisions Z_{LJ}) was measured as the center peak of each of the energy dependent population distributions. The average energies (as a function of Z_{LJ}) were fit to a double exponential functional form from which the average energy lost per collision was then determined as in equation 4.7.*

4.4 DISCUSSION

4.4.1 Comparison with the PTS study:

The PTS study of *Krish et al.* [11] provided the initial experimental conformation that the photolysis of ethyl ethynyl ether at 193 nm yields the ketenyl radical with near unit quantum efficiency. Their detailed results concerning the energetics and distributions of the ketenyl radical serve as a convenient basis for comparison against our current experimental observations. In particular, they observed that ketenyl is generated in two distinct kinetic distributions; 37% in the ground $\tilde{X}^2$ state and the remainder in the excited $\tilde{a}^4$ state. Using conservation of available energy as a guide, the average internal energies of the two energetic distributions can be determined as 2.4 eV and 3.6 eV, respectively. We note coincidently that our measured value of the nascent internal energy of the radical (2.5±0.1 eV) is in excellent agreement with the high recoil (low internal energy) $\tilde{X}^2$ state distribution. As mentioned previously, the majority of the $\tilde{a}^4$ state of ketenyl is calculated to lie above the dissociation barrier of the ground $\tilde{X}^2$ state [3]. While the collisionless environment of the PTS study would permit the observation of a long-lived quartet state, the (relatively) high pressure environment of our TR-FTIRES study would certainly enhance the probability of a collision-induced intersystem crossing (CIISC) pathway.

In terms of the current system, CIISC would predominantly result in a secondary dissociation process in which the majority of the low recoil HCCO population would be converted into methylidyne (CH) and CO. The observation of vibrationally excited CO in our emission spectra, in proportions similar to the observed HCCO signal, provides strong evidence for the occurrence of the CIISC mechanism. Furthermore, our measurements of the nascent internal energy were only able to support the presence of a single HCCO distribution. The fact that the single distribution had a measured internal energy consistent with the PTS results provides further support not only for the CIISC mechanism but also (and more fundamentally) for the validity of the calculated anharmonicity constants. In this regard, we find that the combined experimental results of both the PTS study and our current work suggests that the following dominant reaction pathways are occurring:

$$EEE \longrightarrow CH_2CH_3 + HCCO^{\ddagger}(\tilde{X}^2A'') \tag{4.12}$$

$$EEE \longrightarrow CH_2CH_3 + HCCO^{\ddagger}(\tilde{a}^4A'') \longrightarrow CH_2CH_3 + CH + CO(\nu > 8), \tag{4.13}$$

in which ground state HCCO$^{\ddagger}(\tilde{X}^2A'')$ is generated with 2.5±0.1 eV of nascent internal energy.

4.4.2 SSH(T) calculations:

The theory of vibrational relaxation through collisional interactions was worked out in great detail by Schwartz, Slawsky, and Herzfeld (SSH) [4] in the early 1950's, and latter modified by Tanczos (T) [33]. The core of the analysis revolves around the determination of the probability of a given transition from either of the two colliding species. At the heart of SSH theory, most of the attention is focused heavily upon the repulsive asymptote of the collisional interaction potential, which is chiefly modeled through comparison against the associated Lennard-Jones (LJ) potential. One of the key predictions from the original SSH theory (when focusing solely on V-T energy transfer) [4] is a well-behaved reduced mass dependence in which the lightest colliders are found to be the most efficient quenchers. For the present case of the ketenyl radical however, we have already established that a clear reduced mass dependence, consistent with SSH theory, is not observed as Ne is found to be more efficient than He. In the subsequent modification of SSH theory by Tanczos [33] (SSHT), a term associated with the long-range attractive interaction was included via an exponential coefficient which contained the associated LJ well depth (D_e). It is of interest to note that one of the potential side effects of Tanczos's exponential factor should be a variation of the resulting slopes for the transition probabilities as a function of energy. In this regard, application of the modified SSHT theory could potentially provide insight into the deviations of the reduced mass trend observed in the collisional deactivation of the ketenyl radical.

4.4.2.1 Calculating values of $\langle \Delta E \rangle$:

To calculate the probability of a given collision induced transition of the ketenyl radical from initial state $|\phi_i\rangle$ to final state $|\phi_j\rangle$ by rare-gas atom R_g, we apply the modified equations of SSHT theory [33,34], i.e.:

$$P^{j \leftarrow i}_{HCCO,R_g} = \langle \phi_j | V | \phi_i \rangle^2 \Gamma(\Delta E, D_e, \mu) \int_0^{\infty} \Theta(\Delta E, \mu, v) dv, \tag{4.14}$$

wherein the initial matrix element is treated as the associated harmonically scaled transition dipole moments, and the functions $\Gamma(..)$ and $\Theta(..)$ (which detail the dependence upon the reduced mass μ, magnitude of the energy transferred ΔE, and the attractive portion of the interaction D_e) can be expressed as:

$$\Gamma(\Delta E, D_e, \mu) = \left(\frac{8\pi^3 \mu \Delta E}{\alpha^{*2} h^2} \right)^2 \left(\frac{4\mu}{k_B T} \right) exp \left(\frac{-D_e}{k_B T} \right) \tag{4.15}$$

$$\Theta(\Delta E, \mu, v) = v \; exp \left(\frac{-\mu \Delta E^2}{2 k_B T} \right) \left[\frac{\chi(v)}{\{1 - \chi(v)\}^2} \right], \tag{4.16}$$

in which α^* relates to the curvature of the associated LJ potentials and the velocity dependent function $\chi(v)$ is defined as:

$$\chi(v) = exp \left(\frac{4\pi^2 \mu}{\alpha^{*2} h} \right) \left[v - \sqrt{v^2 + \frac{2\Delta E}{\mu}} \right]. \tag{4.17}$$

For a given initial state $|\phi_i\rangle$, there exists a variety of potential downward transitions to state $|\phi_j\rangle$, each with a specific transition probability $P^{j\leftarrow i}$. To account for all the allowable transitions, a total transition probability $P(E_i)$ as a function of energy can be defined as the sum over all the individual transition probabilities originating from an energy E_j:

$$P(E_i) = \rho(E_i)^{-1} \sum_k P^{k\leftarrow i}, \tag{4.18}$$

to a set of allowed lower energies $\{E_k\}$; divided by the total number of allowable transitions $\rho(E_i)$. Once the vibrational manifold as well as the energy dependent transition probabilities have been calculated, the average energy lost per collision can be obtained as a sum over the probability weighted energy gaps:

$$\langle \Delta E \rangle = \sum_i P(E_i) \langle \Delta E_i \rangle, \tag{4.19}$$

which allows for a semi-direct comparison against our experimental observations. We note additionally that our treatment of Tanczos's method [33] evaluates the velocity dependent integral of equation 4.8 numerically as opposed to relying on the implementation of approximate analytical techniques.

As in the original formulation of SSH theory [4], evaluation of equations (4.8–4.13) with zero attractive interactions (i.e. $D_e = 0$) yields the classically expected reduced mass trend in which He is the most efficient quencher, followed by Ne and finally Ar. As expected, however, when the attractive interactions are allowed to grow in, we find that the reduced mass trend begins to shift. Specifically, for a given rare-gas collider, it is observed that the smallest probability of a transition occurs for the zero attractive interaction ($D_e = 0$). As the attractive interaction is turned on ($D_e > 0$), the relative probability of a transition increases. In this regard, the measure of the long-range attractive interaction (D_e) can be used as a tool to model, and hence explain the observed reduced mass dependencies.

4.4.2.2 Fitting $\langle \Delta E \rangle$ vs. $\langle E \rangle$ - the effect of attractive interactions:

For all energies examined, the calculated $\langle \Delta E \rangle$'s were found to obey a linear functional form in which the only common overlapping point, for each of the three

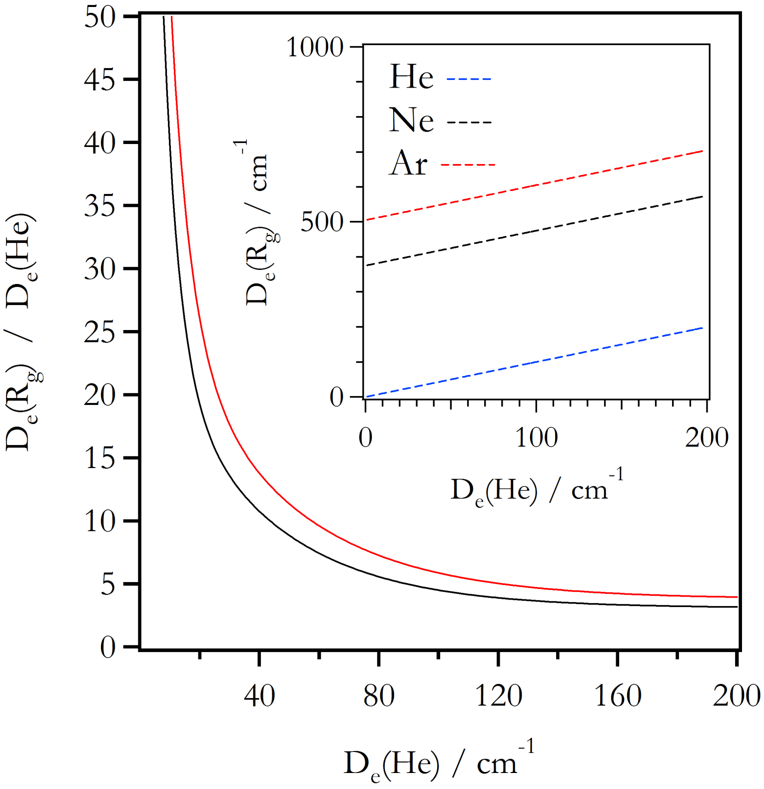

Figure 4.8
The various possible ratios of the Ne and Ar interaction energies with the ketenyl radical, relative to He, for energies less than 200 cm^{-1}. The inset show the linear trends of the three interaction energies in which the differences between the interaction energies are observed to be relatively invariant at $\Delta D_e(Ne, He)$ = 375 cm^{-1} and $\Delta D_e(Ar, He)$ = 505 cm^{-1}.

colliders, was the zero origin. As can be observed in figure 4.6, however, the three-colliders don't actually overlap until about 5,000 cm^{-1}, after which the three trends obey a linear functional form. Thus, fittings of the experimental plots can only reasonably be obtained if the common overlap point is transferred to the origin. In this approach, the reduced mass trend can be analyzed through the slopes of the $\langle \Delta E \rangle$ vs. $\langle E \rangle$ plots, however the calculated magnitudes of the $\langle \Delta E \rangle$ values begin to lose their meaning. We note therefore, that for the current analysis, SSHT theory was employed with the sole intent of obtaining the relative $\langle \Delta E \rangle$ values for each inert

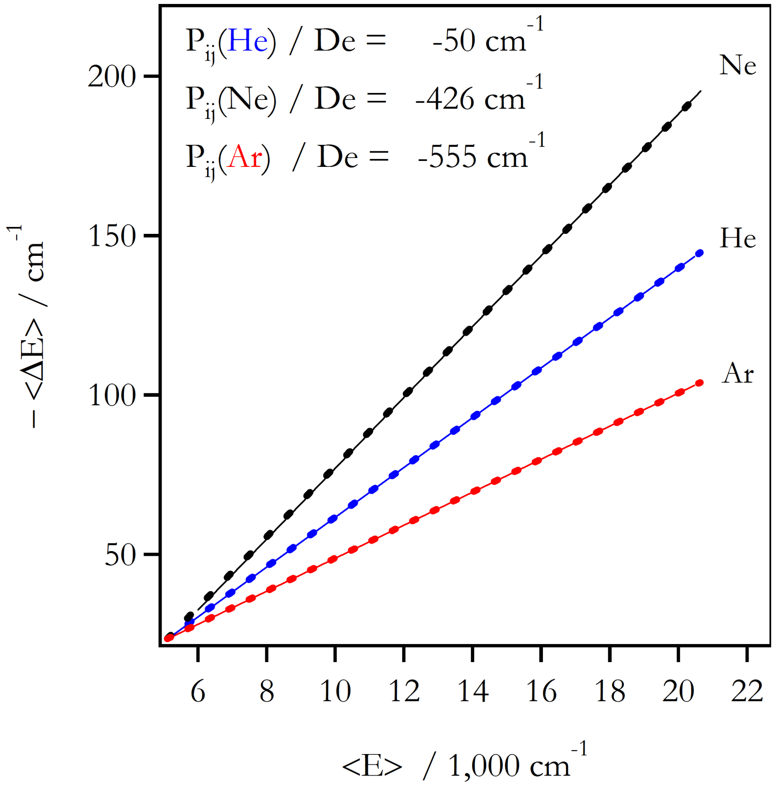

Figure 4.9

Relative fittings of the HCCO + R_g $\langle \Delta E \rangle$ vs. $\langle E \rangle$ plots in which the HCCO / He interaction energy was arbitrarily fixed at -50 cm^{-1} and the remaining Ne and Ar interaction energies were left as fitting parameters.

collider, for use in relative fittings of the experimental data. One obvious drawback of a relative fit is that, as one is free to choose the initial point of comparison (in this case the magnitude of the ketenyl / He interaction energy), there necessarily exists an infinite set of possible solutions. As an example of this point, figure 4.8 highlights the various possible Ne and Ar interaction energies as a function of a fixed He interaction energy. It is of interest to note that the collider interaction energies follow a near constant linear trend in which Ne and Ar are found to be larger than He by 375 cm^{-1} and 505 cm^{-1}, respectively. Once again, we note that each of the solution sets observed in figure 4.8 yield accurate fittings of the experimental data shown in 4.6. Furthermore, regardless of the solution set applied, it is found that the unexpected (non-SSH) reduced mass dependencies observed in the $\langle \Delta E \rangle$ vs. $\langle E \rangle$ plots (when analyzed with SSHT theory) yield physically plausible trends in the associated collider interaction energies. An example of one such fit is highlighted in figure 4.9 in which a fixed He interaction energy of D_e = -50 cm^{-1} has been imposed. The remaining two interaction energies were left as variable parameters, in which fittings to the Ne and Ar data sets were obtained at interaction energies of D_e = -426 cm^{-1} and D_e = -555 cm^{-1}, respectively. In the next section, we will discuss the plausibility of enhanced interactions in radicals.

4.4.2.3 Enhanced attractive interactions in radicals:

It is important to exert caution when attributing meaning to the magnitudes of any of the interaction energies measured here, as the initial He interaction energy is always arbitrarily fixed. One useful check of the observed trend lies within the associated relative ratio of the three interaction energies. Specifically, it is reasonable to expect that a major component of the attractive interaction will be governed by the dipole-induced dipole moment generated in the electron cloud of the collider. In this regard, the ratio of the interaction energies should scale comparably (though not exactly) with the ratio of the associated atomic polarizability. For the series (He, Ne, Ar) employed here, the polarizability ratios of the three species when calculated as He:(He, Ne, Ar) are determined to be (1:2:8). Alternatively, the fit values portrayed in figure 4.9 yield ratios of (1:8:11), which contrast poorly with the predicted polarizability ratios. As observed in the main body of figure 4.8, variation of the fixed He interaction energy can produce a variety of such ratios. As a comparison, fixed He interaction energies of (-20, -100, and -200) cm^{-1} yield associated ratios of (1:20:26), (1:5:6), and (1:3:4). However, given the functional forms displayed in figure 4.9, a solution set yielding the exact ratio (1:2:8) is found to be impossible. Nevertheless, given the presence of the reactive unpaired electron on the ketenyl radical, it should be expected that the attractive interaction potential will be governed by more than the polarizability of the colliders. Consider the recent high-level theoretical study by Buchachenko *et al.* [35,36] in which interaction energies were calculated at the CCSD(T) level of theory for the rare-gas atoms in complexes with neutral and anionic atomic bromine. For the neutral species, the interaction energies for the series (He, Ne, Ar) were found in ratios of (1:2:8), in excellent agreement with the associated atomic polarizabilities. On the other hand, interaction energies for the same series with the anionic bromine were observed in ratios of (1:3:12), where the magnitudes of the interaction energies had increased due to an enhanced electrostatic interaction. In the same way, the unpaired electron in the ketenyl radical should enhance each of the interaction energies and hence should yield ratios which deviate from the polarizability predictions.

The experimental measurements presented here suggest that even with a fixed

He interaction energy of 0 cm^{-1}, Ne is expected to be bound with nearly 400 cm^{-1}; a value many times larger than a typical Ne / molecule Lennard-Jones well depth. Nevertheless, the enhanced absolute magnitudes of the average energy lost (for all energies examined) suggests that all three colliders, not just Ne and Ar, are interacting strongly with ketenyl. In this regard, He interaction energies of 50-100 cm^{-1} can be viewed as reasonable. However, further theoretical and experimental studies will be required before definitive values for the interaction energies can be assigned.

As an initial attempt however, we were able to perform modest potential energy scans of the HCCO / Rg system at the UMP2 / 6-311++G(2d,2p) level of

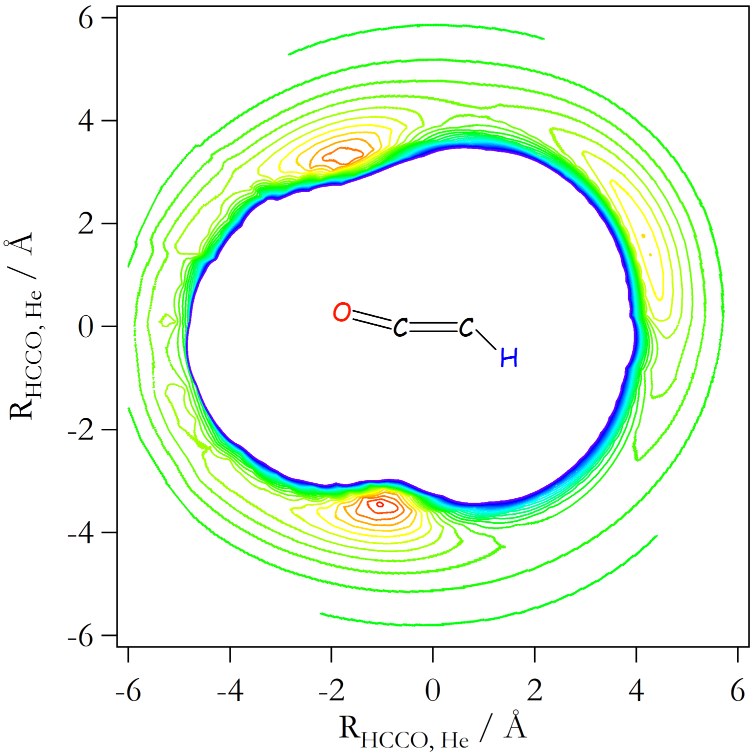

Figure 4.10
Two-dimensional potential energy surface scan, calculated at the UMP2 / 6-311++G(2d,2p) + (3321) level of theory, of atomic He approaching ground state HCCO radical in the molecular plane.

theory. In order to make the calculation more tractable, we limited the scope of the scans to the area containined within the molecular plane. Furthermore, the geometry of the radical was kept frozen at the calculated equlilibrium bond distances. Once global minima were found, additional calculations were performed at the more sophisticated UMP4(full) / aug-cc-pVTZ + (3321) level of theory (where the (3321) refer to a set of bond functions which were maintained midway between the center of mass of the radical and the approaching atom). We note additionally that all calculated energies were examined relative to a near infinite HCCO–Rg separation (i.e. $R_{Rg-HCCO}$ = 2,000 Å) and that basis set superposition error (BSSE) was treated by employing the counterpoise procedure of Boys and Bernardi [37]

Contrary to the expectation that the global minimum would appear near the unpaired electron (located on the carbon atom containing the hydrogen), figure 4.10 depicts that the two most prominent local minima actually occur near the C=O functional group. At the UMP4(full) level of theory, the global minima for He, Ne, and Ar were calculated to be -44.2, -76.5, and -193.7 cm^{-1}, respectively. These calculated values compare poorly with the SSH assisted measured values of -50, -426, and -555 cm^{-1}. Nevertheless, given that our PES sampled only a single plane of approach, it is quite reasonable to suggest that our calculation may have missed the true global minimum altogether. We note additionally that the calculated interaction energies were quite sensitive to both the method and the size of the basis sets employed. Furthermore, the magnitudes of the interaction energies were observed to increase when more sophisticated methods and basis sets were employed. Just the same, the overall trends observed in the experimental and calculated data sets are clear; Argon shows the strongest interaction with ketenyl, followed by Ne and finally He.

4.4.3 Validity of GAUSSIAN 03 *PT2 calculations:*

The core observation of the current study relies fundamentally on the measurement of the time-resolved internal energy of the ketenyl radical. As described above, this analysis is heavily predicated upon our ability to accurately model the spectroscopic manifold of the radical using theoretically derived anharmonicity constants. It is reasonable then that we should provide some insight as to why we believe that the calculated spectral constants are accurate and valid for use in such an analysis. In addition to the cited benchmarks of Barone [28,29], we have tested the applicability of PTS theory against the experimentally measured anharmonicity constants of various geometric isotopomers of hydrogen cyanide (HCN, HNC, DNC, and DNC) as determined by Maki *et al* [38-41]. Similar to our analysis of ground state ketenyl, the anharmonic spectral constants of the various isotopomers of hydrogen cyanide were evaluated at the B3LYP / aug-cc-pVQZ level of theory. For each isotopomer considered, when considered relative to the high-resolution absorption / emission spectra of Maki *et al* [38-41], PT2 analysis yielded remarkably accurate anharmonic constants with average standard deviations of less than 1 cm^{-1}. Subsequently, new sets of calculated emission spectra for the ν_1 CH stretch of HCCO were obtained with a ± 1 cm^{-1} variation applied to the originally calculated anharmonicity constants. When the Ar data set was re-analyzed with the modified calculated emission spectra, variations to the calculated average internal energies of no more than ± 500 cm^{-1} were obtained, well within the posted error bars.

As a further test of the accuracy of the calculated anharmonicity constants, we refer back to the comparable results of the PTS study [11] of Krish *et al.* The two kinetic distributions of the ketenyl radical were determined to possess internal energy distributions of 2.4 eV and 3.6 eV. As the high energy distribution is expected to undergo secondary dissociation under our experimental conditions, only a single ketenyl distribution (with 2.4 eV of internal energy) should be observable in our experiments. Once again, our measured nascent internal energy of the ketenyl at 2.5 ± 1 eV provides compelling support for the accuracy of the calculated anharmonicity constants.

4.4.4 Information theoretic examination of $|\langle \Delta E \rangle|$*:*

In a recent study [18], we applied the methods of information theory (as described by Muckerman)[42] as a means of quantifying the statistical partitioning of available internal energy following the photolysis of vinyl cyanide. In particular, it was found that the resulting internal energies of the main fragments (HCN, HNC, HCCN, and H_2CC:) were all well reproduced from a statistical analysis comparing the geometries of the precursor and the resulting photofragments. It is suggested that such an analysis is extremely well suited for describing product state distributions following unimolecular dissociations in which there is no reverse barrier to re-association (which would require an additional impulsive description). The SSHT assisted analysis of the ketenyl / rare-gas atom system discussed above, highlights the importance of the long-range attractive interaction between the radical and collider, implying the potential generation of a metastable complex. From this stand point, it is reasonable then to recast the notion of the radical / atom collision as a half-collision, in which the departing components of the collision complex are treated as fragments in a unimolecular dissociation. Information theory applied to such a system (a complex dissociating into an atom and a molecule) is of interest as it could provide a statistical measure of the translational energy partitioned to the retreating atom (i.e. the average energy transferred from the radical to the atom; $\langle \Delta E \rangle$). In this regard, information theory could provide additional evidence to support the strong (relative to closed shell species) interaction of ketenyl with the inert atomic colliders.

4.4.4.1 Statistical determination of $\langle \Delta E \rangle$:

For a given molecular complex composed of N_p-atoms which undergoes unimolecular dissociation into an atom and a molecule composed of (N_p-1) atoms, it is found that the average internal energy of the molecular fragment can be calculated as:

$$\langle E_{in} \rangle = \frac{k-3}{k} E_{avail}, \tag{4.20}$$

in which k relates directly to N_p as: $k = (6N_p - 11)$ for linear and $k = (6N_p - 12)$ for non-linear complexes. From here, the application of the conservation of both momentum and energy yield a direct measurement of the average translational energy of the departing atom, and subsequently the average energy lost per collision (e.g. $\langle \Delta E \rangle$) as:

$$\langle E_{trans}^{Rg} \rangle = \frac{3}{k} \frac{M_{molecule}}{M_{molecule} + M_{atom}} E_{avail} = \langle \Delta E \rangle, \tag{4.21}$$

wherein M_x refers to the associated mass of the individual fragments. The observed mass dependence, depicted by equation 4.15, shows a distinct similarity to the original formation of SSH theory. It is also important to note that one of the fundamental assumptions inherent in the above analysis is the complete randomization of the available total energy prior to the dissociation. Given the metastable nature of the radical / collider interaction, if complete energy randomization is not achieved; it is conceivable that equation 4.15 could significantly overestimate the energy partitioned into the departing atomic collider.

4.4.4.2 Comparison with experiment:

When equation 4.15 is applied to the ketenyl / rare-gas system (for average energies up to 20,000 cm^{-1}) a clear SSH reduced mass trend is observed. The agreement with the original SSH theory suggests that the assumed attractive interaction is invariant among each of the various colliders, i.e. the initial stance of the analysis is the existence of a bound complex. In agreement with the modified SSHT theory applied above, a common interaction energy (just like a zero interaction energy) favors transitions induced by lighter colliders. Additionally, as was suggested previously, it is observed that the calculated $\langle \Delta E \rangle$'s are off by about an order of magnitude, suggesting the need for an appropriate scaling factor. In particular, such a scaling factor should be required to account for the weak nature of the complex bond, and could provide insight into the relative strengths of the individual interactions. We note that, in a concurrent study from this lab [43], it has been observed that the above equation likewise overestimates (to a similar extent) the values of $\langle \Delta E \rangle$ measured in the collisional deactivation of HNC. Similar to ketenyl, HNC (considered to be a zwitterion) possess an exotic electronic configuration, in which partial charges are present on both the nitrogen and carbon centers. As such, it is reasonable to expect that enhanced attractive interactions will lead to more tightly bound complexes, and hence enhanced energy transfer probabilities. We note coincidently that, despite an incorrect reduced mass trend already discussed, when an additional (1/k) coefficient is added to equation 4.15 above, the calculated $\langle \Delta E \rangle$ magnitudes are in near quantitative agreement with the measured values for both the HNC and HCCO systems.

While such a scaling factor fails to provide insight into the measured interaction energies, and hence clearly requires a further scaling factor; the combined method of equation 4.15 with the (1/k) scaling factor provide a novel first order approximation of the expected average energy lost for a given radical system.

4.5 CONCLUSION

We have presented an experimental examination of the V-T energy transfer of vibrationally highly excited ketenyl radical, collisionally quenched through the rare-gas atomic colliders (He, Ne, and Ar). A series of time-resolved internal energy distributions were obtained through a GAUSSIAN assisted modeling of the anharmonic ν_1 CH stretch, observed in time-resolved emission spectra following the 193 nm photolysis of ethyl ethynyl ether. The average nascent internal energy of the radical was measured to be 2.5±0.1 eV, in excellent agreement with the stable high recoil kinetic distribution observed in the prior PTS study of Krish et al [11]. The dynamic evolution of the radical internal energies, as a function of the number of rare-gas collisions, were fit to analytical forms from which the average energy lost per collision (for each inert collider) was determined. It is found that the ketenyl radical exhibits a non-SSH reduced mass trend in which Ne is the most efficient quencher, followed by He and finally Ar. Additionally, similar to results for the benzyl radical [32], it is observed that the ketenyl radical exhibits overall enhanced energy transfer values in which $\langle \Delta E \rangle >$ 10 cm^{-1} (up to about 200 cm^{-1} at $\langle E \rangle$ = 20,000 cm^{-1}) is observed for all internal energies examined. Application of SSHT theory, in which the long-range attractive intermolecular interaction energy is incorporated into the original SSH theory, showed that the observed reduced mass trend actually correlates with a monotone increasing interaction energy trend in which D_e(Ar-HCCO) > D_e(Ne-HCCO) > D_e(He-HCCO). Furthermore, the deviation of the interaction energy ratios away from the associated atomic polarizabilities suggests that the unpaired electron of the radical is resulting in an enhanced interaction energy and thus a more efficient energy transfer process.

ACKNOWLEDGEMENT

This work is supported by Basic Energy Sciences, U.S. Department of Energy, through Grant No. DEFG 02–86ER 134584.

References:

1. J. A. Miller, R. J. Kee, and C. K. Westbrook, *Annu. Rev. Phys. Chem.* **41**, 345 (1990).
2. D. L. Osborn, D. H. Mordaunt, H. Choi, R. T. Bise, and D. M. Neumark, *J. Chem. Phys.* **106**, 10087 (1997).
3. C-. H. Hu, H. F. Schaefer III, Z. Hou, and K. D. Bayes, *J. Am. Chem. Soc.* **115**, 6904 (1993).
4. R. N. Schwartz, Z. I. Slawsky, and K. F. Herzfeld, *J. Chem. Phys.* **20**, 1591 (1952).
5. G. V. Hartland, W. Xie, D. Qin, and H-. L. Dai, *Rev. Sci. Instrum.* **63**, 3261 (1992).
6. L. Letendre, H-. L. Dai, I. A. McLaren, and T. J. Johnson, *Rev. Sci. Instrum.* **70**, 18 (1999).
7. D. K. Liu, L. Letendre, and H-. L. Dai, *J. Chem. Phys.* **115**, 1734 (2001).
8. M. J. Wilhelm, M. Nikow, and H-. L. Dai, *J. Mol. Struct.* **883-884**, 242 (2008).

9. D. L. Osborn, *J. Phys. Chem. A* 107, 3728 (2003).

10. M. J. Wilhelm, W. McNavage, R. Groller, and H-. L. Dai, *J. Chem. Phys.* **128**, 064313 (2008).

11. M. J. Krish, J. L. Miller, L. J. Butler, H. Su, R. Bersohn, and J. Shu, *J. Chem. Phys.* **119**, 176 (2003).

12. G. V. Hartland, D. Qin, and H-. L. Dai, *J. Chem. Phys.* **100**, 7832 (1994).

13. G. V. Hartland, D. Qin, and H-. L. Dai, *J. Chem. Phys.* **102**, 8677 (1995).

14. D. Qin, Ph.D. thesis, University of Pennsylvania, 1996.

15. G. V. Hartland, D. Qin, and H-. L. Dai, *J. Chem. Phys.* **107**, 2890 (1997).

16. C. D. Pibel, E. Sirota, J. Brenner, and H-. L. Dai, *J. Chem. Phys.* **108**, 1297 (1998).

17. E. B. Wilson, J. C. Decius, and P. C. Cross, *Molecular Vibrations: The Theory of Infrared and Raman Vibrational Spectra* (McGraw-Hill, New York, 1955).

18. M. J. Wilhelm, M. Nikow, L. Letendre, and H-. L. Dai, *J. Chem. Phys.* **130**, 044307 (2009).

19. R. Zare, *Angular Momentum: Understanding Spatial Aspects in Chemistry and Physics* (Wiley-Interscience, New York, 1988).

20. G. Herzberg, *Spectra of Diatomic Molecules, Molecular Spectra and Molecular Structure* (D. Van Nostrand Company, Princeton, NJ, 1939).

21. J. L. Steinfeld, R. N. Zare, L. Jones, M. Lesk, and W. Klemperer, *J. Chem. Phys.* **42**, 25 (1965).

22. H. Lefebvre-Brion and R. W. Field, *Perturbations in the Spectra of Diatomic Molecules* (Academic Press Inc.,Orlando, FL, 1986).

23. J. M. Smith, J. C. Bloch, R. W. Field, and J. I. Steinfeld, *J. Opt. Soc. Am. B* **12**, 964 (1995).
24. A. Shayesteh, S. Yu, and P. F. Bernath, *Chem. Eur. J.* **11**, 4709 (2005).
25. W. Xie, C. Harkin, and H-. L. Dai, *J. Chem. Phys.* **93**, 4615 (1990).
26. K. G. Unfried, G. P. Glass, and R. F. Curl, *Chem. Phys. Lett.* **177**, 33 (1991).
27. L. R. Brock, B. Mischler, E. A. Rohlfing, R. T. Bise, and D. M. Neumark, *J. Chem. Phys.* **107**, 665 (1997).
28. V. Barone, *J. Chem. Phys.* **120**, 3059 (2004).
29. V. Barone, *J. Chem. Phys.* **122**, 014108 (2005).
30. M. J. Frisch *et al.*, GAUSSIAN 03, Revision C.01, Gaussian, Inc., Wallingford, CT, 2004.
31. C. Fockenburg, *J. Phys. Chem. A* **109**, 7150 (2005).
32. M. Damm, F. Deckert, H. Hippler, and G. Rink, *Phys. Chem. Chem. Phys.* **1**, 81 (1999).
33. F. I. Tanczos, *J. Chem. Phys.* **25**, 439 (1955).
34. J. L. Stretton, *Trans. Faraday Soc.* **61**, 35 (1964).
35. A. A. Buchachenko, J. Klos, M. M. Szczesniak, G. Chalasinski, B. R. Gray, T. W. Wright, E. L. Wood, L. A. Viehland, and E. Qing, *J. Chem. Phys.* **125**, 064305 (2006).
36. A. A. Buchachenko, T. A. Grinev, T. G. Wright, and L. A. Viehland, *J. Chem. Phys.* **128**, 064317 (2008).
37. S. F. Boys and F. Bernardi, *Mol. Phys.* **19**, 553 (1970).

38. A. G. Maki, G. C. Mellau, S. Kee, M. Winnewisser, and W. Quapp, *J. Mol. Spectrosc.* **202**, 67 (2000).

39. A. G. Maki and G. C. Mellau, *J. Mol. Spectrosc.* **206**, 47 (2001).

40. A. G. Maki and R. L. Sams, *J. Chem. Phys.* **75**, 4178 (1981).

41. W. Quapp, M. Hirsch, G. C. Mellau, S. Kee, M. Winnewisser, and A. G. Maki, *J. Mol. Spectrosc.* **195**, 284 (1999).

42. J. T. Muckerman, *J. Phys. Chem.* **93**, 179 (1989).

43. M. J. Wilhelm, M. Nikow, J. M. Smith, and H-. L. Dai, (*In preparation*).

CHAPTER 5

Photodissociation of vinyl cyanide at 193 nm: Nascent product distributions of the molecular elimination channels[†]

[†] The majority of this chapter has been published in the *Journal of Chemical Physics* **130**, 044307 (2009).

5.1 Introduction

The photodissociation dynamics of small, unsaturated organic molecules such as ethylene as well as its various substituted analogs have been a subject of interest toward the fundamental understanding of reaction dynamics as well as their relevance to combustion, environmental, and atmospheric chemistry [1-11]. Beyond the case of ethylene, much attention has been focused on the halogen substituted variants, particularly vinyl chloride [6-9] and vinyl bromide [10-12]. Recent years have seen increasing attention to the more complex cyano-substituted species vinyl cyanide, also known as acrylonitrile [13-18].

Similar to other substituted vinyl species, it has been observed that vinyl cyanide exhibits strong absorption near 193 nm, with contributions predominantly from a $\pi^* \leftarrow \pi$ transition (centered at 203 nm) as well as a $\sigma^* \leftarrow \sigma$ (172.5 nm) and a $\pi^* \leftarrow n$ (217.0 nm) transition [19]. As with other substituted vinyl species, dissociation at 193 nm potentially results in four general reaction pathways; two radical and two molecular in nature [1-11]. However, the added complexity gained by changing the substituted functionality from a hydrogen (or halogen) to a heterogeneous diatomic species results in additional reaction pathways due to the potential presence of geometric isomers. Specifically, the various reaction channels available to vinyl cyanide at 193 nm, including unique electronic and/or bonding states, as well as their associated endothermicity can be summarized as follows [13,20]:

$$H_2CC(H)CN \rightarrow HCCH + HNC \qquad \Delta H_0 = 56\, kcal\, mole^{-1}, \quad (5.1)$$

$$\rightarrow: C = CH_2(^1A_1) + HCN \qquad \Delta H_0 = 86\, kcal\, mole^{-1}, \quad (5.2)$$

$$\rightarrow: C = CH_2(^3B_2) + HCN \qquad \Delta H_0 = 134\, kcal\, mole^{-1}, \quad (5.3)$$

$$\rightarrow HCCCN + H_2 \qquad \Delta H_0 = 50\, kcal\, mole^{-1}, \quad (5.4)$$

$$\rightarrow: C = C(H)CN(^1A') + H_2 \qquad \Delta H_0 = 90\, kcal\, mole^{-1}, \quad (5.5)$$

$$\rightarrow: C = C(H)CN(^3A') + H_2 \qquad \Delta H_0 = 140\, kcal\, mole^{-1}, \quad (5.6)$$

$$\rightarrow H_2C = CCN + H \qquad \Delta H_0 = 108\, kcal\, mole^{-1}, \quad (5.7)$$

$$\rightarrow H_2C = CH + CN \qquad \Delta H_0 = 131\, kcal\, mole^{-1}. \quad (5.8)$$

Most studies to date have examined the radical dissociation channel leading to cyano (CN) + vinyl (H_2CCH) largely by probing the state distribution of the CN photofragment [14,15]. With the exception of an early photofragment translational spectroscopy (PTS) study which suggested that the cyano loss channel accounted for nearly 75% of the total dissociation yield [21] most studies agree that the cyano + vinyl radical channel accounts for (at best) less than 1% of the total quantum yield [13-17].

In an attempt to detect the products resulting from reactions [(1)-(6)], Fahr and Laufer16 studied the photolysis of acrylonitrile–1d excited with 190 nm light using timeresolved UV absorption spectroscopy. The observation of known transitions assignable to deuterium cyanide (DCN) and triplet vinylidene (:C=CH$_2$[$^3B_2$]), coupled with the absence of transitions from hydrogen cyanide (HCN), suggested the dominance of reaction (3). Furthermore, their observations suggested that elimination involving CN in either the (X) [reaction (8)] or (A) electronic state account for less than 5% of the total quantum yield.

More recently, Blank et al. [13] updated the PTS results by incorporation of a tunable vacuum ultraviolet (synchrotron radiation) beam as an ionization source to gain insight into the internal energy content of the resulting photofragments. This most recent PTS study proposed that photodissociation at 193 nm proceeds with four main elimination channels describable by reactions: (1) and/or (2), (4) and/or (5), (7), and (8). Furthermore, it was suggested that all dissociation channels occurred on the ground electronic state following the internal conversion from the initially prepared S_1 state. However, with the exception of support for the minimal presence of reaction (8), the branching ratios of the remaining channels were left undetermined. Additionally, while it was suggested that the H_2 loss channels [reactions (4) and (5)] occurred competitively, there remained lingering doubts as to the relative importance of the three H(CN) loss reactions [(1)–(3)]. Contrary to the results of Fahr and Laufer [16], the presence of triplet vinylidene [as in reaction (3)] was readily excluded based on conservation of energy arguments. Nevertheless, it was still unclear whether the dominant H(CN) loss channel corresponded to a four-center elimination yielding HNC + acetylene [reaction (1)] or a three-center elimination yielding HCN + vinylidene ($^1A_1$) [reaction (2)]. The calculated reverse recombination barrier of the three-center elimination matched well against the measured average translational energy of the m/e (26 + 27) fragments and hence offered support for the dominance of the three-center elimination channel. However, the photoionization spectra suggested that the H(CN) fragment (then considered solely to be HCN) was generated with too much internal energy (2.6 eV) and hence could not have occurred via the three–center elimination channel.

A subsequent theoretical study by Derecskei–Kovacs and North, using transition states generated by *ab initio* methods for unimolecular Rice-Ramsperger-Kassel-Marcus (RRKM) dissociation rate calculations [17] concluded that the dominant molecular elimination channels are reactions (2) and (5); both of which occur through three–center transition states with calculated branching ratios of 0.593 and 0.152, respectively. Additionally, it was determined that the four–center H(CN) reaction occurred with the generation of HNC + acetylene, contrary to the prior expectation in which HCN was the common counterfragment for both three– and four–center eliminations [13]. Moreover, the calculated energy of the four–center transition state was predicted to be higher than that of the three-center transition state by nearly 10 kcal $mole^{-1}$, resulting in a substantial decrease in the calculated RRKM dissociation rate and thus a negligible branching ratio of 0.0012 for the reaction leading to HNC + acetylene.

In a prior study, we used time-resolved Fourier transform infrared emission spectroscopy (TR–FTIRES) to examine the dissociation fragments following the 193 nm photodissociation of vinyl cyanide [18]. IR emission from acetylene and hydrogen isocyanide, among other species, was detected, suggesting that reaction (1) was more significant than previously considered. The relative quantities of both hydrogen cyanide and cyanoacetylene were obscured, however, by the near resonant overlap of IR transitions associated with the fundamentals and combination bands of acetylene. As a result, it was initially unclear if the three-center elimination channel, reaction (2), yielding HCN + vinylidene ($^1A_1$) was important.

In what follows, we report observations made following the photodissociation of deuterated vinyl cyanide in an attempt to decouple the overlapping transitions and hence finally discern the relative presence of HNC [reaction (1)] versus HCN [reaction (2)]. Using perdeuterovinyl cyanide, the difference between the CH fundamental stretching transitions of acetylene and hydrogen cyanide, a mere 22 cm^{-1} in the protonated form, become much more substantial (191 cm^{-1}) and can hence be resolved in the IR emission spectra. A detailed analysis of the TR–FTIRES data recorded following the 193 nm photodissociation of both vinyl cyanide and perdeuterovinyl cyanide yields the first experimental relative branching ratio of the three– versus four–center elimination of $C_2H_2 + H(CN)$. Furthermore, the superior frequency resolution of the deuterated spectra provides an opportunity to assess the relative presence of cyanoacetylene and challenge the prior RRKM prediction [17] that the three–center H_2 elimination [reaction (5)] is the dominant loss channel.

5.2 EXPERIMENTAL

A more detailed description of the experimental setup has been given elsewhere [11,18,22-25]. Briefly, the output from an ArF excimer laser ($\lambda = 193nm, 20Hz, \leq 50mJ/pulse$) (Lambda Physik, LPX 200) was collimated through a photolysis cell mounted with two CaF_2 windows. The sample typically contained 10-30 mTorr of precursor molecules and 4 Torr of He bath gas under constant flow conditions. Pressure in the cell was monitored with a capacitance manometer (MKS Baratron, 0-10 Torr). Emission after the photolysis laser pulse was collected perpendicular to the laser propagation axis by a gold–mirror Welsh cell arrangement in the photolysis cell and then collimated and focused into the FTIR spectrometer by two KBr lenses that match the f/4 focusing characteristics of the spectrometer. The spectrometer (Bruker IFS 66/s) was equipped with an interferometer capable of time-resolved step–scan measurements and a mercury cadmium telluride detector (HgCdTe J15D14, *EG&G* Judson Technologies, 500 ns rise time, 750-10 000 cm^{-1} spectral range). The internal cavity of the FTIR was continually flushed with a FTIR purge gas generator (75-45, Parker Balston). The spectral response of the HgCdTe detector was calibrated with a Globar® source, which was modeled as a perfect blackbody.

Interferograms for this work were recorded at 100 ns time intervals averaging 200 laser shots per interferogram point for a total observation window of 20 μs. The time–resolved interferometric signal from the detector was amplified (ten times) by a fast amplifier (Stanford Research Systems SR445, DC-300 MHz) before reaching the transient digitizer (Spectrum PAD82a, 100/200 MHz), which was triggered by a fast photodiode that monitored the excimer output. Subsequent Fourier transformation of each interferogram yields a time–resolved spectrum at every 100 ns. To further enhance the observed spectral resolution, spectra were synchronously cross correlated in bins of 10 to yield representative spectra spanning 1.0 μs intervals [26]. The spectral resolution was typically set at 12 cm^{-1}.

Acrylonitrile ($\geq$99%) and acylonitrile–d3 (98% atom D) (both Sigma–Aldrich) were processed with several freeze pump thaw cycles before use and purity checked with IR absorption spectroscopy. Helium gas from the supplier (Spectra Gas, research grade, 99.9%) was used directly. Unphotolyzed sample was recollected after each experiment at liquid nitrogen temperature and purified for further use.

5.3 Results and Analysis

5.3.1 Time–resolved IR emission spectra following 193 nm photodissociation

Time–resolved IR emission spectra of the protonated sample at intervals of 2, 6, 11, and 16 μs following the arrival of the 193 nm photolysis pulse are presented in Fig. 1. Five main spectral features persist throughout all observed time slices. Table 5.1 summarizes the assignments of these IR emission features. With the exception of the feature just above the low-energy cutoff of the MCT detector around 720 cm^{-1}, all observed features exhibit an anharmonic bandcenter shift toward the fundamental transition frequencies with time. The features exhibiting marginally resolved P and R-branches with fundamentals at 2023 and 3652 cm^{-1} are assignable to the ν_3 CN

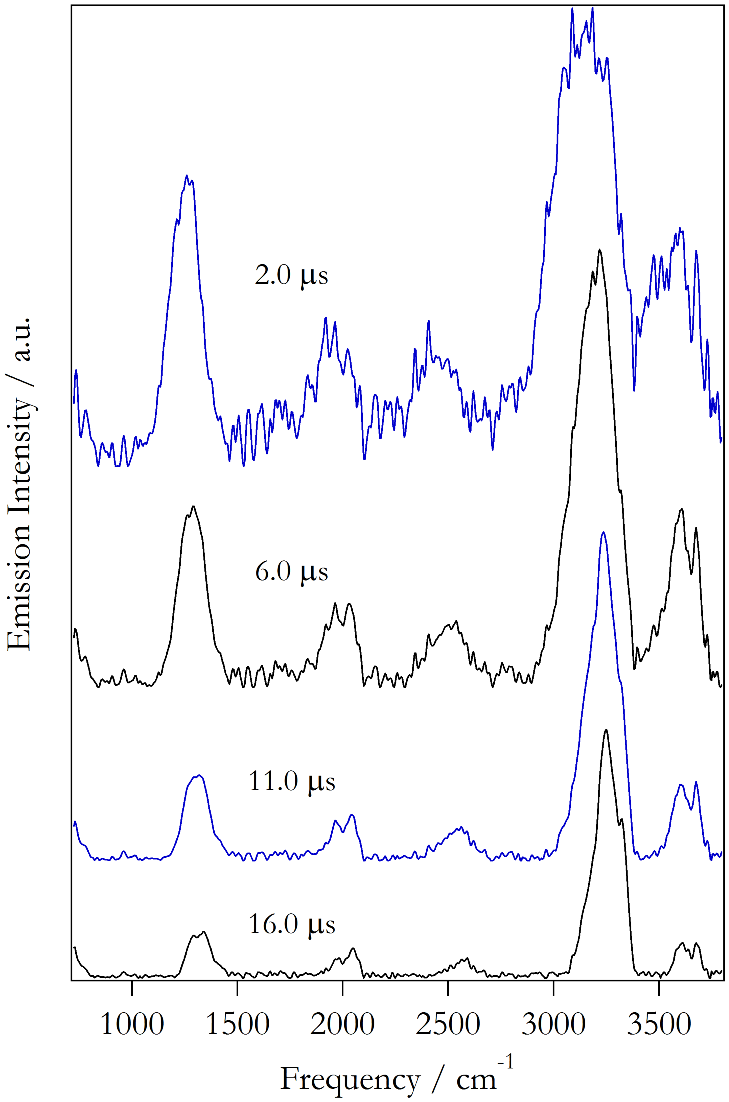

Figure 5.1
Time-resolved IR emission spectra collected following the 193 nm photodissociation of vinyl cyanide.

stretch and ν_1 NH stretch of HNC [27] respectively. While there is no indication of the ν_3 CN stretch of HCN at 2097 cm^{-1}, this does not imply the absence of HCN as a product. The CN stretch of HCN is a notoriously weak feature with a known transition dipole moment of only 0.001362 D [28], much smaller than the 0.108 D transition dipole moment of the CN stretch of HNC [29,30]. Any signal arising from the CN stretch of HCN would likely be buried in the noise of the spectra. In comparison, the CH stretch of HCN [28] has a detectable transition dipole moment of 0.0831 D.

Table 5.1
The spectral assignment (fundamental transition frequencies and molecular nature) for the observed features in the time–resolved IR emission spectra following the 193 nm photodissociation of vinyl cyanide. Also listed are the photodissociation channels leading to the production of the observed species.

Frequency(cm^{-1})	Species	Dissociation channel
712	HCN(ν_2)	[2]
720	HCCCN($\nu_6 + \nu_7$)	[4] and [5]
730	HCCH(ν_5)	[1] and [2]
1314	HCCCN($2\nu_5$)	[4] and [5]
1326	HCCH($\nu_4 + \nu_5$)	[1] and [2]
1410	HCN($2\nu_2$)	[2]
2023	HNC(ν_3)	[1]
2563	H_2CCCN(ν_3)	[7]
2596	HCN($\nu_1 - \nu_2$)	[2]
3289	HCCH(ν_3)	[1] and [2]
3311	HCN(ν_1)	[2]
3652	HNC(ν_1)	[1]

The intense feature in the emission spectra around 3300 cm^{-1}, exhibiting a sizable anharmonic shift and largely lacking any rotational resolution, is potentially assignable as the CH stretching modes of acetylene [31] at 3289 cm^{-1}, HCN [32] at 3311 cm^{-1}, and possibly cyanoacetylene [33] around 3326 cm^{-1}. As all three modes exhibit fundamental transitions within 40 cm^{-1} of one another, it is unlikely that the relative presence of either species can be discerned. Similarly, the second most intense feature around 1300 cm^{-1} is likely composed of overlapping contributions from the $(\nu_4 + \nu_5)$ combination band of acetylene [31] at 1326 cm^{-1}, the $2\nu_5$ overtone band of cyanoacetylene [33] at 1314 cm^{-1}, as well as possible minor contributions from the $2\nu_2$ overtone band of HCN [32] around 1410 cm^{-1}. Without clear resolution of each band, these features are unlikely to yield information regarding the relative amount of either fragment. It is important to note additionally that there is no clear evidence to support the presence of the ν_3 CN stretch of cyanoacetylene, which has a fundamental transition near 2274 cm^{-1} and transition dipole moment of 0.0418 D [33]. In that regard, as the ν_3 CN stretch is a less energetic motion of cyanoacetylene (within the assumption of a Boltzmann distribution for the excited molecules) compared to the ν_1 CH stretch, there should not be a substantial cyanoacetylene contribution in the 3300 cm^{-1} band. In the same way, the $2\nu_5$ overtone band of cyanoacetylene at 1314 cm^{-1} is a less energetic motion compared with both the ν_3 CN and the ν_1 CH stretches; hence we cannot rule out a low-energy cyanoacetylene contribution in the 1300 cm^{-1} band. Regardless, the sizable overlap of all the potential transitions from either acetylene, HCN, or cyanoacetylene in the 1300 cm^{-1} band precludes a definitive assignment using these spectra. Lastly, the feature with the latter time position near 2600 cm^{-1} has previously been assigned solely as the ν_3 CN stretch of the alpha cyanovinyl radical (H_2C=C–CN) [18]. However, if vibrationally excited HCN is produced in significant amounts, this feature would also contain contributions from the $(\nu_1 - \nu_2)$ difference band of HCN with a known fundamental near 2596 cm^{-1} and a modest transition dipole moment of 0.0226 D [28].

Figure 2 highlights the IR emission spectra at numerous time intervals following the 193 nm photodissociation of perdeuterovinyl cyanide. As in the protonated case, there is a series of five features that persist for most of the observed time slices.

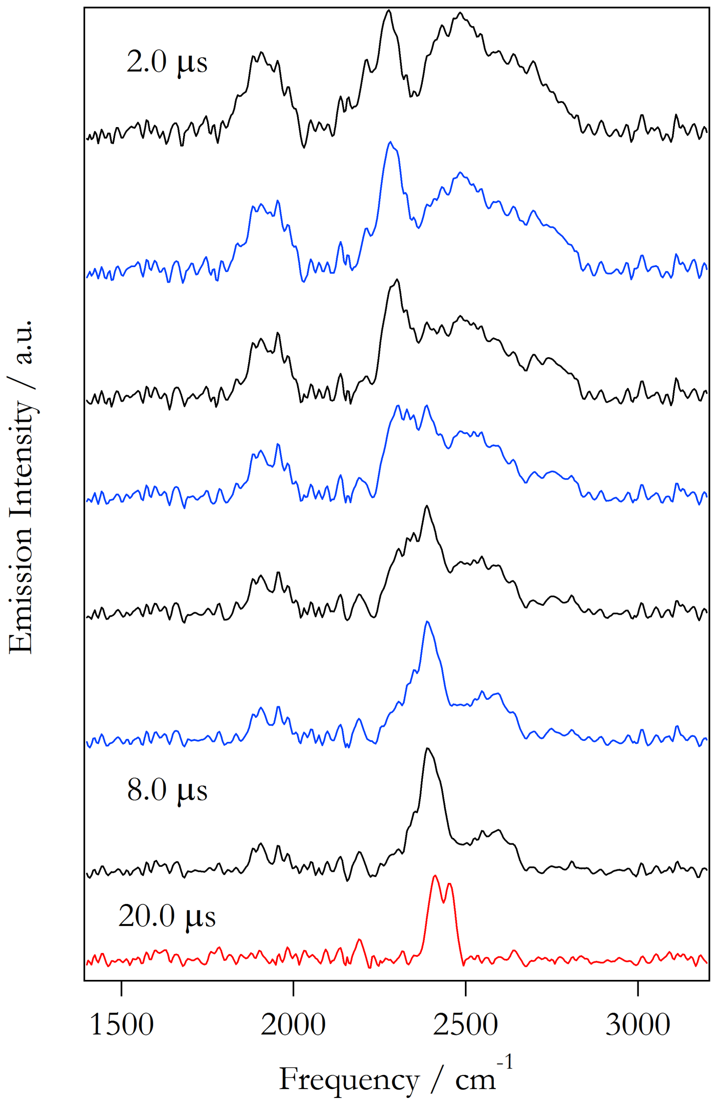

Figure 5.2
Time–resolved IR emission spectra collected following the 193 nm photodissociation of fully deuterated vinyl cyanide.

The feature attributable to the $(\nu_4 + \nu_5)$ combination band of acetylene [31,34] and the $2\nu_5$ overtone band of cyanoacetylene [35] is identified at 1050 cm^{-1} upon deuteration. Additionally, there is a band centered near 1950 cm^{-1}, assignable to the ν_3 CN stretching modes of DNC (1938 cm^{-1}) (Ref. 36) and DCN (1925 cm^{-1}) [37]. Unlike HCN, DCN has a modest transition dipole moment of 0.02274 D (Ref. 28) for the CN stretching mode. The transition dipole moment of DNC has not yet been measured, but *ab initio* calculations at the B3LYP/aug–cc–pVQZ (Ref. 38) level generates a transition dipole moment of 0.066 D for the ν_3 CN stretch mode. Subsequently, both isomers (DCN and DNC) could be contributing to the signal observed at 1950 cm^{-1}. The ν_3 CN stretch of deuterated cyanoacetylene is an IR active mode with a known fundamental frequency of 1966 cm^{-1} and a transition dipole moment of 0.0439 D [35]. This mode is notably absent in the undeuterated spectra; therefore there is no reason to expect that it is contributing significantly in the deuterated spectra.

The most interesting features of the perdeuterodissociation spectra (Fig. 2) are the group of partially resolved features spanning from 2200 to 2800 cm^{-1}. Unlike the protonated fragments, the CD stretching fundamentals of deuterated acetylene and DCN, as well as the ND stretch of DNC, are all well resolved by at least 150 cm^{-1}. As is particularly evident in the spectra at and after 4 μs, there are three partially resolved features with fundamentals at 2349, 2630, and 2787 cm^{-1} which are assignable to deuterated acetylene [31,34], DCN [37], and DNC [39], respectively. It is important to note that the feature at 2250 cm^{-1} in the early time spectra quickly undergoes an anharmonic shift into the ν_3 CD stretch of deuterated acetylene at 2439 cm^{-1}. This feature in the early time spectra should not be assigned as the ν_2 C≡C stretch of deuterated cyanoacetylene whose fundamental transition is at 2247 cm^{-1} [$|\mu|$=0.0469 D (Ref. 35)]. We note that a similar feature existed in the time-resolved IR emission spectra previously taken after the 193 nm photodissociation of perdeuterovinyl bromide [12]. Figure 3 highlights a comparison between the quickly shifting features observed in both vinyl cyanide–d3 and vinyl bromide–d3 dissociation–emission spectra. In our prior examination of the dissociation of vinyl bromide, it was determined that the dominant channel leading to molecular fragments was that of a three–center elimination of hydrogen bromide and vinylidene ($^1A_1$) [11].

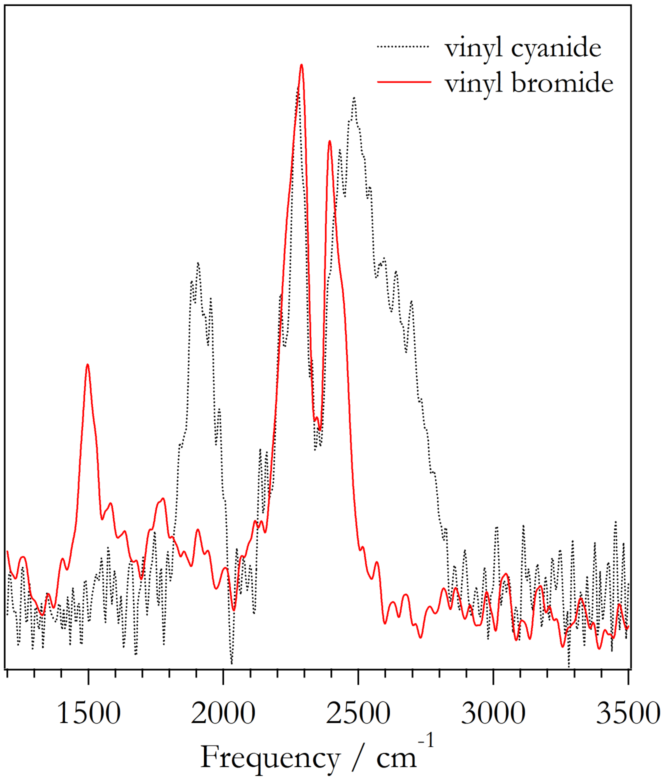

Figure 5.3
Comparison of early time emission spectra following the 193 nm photodissociation of deuterated vinyl cyanide (black, dotted) and deuterated vinyl bromide (red, solid).

It should be noted that calculations have found that vinylidene ($^1A_1$) has a shallow isomerization barrier (1.5 kcal $mole^{-1}$) and on the time scale of our observation would rapidly isomerize to acetylene with a minimum of 44.3 kcal $mole^{-1}$ of internal energy [40-43]. When considering deuterated vinylidene ($^1A_1$), which has an estimated (based on zero-point energy correction) isomerization barrier of 24 kcal $mole^{-1}$, we anticipate that deuterated acetylene would be initially produced with at least 45.4 kcal $mole^{-1}$ of internal excitation [41,43]. Subsequently, we assign the quickly shifting feature originally appearing at 2250 cm^{-1} to emission from the ν_3 CD stretch of highly rovibrationally excited deuterated acetylene.

Table 5.2
The spectral assignment (fundamental transition frequencies and molecular nature) for the observed features in the time-resolved IR emission spectra following the 193 nm photodissociation of vinyl cyanide–d3. Also listed are the photodissociation channels leading to the production of the observed species.

Frequency(cm^{-1})	Species	Dissociation channel
1314	DCCCN($2\nu_5$)	[4] and [5]
1326	DCCD($\nu_4 + \nu_5$)	[1] and [2]
1410	DCN(ν_3)	[2]
2023	DNC(ν_3)	[1]
3289	DCCD(ν_3)	[1] and [2]
3311	DCN(ν_1)	[2]
3652	DNC(ν_1)	[1]

The complete assignments of bands found in the IR emission spectra following 193 nm dissociation of perdeuterovinyl cyanide have been summarized in Table 5.2.

5.3.2 Photodissociation product population distributions

The anharmonic shift of a particular emission feature can be used to determine the internal energy content of the emitting molecules. Consequently, the temporal evolution of the frequency and intensity of emission features permits deduction in the change of the internal energy content of the emitting photofragments as a function of time [4448]. The procedure for deducing the internal energy content of the emitting molecules from the IR emission spectra is as follows: Using experimentally determined spectroscopic constants, we can calculate the energy of all vibrational levels of a particular molecule to high excitation energy. It is assumed that emission intensity from each of the high vibrational levels follows harmonic selection rules through all the IR active modes but the emission position is determined by the energy difference between the emitting level and the corresponding lower level. With a population distribution imposed on the vibrational levels, an emission spectrum can be calculated. Conversely, the population distribution can be determined from a fit of the experimentally observed spectra using the series of calculated spectra. This approach has been applied previously for the study of collisional energy transfer of highly vibrationally excited nitrogen dioxide [4448] sulfur dioxide [44], as well as pyrazine [44].

In previous studies where rotational resolution was not attainable, the emission spectra were calculated as purely vibrational transitions. The bandwidth and shape of the vibrational emission band were treated as a Gaussian function whose width matched that of the associated observed fundamental absorption feature [48]. In the current study, particularly for spectra recorded at later times, partial resolution of the rotational contour is observed. For these spectra, the emission band is calculated as the sum of individual rotational transitions where each transition is imposed with a Gaussian functional line shape, proportional to the experimental spectral resolution. The intensity of each rovibrational transition [49-51] in the emission spectra is given by

$$I^{em}_{\nu,J} = L_{\nu}\nu^{4}_{n,m}|\mu_{0\leftarrow 1}|^{2}S^{PQR}_{J,K}exp\left(\frac{-E_{in}[\nu_k(l_k),J]}{k_B T_{rot}}\right), \tag{5.9}$$

in which $\nu_{n,m}$ corresponds to the frequency of the $[m \leftarrow n]$ rovibrational transition, $|\mu_0 \leftarrow 1|$ the fundamental transition dipole moment, and L_ν is the vibrational line strength factor according to the harmonic scaling rule [44,52]. $S^{PQR}_{J,K}$ refers to the set of $(\Delta K = 0, \Delta J = 0, \pm 1)$ H$\ddot{o}$nl-London factors [49,53]. As will be discussed later, the vibrational population will be fitted through variation in a vibrational temperature to describe the distribution. However, the resolution of our experiments precludes the possibility of fitting the rotational distribution. A constant rotational temperature (T_{rot}) of 300 K has been used to model the rotational distribution. For latter time spectra, for example, after 10 μs, where rotational resolution is more relevant, each emitting molecule has experienced more than 100 collisions during the 10 μs period to allow rotational thermalization. For the earlier time spectra, even though the nascent reaction products may be generated with high rotational excitation, because these molecules usually also have a broad vibrational energy distribution, the effect of the rotational temperature in emission spectra is less discernable.

The detailed procedure for fitting the experimental spectra with the calculated emission basis set has been outlined previously in great detail [44,48]. Briefly, as the number of allowed transitions rapidly increases with internal energy, it is impractical to attempt a fit in which each individual transition is allowed to vary. To simplify the process, the rovibrational manifold is partitioned into evenly spaced 500 cm^{-1} wide bins. Invoking an assumption of equal population of all levels within a given bin, representative emission spectra can be generated by summing up all allowed transition within each energy bin. With the greatly reduced number of basis bin spectra, the experimental spectra can be fitted either through enforcing a functional form on the bin population distribution [48] or through a free-form fit [47]. For the free–form fit, the populations of the individual bins are allowed to vary freely until the difference between the calculated and experimental spectra is minimized using a nonlinear least-squares fitting procedure.

5.3.2.1 Modeling IR emission from DCCD ν_3

High resolution spectroscopic investigations of deuterated acetylene have yielded rovibrational constants for describing the ground state vibrational levels up to 17 000 cm^{-1} above the zero-point energy [31,34]. If the initial photofragment is in the form of deuterated vinylidene ($^1A_1$) [reaction (2)], isomerization to deuterated acetylene will add an additional 46 kcal $mole^{-1}$ (16 000 cm^{-1}) of internal excitation [41,43] on top of any energy originally partitioned to the nascent vinylidene ($^1A_1$) fragment. Alternatively, direct generation of acetylene [as in reaction (1)] leaves nearly 92 kcal $mole^{-1}$ to be partitioned among all the various translational and internal degrees of freedom of both photofragments. Therefore, it is reasonable to expect that if acetylene is generated both as vinylidene ($^1A_1$) in a three–centered reaction [reaction (2)] and directly from a four–center reaction [reaction (1)], it should show up in the collected emission spectra in two very distinct energetic distributions separated by as much as 46 kcal $mole^{-1}$.

For the deuterated acetylene spectra, our simulation analysis will focus solely on the ν_3 CD stretch. Only transitions allowed by the rigid-rotor/harmonic oscillator selection rules: $\Delta\nu_3 = -1, \Delta J = 0, \pm 1$ will be included in the calculation. To account

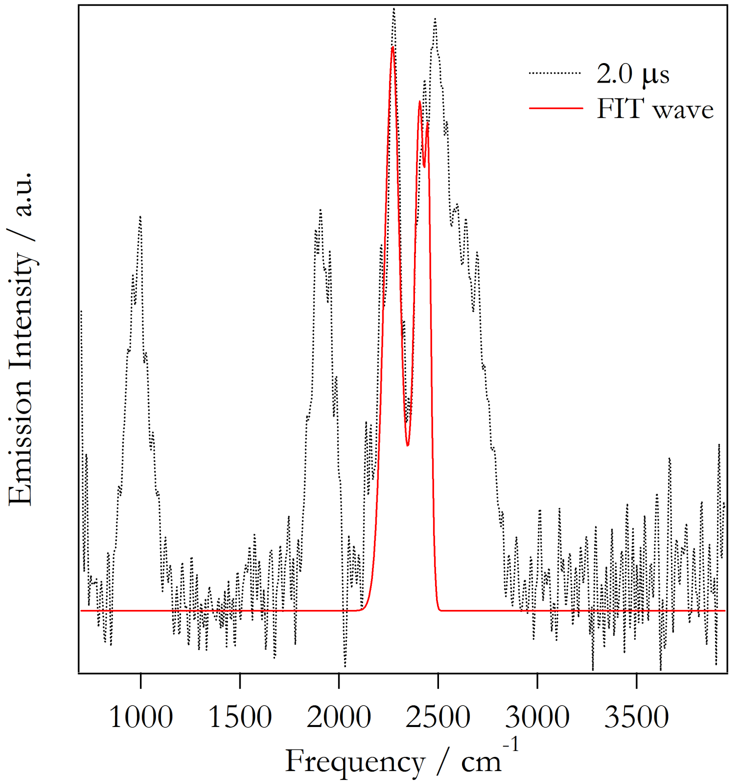

Figure 5.4

Experimental (black, dotted) spectrum collected 2 μs after the dissociation of deuterated vinyl cyanide overlaid with the calculated best fit spectrum (red, solid) of deuterated acetylene obtained using Eqs. (5.9) and (5.10).

for the possibility that acetylene may be generated with vastly different energy content from two different reactions, a dual population distribution [Eq. (10)] is used to fit the observed spectral feature: a low–energy distribution defined by a temperature (in the first term) as well as a high–energy Gaussian distribution,

$$P^j = \frac{\alpha_1}{\sqrt{2\pi}} exp\left(\frac{-hcE_j}{k_B T_{vib}}\right) + \frac{\alpha_2}{\sqrt{2\pi}\sigma} exp\left(\frac{-[E_j - < E >]^2}{2\sigma^2}\right). \tag{5.10}$$

In the spectral fitting, there are four variables: the relative intensity scaling factors (α_1/α_2), the low–energy vibrational temperature (T_{vib}), as well as the average internal energy <E> and width (σ) of the high-energy Gaussian distribution. Figure

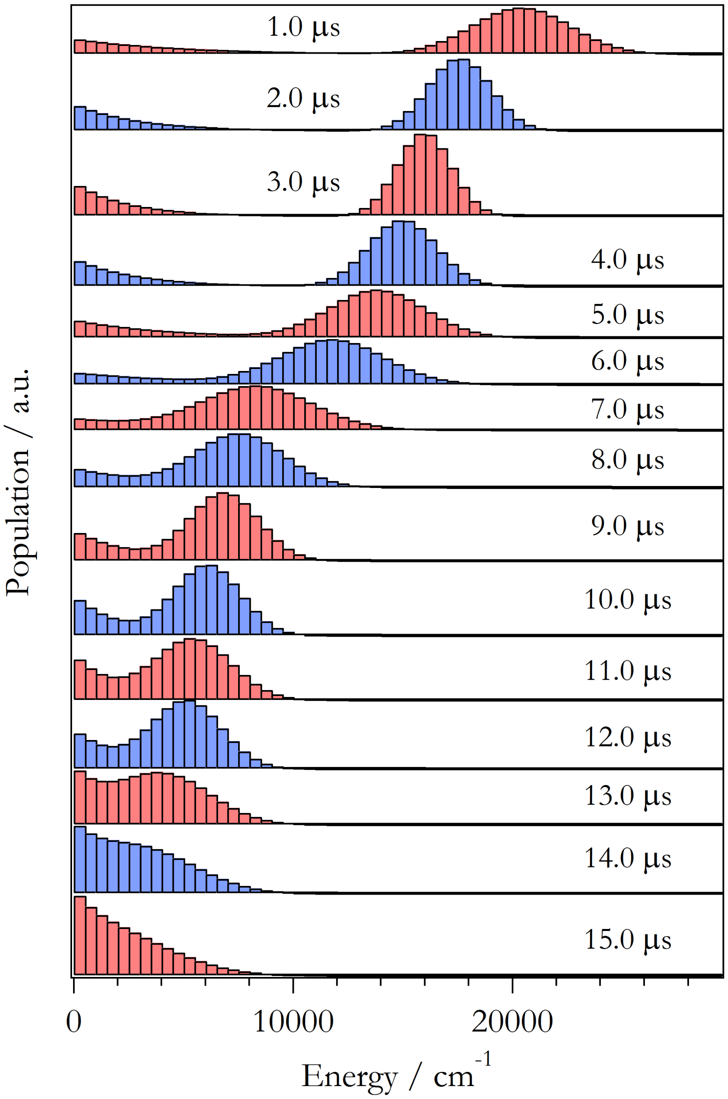

Figure 5.5
DCCD population distributions as a function of time following the 193 nm dissociation of deuterated vinyl cyanide.

4 highlights an experimental emission spectrum collected 2 μs after the arrival of the photolysis pulse with an overlay of the best fit calculated for deuterated acetylene emission. At this earlier time, as expected, the bimodal distribution is clear. The complete evolution of the deuterated acetylene populations as a function of time, deduced from the fitting of spectra taken at various times, is shown in Fig. 5. At early times when there are two distinct energy distributions, the change in time of the average internal energy of the high-energy distribution can be well described by

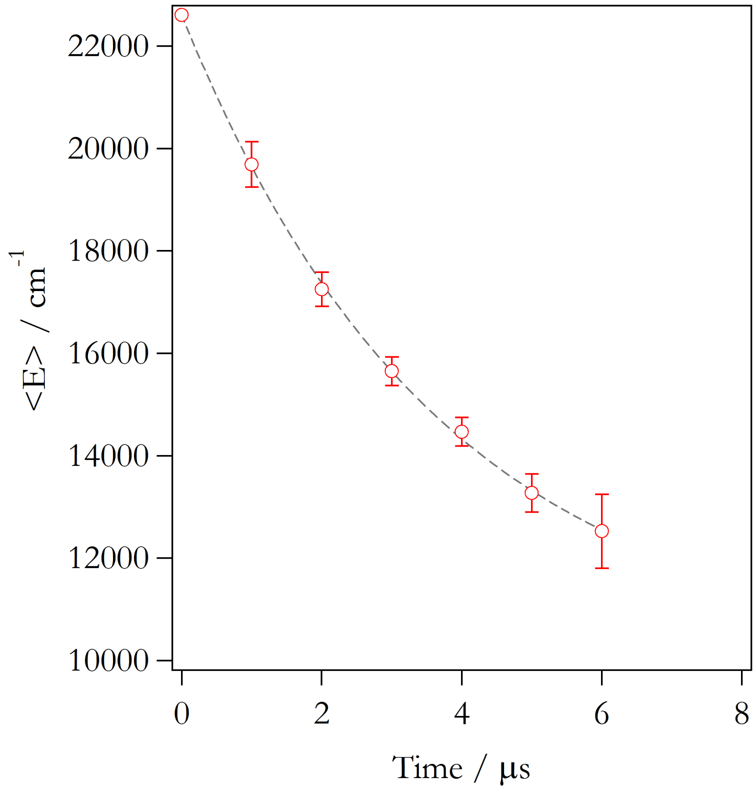

Figure 5.6
Measured variation of the average energy of the highly rovibrationally excited DCCD (collisionally quenched with 4 Torr He) as a function of time along with an overlaid exponential fit function. The zero–time point has been estimated through back extrapolation of the exponential fit.

a decaying exponential function. As displayed in Fig. 6, extrapolation of this functional form back to zero time yields an average initial internal energy for deuterated acetylene of 22 400±700 cm^{-1} (64.2±2.0 kcal $mole^{-1}$).
Since the zero-point energy difference between deuterated acetylene and vinylidene ($^1A_1$) is predicted to be 15 880 cm^-1, or 45.5 kcal $mole^{-1}$ [41,43], it is suggested that vinylidene ($^1A_1$) is initially generated from reaction (2) with 7600±700 cm^{-1} (22±2.0 kcal $mole^{-1}$ of internal energy.

For the low-energy acetylene distribution, a vibrational temperature is determined from the fitting of each time–resolved spectrum. The series of vibrational temperatures was found to be well described by a decaying exponential functional form. Extrapolation of this functional form back to zero time suggests an initial vibrational temperature of 18 425 K, or an average energy of 29.0±1.4 kcal $mole^{-1}$. This temperature corresponds to the nascent acetylene–d2 internal energy distribution following the four–center elimination [reaction (1)].

5.3.2.2 Modeling IR emission from HNC ν_1 and ν_3

The appearance of the ν_1 NH stretch and ν_3 CN stretch transitions, unobstructed by other bands, from HNC in the emission spectra provides an opportunity to examine the internal energy content of the products from the four–center HNC + acetylene elimination channel of vinyl cyanide. Prior spectroscopic studies by Maki and Mellau [27] have determined the vibrational constants from vibrational levels of HNC up to 6100 cm^{-1} above the zero–point level. These constants are used in this study to calculate the vibrational level positions up to 12 000 cm^{-1} above the zero-point level. IR emission transitions from these levels are then calculated using the rigid–rotor/harmonic oscillator selection rules ($\Delta\nu_1$ and $\Delta\nu_3$ =-1, $\Delta J = 0, \pm1$) to fit the observed ν_1 NH stretch and ν_1 CN stretch bands for the determination of the vibrational energy distribution.

Unlike the deuterated acetylene case, there appears to be only a single population distribution of HNC determined from the spectral fitting. The fitted population appears to be readily describable by a distribution function as in the first term of Eq. (5.10) with a vibrational temperature.

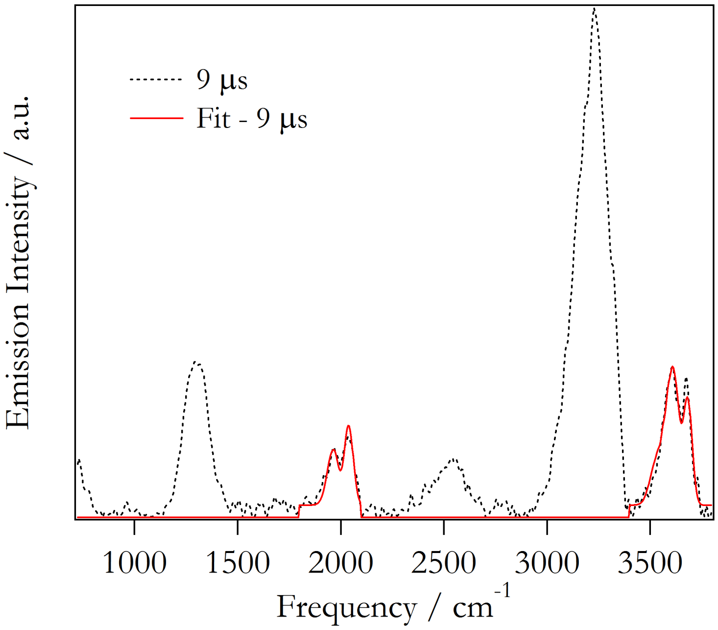

Figure 5.7
Experimental (black, dotted) spectrum collected 9 μs after the dissociation of vinyl cyanide overlaid with the calculated best fit spectrum (red, solid) of hydrogen isocyanide obtained using Eqs. (5.9) and (5.10).

Figure 7 highlights the representative fit of the HNC features in late time emission spectra. The evolution of the measured vibrational temperature, as presented in Fig. 8, is observed to obey an exponential functional form, which permits extrapolation back to a zero-time vibrational temperature of 15 192 K. The nascent average internal energy of HNC is estimated from this zero-time vibrational temperature to be 24.5±1.4 kcal $mole^{-1}$ for HNC originating from reaction (1).

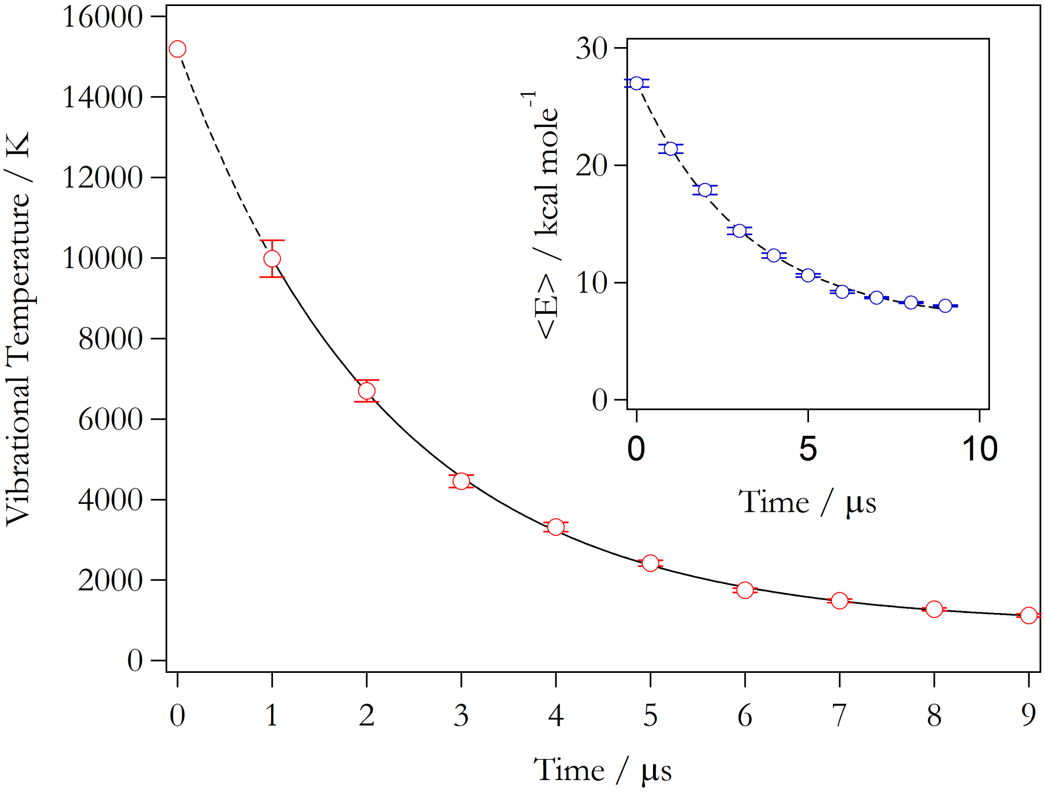

Figure 5.8
Measured variation of the vibrational temperature of rovibrationally excited HNC (collisionally quenched with 4 Torr He) as a function of time along with an overlaid double exponential fit function. The zero–time point has been estimated through back extrapolation. The inset shows the corresponding average internal energy content of the HNC ensemble as a function of time.

5.4 DISCUSSION

5.4.1 The electronic state of vinylidene from the photodissociation reaction

Following the photodissociation of vinyl cyanide–1d near 190 nm, Fahr and Laufer [16] observed UV absorption transitions associated with both DCN and vinylidene ($^3B_2$). As there were no observable transitions assignable to HCN (the expected four–center elimination photoproduct), it was suggested that the dissociation occurred predominantly through a three–center elimination channel yielding DCN + vinylidene ($^3B_2$). Nevertheless, in the follow up PTS study by Blank et al. [13], while it was suggested that the three–center channel dominated the H(CN) + C_2H_2 elimination, conservation of energy arguments based on the measured translational energy results effectively ruled out the occurrence of vinylidene ($^3B_2$). New results from the emission spectra can be used to help resolve this contradiction.

Dissociation via reaction (3) leaves only 14 kcal $mole^{-1}$ to be partitioned among the various degrees of freedom of both the HCN and vinylidene ($^3B_2$) fragments [13]. With the possible exception of the low–energy bending motions, vibrational populations of the nascent HCN and vinylidene ($^3B_2$) would likely be limited to the zero-point level and hence unobservable in the IR emission spectra. Vinylidene in the ($^3B_2$) state is relatively stable due to a massive isomerization barrier of 50 kcal $mole^{-1}$ relative to the associated acetylene ($^3B_2$) species [40]. This is quite different from the relatively unstable vinylidene ($^1A_1$), which would quickly isomerize to acetylene ($^1\Sigma_g^+$) through a shallow barrier of only a few kcal $mole^{-1}$. Triplet vinylidene produced from direct photodissociation is not expected to give IR emission but is instead expected, through collision induced intersystem crossing with the inert gas, to become first singlet vinylidene and then singlet acetylene. The singlet ($^1A_1$)–triplet ($^3B_2$) splitting of vinylidene is predicted to be on the order of 2 eV, or 45 kcal $mole^{-1}$ [40]. Hence, any singlet acetylene generated from crossing of triplet vinylidene should have at least 92 kcal $mole^{-1}$ of nascent internal energy. In the present study, it has been determined that acetylene is generated in two distinct energetic distributions. The highest excited acetylene distribution has an estimated average nascent vibrational energy of only 64 kcal $mole^{-1}$, well below the 92 kcal $mole^{-1}$ possible if it were from triplet vinylidene in reaction (3). Therefore, it is suggested that the highly excited acetylene distribution containing 64±2.0 kcal $mole^{-1}$ of nascent internal energy originated not from triplet vinylidene ($^3B_2$) but rather as singlet vinylidene ($^1A_1$) with 22±2.0 kcal $mole^{-1}$ of nascent internal energy. Furthermore, conservation of energy suggests that HCN is generated with approximately 25 kcal $mole^{-1}$ of nascent internal energy, nearly double the 14 kcal $mole^{-1}$ of total energy available following dissociation to HCN + vinylidene ($^3B_2$). Therefore, in agreement with the results of Blank et al., the observed HCN and acetylene IR emission features suggest that reaction (2) [as well as reaction (1)] is occurring to a much more significant extent than reaction (3).

5.4.2 HNC versus HCN as photodissociation product

The PTS study of Blank et al., using a tunable ionization source, has provided valuable data on the nascent internal energy of the m/e 27 (HCN and/or HNC) photofragment [13]. The observed ionization onset of 11.0±0.3 eV when assigned to HCN (with an ionization potential of 13.6 eV) would suggest a high internal energy of 2.6±0.3 eV, or 60 kcal $mole^{-1}$, in nascent HCN. On the other hand, since our study has clearly provided evidence supporting the existence of HNC as a reaction product, the PTS results should be re–examined. If the m/e 27 signal in the PTS study were to be assigned to HNC [which has a measured ionization potential of 12.04 eV (Ref. 54)], a more reasonable internal energy content of 1.0±0.3 eV (24±7 kcal $mole^{-1}$) should then be observed. This number is in excellent agreement with our measured value of 24.5±1.4 kcal $mole^{-1}$. Both isomers (HCN and HNC) may appear as photodissociation products and contribute to the m/e 27 signal in the PTS study. The presence of excited HNC with a lower ionization threshold, however, prevented an unobstructed measurement of the HCN internal energy content.

The relative population and internal energy content of HCN/HNC can be deduced by examining the population and energy content of the corresponding co-product acetylene in the photodissociation reaction. Specifically, as noted in the *ab initio* study of Derecskei-Kovacs and North [17], the generation of HCN should be accompanied by vinylidene ($^1A_1$) [reaction (2)], or rather, highly rovibrationally excited acetylene, whereas the generation of HNC should be accompanied by minimally excited acetylene [reaction (1)]. Figure 9 exhibits the ratios of the high-energy acetylene population [from reaction (2)] to the total acetylene population [from both reactions (1) and (2)] determined from the emission spectra detected at different times following the photodissociation of deuterated vinyl cyanide. The earliest ratios, obtained from fits to two nearly completely resolved acetylene features in the emission spectra, show minor fluctuations around a value of 0.77. As time progresses, the fit attributes more population to the low–energy vibrational temperature, likely due to collisional relaxation, and hence results in a rapid decrease in the ratio. The earliest observed ratios are found to be relatively constant around a value of 0.77, which is thus adopted as the representative nascent population ratio for acetylene originating from reaction (2) relative to the total acetylene population [originating from reactions (1) and (2)].

Consequently, the ratio of the D(CN) + C_2D_2 photodissociation products in two isomeric forms is deduced as [DCN] : [DNC] = (3.34 : 1.00).

With the ratio of the DCN/DNC populations determined, we can now reconsider the significance of the center of mass (c.m.) translational energy distribution

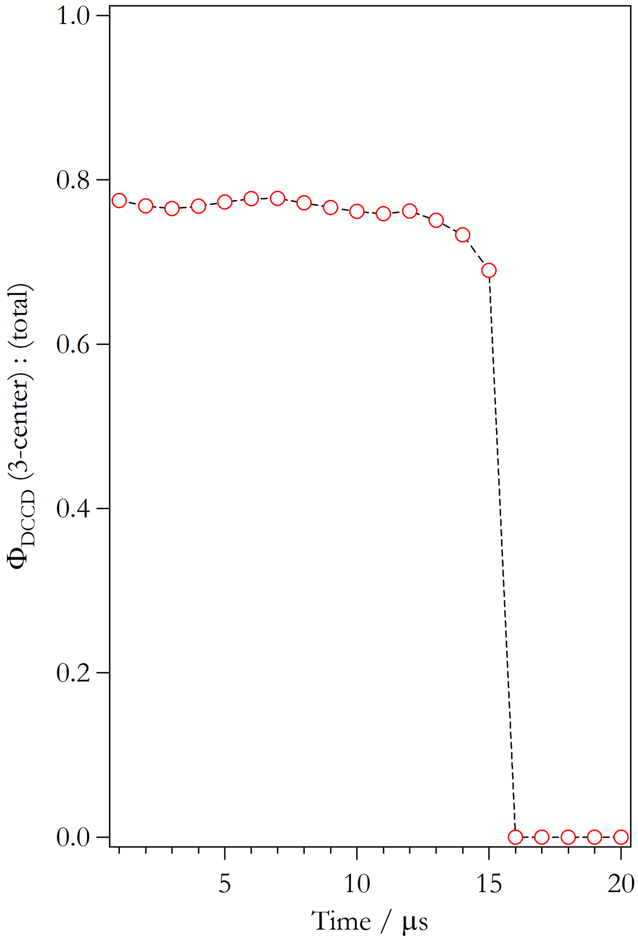

Figure 5.9

Measured branching ratio of highly rovibrationally excited DCCD (three–center elimination) relative to the total DCCD population. The initial four points represent results obtained from fitting two partially resolved DCCD features, highly excited DCCD as well minimally excited DCCD. Points 6-15 correspond to an unresolved mixture of the two features, and the final five points were obtained by assuming a single representative vibrational temperature.

[P(E_T)], measured for the m/e (26+27) signals in the PTS study [13]. Specifically, the PTS study found that the distribution possessed an average energy of 15 kcal $mole^{-1}$ with a maximum near 8 kcal $mole^{-1}$. Moreover, it was observed that the distribution extended out beyond 47 kcal $mole^{-1}$. Assuming the isotope effect on the relative rates of the reactions is negligible, the HCN:HNC population ratio should be 3.34. The observed P(E_T) should therefore be dominated largely by the three–center HCN + vinylidene ($^1A_1$) loss channel and have a lesser contribution from the four–center HNC + acetylene channel. The three–center channel [reaction (2)] leaves about 62 kcal $mole^{-1}$ as available energy for HCN + vinylidene ($^1A_1$). As discussed above, we have measured the nascent average internal energy of the vinylidene ($^1A_1$) fragment to be 21.8 kcal $mole^{-1}$. As reaction (2) is found to contribute 77% of the detected fragments, it is reasonable to attribute the observed average (c.m.) translational energy of 15 kcal $mole^{-1}$ to the HCN + vinylidene ($^1A_1$) channel. Therefore, by conservation of available energy the nascent internal energy of HCN can be calculated to be 25.2 kcal $mole^{-1}$. In the same way, the four–center channel [reaction (1)] leaves about 92 kcal $mole^{-1}$ of available energy for HNC + acetylene. As we have measured the nascent internal energy of both of these fragments to be 29.0±1.4 kcal $mole^{-1}$ (HCCH) and 24.5±1.4 kcal $mole^{-1}$ (HNC), conservation of available energy suggests that the average (c.m.) translational energy for the four–center elimination [reaction (1)] must therefore be about 38.5±2.8 kcal $mole^{-1}$. It is of interest to note that the well separated average (c.m.) translational energies of the three– and four–center elimination products, coupled with the dominance of the three–center elimination channel, provide close semi–quantitative agreement to the overall observed (c.m.) translational energy distribution of the PTS study.

The negligible effect of the isotope substitution on the determination of the branching ratio can be assessed as follows. The harmonic frequencies of the fully protonated/ deuterated forms of the precursor and transition state structures associated with the H(CN) elimination channels were calculated at the UB3LYP/aug–cc–pVTZ level of theory. The frequencies, along with the modified transition state energies, adjusted to account for the isotope effect on vibrational frequencies, were used in a RRKM analysis. As expected, complete deuteration leads to an increase in the individual reaction rates due to the enhanced density of states. Nevertheless, the relative ratio of the two channels, both in the protonated and deuterated forms, remained nearly invariant with a calculated H(D)CN : H(D)NC branching ratio of 3.3±0.1.

5.4.3 The $HC_2(CN)$ + H_2 channel

In Derecskei–Kovacs and Norths calculation, the three–center H_2 + cyanovinylidene ($^1A'$) elimination channel [reaction (5)] was calculated to be the fastest (with a dissociation rate of 1.63×10^{10} Hz) and the largest branching ratio of 0.593. Similar to vinylidene ($^1A_1$), cyanovinylidene ($^1A'$) is calculated to be a metastable minimum on the ground potential energy surface of cyanoacetylene [55,56]. Hu and Schaefer [55] examined cyanovinylidene ($^1A'$) at the TZ2P CCSD(T) level of theory and found a zero-point energy corrected isomerization barrier of only 2.2 kcal $mole^{-1}$ and an exothermicity (relative to the cyanoacetylene ZPE) of 47.2 kcal $mole^{-1}$. Furthermore, their calculations predict a singlet ($^1A'$)–triplet ($^3A'$) splitting on the order of 42 kcal $mole^{-1}$, implying a similarly large exothermicity following intersystem crossing to singlet cyanovinylidene ($^1A'$).

The rovibrationally hot cyanoacetylene resulting from the photodissociation product cyanovinylidene ($^1A'$) should be detectable by TR–FTIRES. This is expected as cyanoacetylene is an experimentally well characterized molecular species whose transition dipole moments are comparable to acetylene and hydrogen isocyanide [28-30,57]. Should the dominant channel be, in fact, the three-center elimination of cyanovinylidene ($^1A'$) [reaction (5) or (6)], the resulting TR–FTIRES spectra are expected to display the various infrared active cyanoacetylene features. In both the protonated and deuterated studies, however, the experimental spectra show little evidence supporting even the slightest presence of cyanoacetylene. This observation suggests that any cyanoacetylene generated must be either relatively cold or produced in minor quantities relative to those observed for the acetylene, hydrogen cyanide, and hydrogen isocyanide products. Prior studies, most notably the PTS study of Blank et al. [13], have clearly shown the presence of cyanoacetylene as a photofragment. In particular, the photoionization spectrum of the resulting cyanoacetylene fragment suggested a maximal nascent internal energy content of 0.8±0.3 eV (18.4±7 kcal $mole^{-1}$) [13]. As this value is much less than the expected 47.2 kcal $mole^{-1}$ resulting from the three–center elimination of cyanovinylidene ($^1A'$), it is likely that reaction (4) generating cyanoacetylene directly, not (5) or (6) generating cyanovinylidene ($^1A'$), is the dominant H_2 loss channel. It is therefore concluded that, dissimilar from the observation that the three–center transition state dominates the acetylene elimination channel, the four–center transition state likely dominates the cyanoacetylene elimination channel.

5.4.4 The H(CN) + C_2H_2 channels

Derecskei–Kovacs and North [17] previously carried out *ab initio* calculations to determine the potential energy surface and the associated transition states for the 193 nm photodissociation channels of vinyl cyanide. Subsequently, they examined the microcanonical RRKM dissociation rate constants for the various elimination channels. The calculated dissociation rates allowed the estimation of the branching ratios of the various elimination channels. In their calculation, it was determined that the four–center elimination channel [reaction (1)] leading to HNC + acetylene possessed a transition state energy nearly 10 kcal $mole^{-1}$ above the corresponding three–center transition state of reaction (2) leading to HCN + vinylidene ($^1A_1$). The corresponding RRKM dissociation rates resulted in a branching ratio of the three– versus four–center [reaction (2) : reaction (1)] channels on the order of 126, which is in stark contrast to our measured value of 3.34. The new experimental value requires a re–examination of the relative magnitudes of the *ab initio* calculated transition state energies.

The calculated rate constants were derived, as in the RRKM theory, from a ratio of the number of states (at the excitation energy) of the particular transition state [$N_{TS}(E', J')$] to the density of states (again, at the excitation energy) of the precursor species [$\rho(E', J')$]. As the precursor species is identical for all reaction channels, the relative branching ratio is directly proportional to the ratio of the number of states of the associated transition states. The RRKM branching ratio can be changed, therefore, by simply adjusting the relative energy difference between the two transition states without the knowledge of the absolute energy of either state.

We have used the harmonic vibrational frequencies of the precursor as well as the two calculated transition states from *ab initio* calculations to perform RRKM analysis of the photodissociation rates. In order to achieve an HCN to HNC product ratio of 3.34, we have found that the energy of the four–center transition state should be 10.5 kcal $mole^{-1}$ *below* that of the calculated three–center transition state. It is important to note that this estimate is within the framework of RRKM theory for calculating the dissociation rates with the assumption that the transition states for each of the channels are the same ones from the *ab initio* calculations [17].

Given that many factors may influence the determination of the reaction barriers from the reaction branching ratio, the contradiction between the experimentally measured branching ratio and the existing theoretical calculation calls for re–examination of theoretical calculations of the transition states.

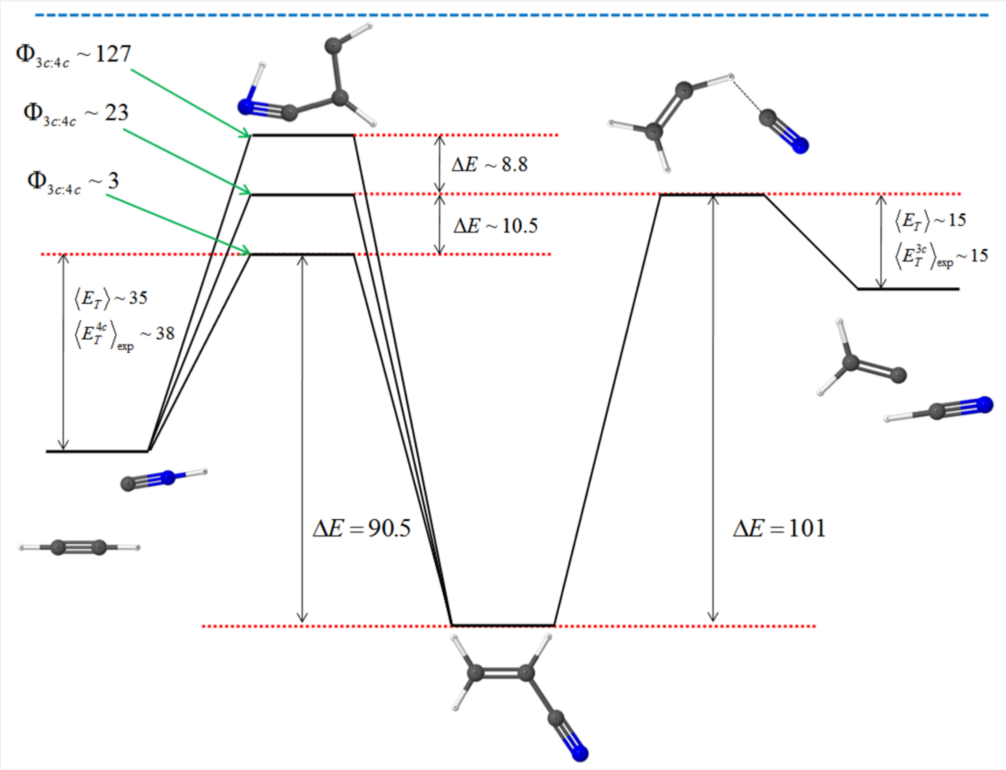

Figure 5.10

Determination of the transition state energies for the three- vs. four-center elimination of the H(CN) + C_2H_2 *channels. Values for the reverse recombination energies were estimated from the average translation energy values of Ref(13). RRKM analysis was repeated by iterating through decreasing values of the four-centered transition state energy until the calculated branching ratio matched the experimentally measured value.*

In an attempt to characterize the absolute energies of the two transition state structures for the H(CN) dissociation reactions, we turn our attention to the magnitude of the associated reverse recombination barriers. For a dissociation process over a barrier, it has been proposed that the resulting product translational energy will be directly proportional to the magnitude of the associated reverse recombination barrier [13,58,59]. The measured average translational energy for the HCN + vinylidene ($^1A_1$) channel of 15 kcal $mole^{-1}$ from the PTS study [13] agrees well with the *ab initio* calculated reverse recombination barrier for the three–center elimination channel (E_{TS}^{rev}=15 kcal $mole^{-1}$), and hence lends further support for the calculated energy of the three–center transition state of (E_{TS}^{3C}=101 kcal $mole^{-1}$). As depicted in figure 10, adopting a modified four–center transition state energy of 90.5 kcal $mole^{-1}$ (10.5 kcal $mole^{-1}$ below the three–center transition state) suggests a calculated translational energy of 35 kcal $mole^{-1}$ for the HNC + acetylene channel, which is in close agreement with our experimental value of 38.5±2.8 kcal $mole^{-1}$. Subsequently we deduce that the transition state energies most consistent with the measured branching ratio and the product translational energy would be (E_{TS}^{3C}=101 kcal $mole^{-1}$) for the three–center transition state, and (E_{TS}^{4C}=90.5 kcal $mole^{-1}$) for the four–center transition state.

In addition to the standard molecular and radical elimination channels already discussed above, some recent literature suggested that a third channel, deemed the roaming atom effect [60-63], may account for the observed data. The roaming atom effect can be described roughly as a two–part process consisting initially of a partial radical dissociation followed by an intramolecular radical–radical reaction yielding a set of molecular products. The best characterized example of this phenomenon stems from the dissociation of formaldehyde (H_2CO) [64], in which the process commences with the elongation of one of the C–H bonds just short of a complete radical dissociation [63]. The weakly bound hydrogen samples the locally flat potential energy surface (roams) then subsequently returns to the pseudo–HCO radical and abstracts the remaining hydrogen yielding vibrationally hot molecular hydrogen (H_2) and rotationally cold carbon monoxide (CO) [60,61,63,64]. Alternatively, there also exits a molecular elimination channel (involving a well–defined transition state) which yields vibrationally cold H_2 and rotationally hot CO [60,61,63,64]. This highlights one of the telltale signatures of a roaming atom event coupled with a molecular elimination channel, a bimodal energetic distribution.

For the current study, there exist four energetically accessible radical (and hence potential roaming) channels, a single CN loss channel [reaction (8)] and three (two beta and a single alpha) H loss channels [reaction (7)] [17]. Depending on the identities of the roaming and abstracted atom(s)/ group(s) involved in the dissociation, there would be a variety of different molecular products not to mention unique internal energy distributions available. While the roaming atom effect remains a qualitatively viable possibility to account for the observation that acetylene is generated with a bimodal distribution of internal energies, its relevance to this reaction system remains unclear. As the above discussion show, the bimodal energy distribution can be quantitatively understood from the known, different reaction channels that each eventually give acetylene as product but with different energy. The necessity to invoke the roaming atom effect depends on further theoretical analysis and/or measurements of the product rotational energy distribution as a signature of this effect.

5.4.5 Nascent product energy distributions

Using the population distributions obtained from fittings of the emission spectral features from deuterated acetylene and hydrogen isocyanide, as well as conservation of energy arguments for the remaining photofragments, we have obtained average

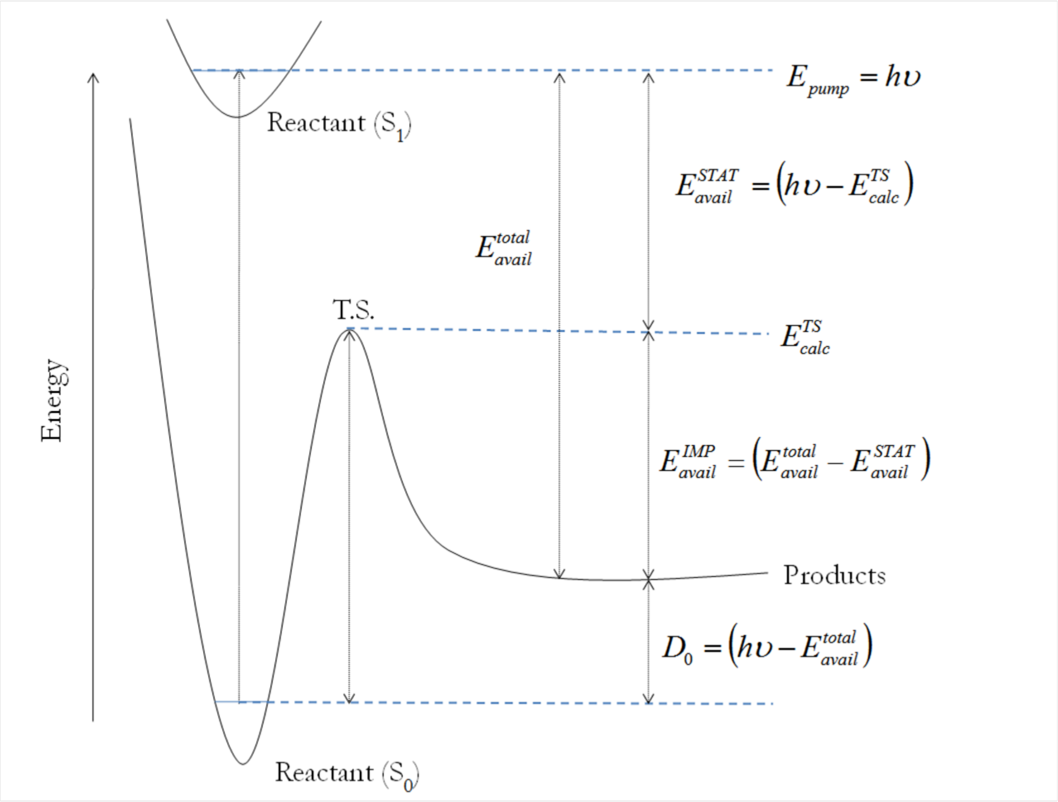

Figure 5.11

General schematic detailing the resulting partitioning of the remaining available energy for a photodissociation process (over a potential barrier) as described by a combined information-theoretic (statistical) + sudden impulsive method.

values for the nascent internal energy content of the photofragments resulting from reactions (1) and (2). In an attempt to further quantify the observed elimination channels, we now employ a combination of an information–theoretical statistical prior method [65] and the sudden–impulsive method [66,67] for analyzing the product energy content. Following the example of Mordaunt et al. [68], we have examined the use of a combined statistical and impulsive model in which the total available energy is partitioned into two separate energy reservoirs, one purely statistical and the other impulsive, i.e., $E_{avail}^{total} = E_{avail}^{stat} + E_{avail}^{imp}$. The two energetic partitions are determined (as in figure 11) in relation to the calculated zero–point energy of the associated transition states, E_{calc}^{TS} , and the thermodynamically determined total available energy, E_{avail}^{total} , where

$$E_{avail}^{stat} = (h\nu - E_{calc}^{TS}), \tag{5.11}$$

$$E_{avail}^{imp} = (E_{avail}^{total} - E_{avail}^{stat}). \tag{5.12}$$

Subsequently the corresponding methods are independently applied to determine the energy partition of each of the associated available energies among the products.

Muckerman [65] previously outlined a procedure, using the continuous rigid–rotor harmonic oscillator approximation, for obtaining analytical expressions for the information–theoretical prior probability density functions for photofragments following UV dissociation. Briefly, for a given polyatomic species undergoing unimolecular dissociation, the associated prior probability density functions for the resulting fragments can be derived through consideration of the total number of fundamental vibrational modes in each fragment as well as the structure of the resulting fragments (linear or nonlinear). For the three–center elimination channel yielding HCN + vinylidene ($^1A_1$) [reaction (1)], the expected nascent energies of the associated fragments can be predicted by modeling a general dissociation yielding a linear triatomic (s=4) and a general nonlinear (s=6) species. Employing the method of Muckerman [65], the prior probability density functions describing the vibrational degrees of freedom for both fragments can be derived as

$$\rho(E_V^{HCN}) = \frac{13!\Gamma(2)}{\Gamma(10)\Gamma(4)} \left[1 - E_V^{HCN}\right]^9 \left(E_V^{HCN}\right)^3 , \tag{5.13}$$

$$\rho(E_V^{H_2CC:}) = \frac{13!\Gamma(2)}{\Gamma(8)\Gamma(6)} \left[1 - E_V^{H_2CC:}\right]^7 \left(E_V^{H_2CC:}\right)^5 . \tag{5.14}$$

Similarly, the four–center elimination channel yielding HNC and acetylene [reaction (2)] can be modeled as a general dissociation yielding a linear triatomic (s=4) and a linear polyatomic (s=7) species. Once again, the prior probability density functions describing the vibrational degrees of freedom for both fragments are as follows:

$$\rho(E_V^{HNC}) = \frac{\Gamma(29/2)\Gamma(2)}{\Gamma(21/2)\Gamma(4)} \left[1 - E_V^{HNC}\right]^{19/2} \left(E_V^{HNC}\right)^3 , \tag{5.15}$$

$$\rho(E_V^{HCCH}) = \frac{\Gamma(29/2)\Gamma(2)}{\Gamma(15/2)\Gamma(7)} \left[1 - E_V^{HCCH}\right]^{13/2} \left(E_V^{HCCH}\right)^6 . \tag{5.16}$$

Integration over the various forms of the resulting prior probability density functions yields the associated nascent average energy values.

Using the generalized method described by Trentelman et al. [66,67], we explore the associated energy distributions as obtained following a dissociation described by an impulsive transfer of momentum. Briefly, the geometry of the associated transition states, particularly the identity and mass of the atoms involved in the dissociation, is used to relate the available energy to the translational degrees of freedom of the resulting photofragments through conservation of linear momentum. The resulting translational energy values can hence be used, through conservation of energy, to obtain the associated internal energy content of the various photofragments.

Table 5.3
Experimental and calculated (statistical and impulsive analysis) energy distributions for the nascent products from the HCN + vinylidene ($^1A_1$) and HNC + acetylene reactions following 193 nm photodissociation of vinyl cyanide.

<E>	Fragment(reaction)	Experiment	Calculation	Rev. Barrier
E_{int}	HCN [2]	25.2^a	26.8	
	$:C{=}CH_2$ [2]	21.8^a	20.8	
	HNC [1]	24.5^a	25.3	
	HCCH [1]	29.0^a	36.8	
E_{trans}	HCN [2]	15.0^b	14.5	(15)
	$:C{=}CH_2$ [2]	15.0^b	14.5	(15)
	HNC [1]	38.5^a	29.4	(35)
	HCCH [1]	38.5^a	29.4	(35)

(a) TR-FTIRES from this work.
(b) PTS from (Ref. 13).

Additionally, the associated reverse reaction recombination barriers for both the three– and four–center eliminations have been included for comparison against the average translational energies. All energies are in units of kcal mole^{-1}.

Consistent with the prior results of Derecskei–Kovacs and North [17], we employ the relative transition state geometries obtained at the UB3LYP/aug–cc–pVTZ level of theory in which reaction (2) is found to occur following the breaking of a C=C bond and reaction (1) occurs via the breaking of a C-H bond.

As recorded in Table 5.3, the combined application of both the statistical–prior and sudden–impulsive models results in product energies that are in reasonable agreement with all of the experimentally measured values. This general agreement of calculated product energy distribution with the experimentally measured values lends strong support for the reasonableness of the proposed mechanisms.

5.5 Conclusion

The time–resolved emission spectra collected following the 193 nm photodissociation of both vinyl cyanide and deuterated vinyl cyanide have revealed the nature and energy content of vibrationally excited photodissociation products. The relative quantity and the energy distribution of the nascent products as well as the branching ratios of the molecular elimination channels can be deduced. The following conclusions on 193 nm photodissociation of vinyl cyanide can be drawn.

1. Contrary to the results of an early study [2], the measured nascent internal energy contents of the resulting C_2H_2 fragments suggests that vinylidene ($^3B_2$) [reaction (3)] plays an insignificant role in the 193 nm dissociation relative to the other H(CN) + C_2H_2 channels [reactions (1) and (2)].
2. Both the three– and four–center eliminations of H(CN) are observed to be major dissociation channels with a relative (HCN : HNC) branching ratio of (3.34).
3. The HCN/HNC branching ratio is inconsistent with the previous *ab initio* generated potential energy surface for the dissociation reaction [17]. RRKM analysis based on the experimentally observed branching ratio, coupled with the measured average translational energies, provides support for the 101 kcal $mole^{-1}$ energy of the three–center transition state [reaction (2)] but suggests that the energy of the four–center transition state [reaction (1)] should be lowered to 90.5 kcal $mole^{-1}$.

4. Application of a combined statistical–prior / sudden–impulsive predictive energy distribution method was found to successfully reproduce the observed nascent average internal energies of the photofragments resulting from the H(CN) loss channels described by reactions (1) and (2) and hence offer further support of the proposed reaction mechanism for the molecular products.
5. The H_2 loss channels [reactions (4)(6)] occur in insignificant quantities relative to the observed H(CN) loss channels. Among the three possible H_2 loss channels, it is deduced that the four–center elimination [reaction (4)] is the dominant channel.
6. The dominant molecular elimination channels following the 193 nm dissociation of vinyl cyanide are therefore determined to be the three–center elimination of HCN + vinylidene ($^1A_1$) [reaction (2)] followed closely by the four-center elimination of HNC + acetylene [reaction (1)].

Acknowledgement

This work was supported in part by Basic Energy Sciences, U.S. Department of Energy, through Grant No. DEFG 02–86ER 134584. Laura Letendre's participation in this study was funded through a NASA Earth System Science Fellowship. Additionally, funding for myself and Matthew Nikow was provided by Temple University. All of the authors wish to thank Professor R. W. Field for inspiring discussions.

References

1. B. A. Balko, J. Zhang, and Y. T. Lee, *J. Chem. Phys.* **97**, 935 (1992).

2. A. Fahr and A. H. Laufer, *J. Photochem.* **34**, 261 (1986).
3. S. Satyapal, G. W. Johnston, R. Bersohn, and I. Oref, *J. Chem. Phys.* **93**, 6398 (1990).
4. E. F. Cromwell, A. Stolow, M. J. J. Vrakking, and Y. T. Lee, *J. Chem. Phys.* **97**, 4029 (1992).
5. E. Martinez–Nunez, A. F. Ramos, A. P. Gallego, and S. A. Vazquez, *Chem. Phys. Lett.* **369**, 1 (2003).
6. D. A. Blank, S. Weizhong, A. G. Suits, Y. T. Lee, S. W. North, and G. E. Hall, *J. Chem. Phys.* **108**, 5414 (1998).
7. E. Martinez–Nunez, S. A. Vazquez, F. J. Aoiz, L. Banares, and J. F. Castillo, *Chem. Phys. Lett.* **386**, 225 (2004).
8. K. Tonokura, L. B. Daniels, T. Suzuki, and K. Yamashita, *J. Phys. Chem. A* **101**, 7754 (1997).
9. J. L. Chang, *J. Chem. Phys.* **122**, 194321 (2005).
10. H. Katayanagi, N. Yonekuira, and T. Suzuki, *Chem. Phys.* **231**, 345 (1998).
11. D. K. Liu, L. Letendre, and H-.L. Dai, *J. Chem. Phys.* **115**, 1734 (2001).
12. L. Letendre, Ph.D. thesis, University of Pennsylvania, 2000.
13. D. A. Blank, A. G. Suits, Y. T. Lee, S. W. North, and G. E. Hall, *J. Chem. Phys.* **108**, 5784 (1998).
14. S. W. North and G. E. Hall, *Chem. Phys. Lett.* **263**, 148 (1996).
15. C. A. Bird and D. J. Donaldson, *Chem. Phys. Lett.* **249**, 40 (1996).
16. A. Fahr and A. H. Laufer, *J. Phys. Chem.* **96**, 4217 (1992).
17. A. Derecskei–Kovacs and S. W. North, *J. Chem. Phys.* **110**, 2862 (1999).

18. L. Letendre and H-.L. Dai, *J. Phys. Chem. A* **106**, 12035 (2002).
19. P. A. Mullen and M. K. Orloff, *Theor. Chim. Acta* **23**, 278 (1971).
20. *CRC Handbook of Chemistry and Physics, 75th ed.*, edited by D. Lide (CRC Press, Cleveland, OH, 1994/95).
21. N. Nishi, H. Shinohara, and I. Hanazaki, *J. Chem. Phys.* **77**, 246 (1982).
22. G. V. Hartland, W. Xie, D. Qin, and H-.L. Dai, *Rev. Sci. Instrum.* **63**, 3261 (1992).
23. L. Letendre, H-.L. Dai, I. A. McLaren, and T. J. Johnson, *Rev. Sci. Instrum.* **70**, 18 (1999).
24. W. McNavage, W. Dailey, and H-.L. Dai, *Can. J. Chem.* **82**, 925 (2004).
25. M. J. Wilhelm, W. McNavage, R. Groller, and H-.L. Dai, *J. Chem. Phys.* **128**, 064313 (2008).
26. M. J. Wilhelm, M. Nikow, and H-.L. Dai, *J. Mol. Struct.* **883884**, 242 (2008).
27. A. G. Maki and G. C. Mellau, *J. Mol. Spectrosc.* **206**, 47 (2001).
28. A. G. Maki, W. Quapp, S. Klee, G. C. Mellau, and S. Albert, *J. Mol. Spectrosc.* **174**, 365 (1995).
29. M. Nezu, T. Amano, and K. Kawaguchi, *J. Mol. Spectrosc.* **192**, 41 (1998).
30. M. Nezu, T. Amano, and K. Kawaguchi, *J. Mol. Spectrosc.* **198**, 186 (1999).
31. M. Herman, A. Camparque, M. I. El Idrissi, and J. V. Auwera, *J. Phys. Chem. Ref. Data* **32**, 921 (2003).
32. A. G. Maki, G. C. Mellau, S. Klee, M. Winnewisser, and W. Quapp, *J. Mol. Spectrosc.* **202**, 67 (2000).
33. A. Jolly, Y. Benilan, and A. Fayt, *J. Mol. Spectrosc.* **242**, 46 (2007).

34. M. Herman, M. I. El Idrissi, A. Pisarchik, A. Camparque, A-.C. Gaillot, L. Biennier, G. Di Lonardo, and L. Fusina, *J. Chem. Phys.* **108**, 1377 (1998).

35. Y. Benilan, A. Jolly, F. Raulin, and J. C. Guillemin, *Planet. Space Sci.* **54**, 635 (2006).

36. D. E. Milligan and M. E. Jacox, *J. Chem. Phys.* **47**, 278 (1967).

37. W. Quapp, M. Hirsch, G. C. Mellau, S. Klee, M. Winnewisser, and A. G. Maki, *J. Mol. Spectrosc.* **195**, 284 (1999).

38. M. J. Frisch et al., GAUSSIAN03, Revision C.01, Gaussian, Inc., Wallingford, CT, 2004.

39. A. G. Maki and R. L. Sams, *J. Chem. Phys.* **75**, 4178 (1981).

40. K. M. Ervin, J. Ho, and W. C. Lineberger, *J. Chem. Phys.* **91**, 5974 (1989).

41. R. L. Hayes, E. Fattal, N. Govind, and E. A. Carter, *J. Am. Chem. Soc.* **123**, 641 (2001).

42. Z. H. Loh and R. W. Field, *J. Chem. Phys.* **118**, 4037 (2003).

43. S. Zou, J. M. Bowman, and A. Brown, *J. Chem. Phys.* **118**, 10012 (2003).

44. D. Qin, Ph.D. thesis, University of Pennsylvania, 1996.

45. G. V. Hartland, D. Qin, and H-.L. Dai, *J. Chem. Phys.* **100**, 7832 (1994).

46. G. V. Hartland, D. Qin, and H-.L. Dai, *J. Chem. Phys.* **102**, 8677 (1995).

47. C. D. Pibel, E. Sirota, J. Brenner, and H-.L. Dai, *J. Chem. Phys.* **108**, 1297 (1998).

48. G. V. Hartland, D. Qin, and H-.L. Dai, *J. Chem. Phys.* **107**, 2890 (1997).

49. G. H. Herzberg, *Spectra of Diatomic Molecules, Molecular Spectra and Molecular Structure* (D. Van Nostrand Company, Princeton, NJ, 1939), Vol. I.

50. G. E. Caledonia, B. D. Green, and R. E. Murphy, *J. Chem. Phys.* **71**, 4369 (1979).

51. Y. Badr, S. A. El–wanees, and M. A. Mahmoud, *J. Photochem. Photobiol. A* **168**, 31 (2004).

52. A. Maki, W. Quapp, and S. Klee, *J. Mol. Spectrosc.* **171**, 420 (1995).

53. R. Zare, *Angular Momentum: Understanding Spatial Aspects in Chemistry and Physics* (Wiley–Interscience, New York, 1988).

54. A. Hansel, C. Scheiring, M. Glantschnig, and W. Lindinger, *J. Chem. Phys.* **109**, 1748 (1998).

55. C. H. Hu and H. F. Schaefer, *J. Phys. Chem.* **97**, 10681 (1993).

56. N. Goldberg and H. Schwarz, *J. Phys. Chem.* **98**, 3080 (1994).

57. T. Koops, W. M. A. Smit, and T. Visser, *J. Mol. Struct.* **112**, 285 (1984).

58. S. W. North, D. A. Blank, J. D. Gezelter, C. A. Longfellow, and Y. T. Lee, *J. Chem. Phys.* **102**, 4447 (1995).

59. D. A. Blank, S. W. North, D. Stranges, A. G. Suits, and Y. T. Lee, *J. Chem. Phys.* **106**, 539 (1997).

60. D. Townsend, S. A. Lahankar, S. K. Lee, S. D. Chambreau, A. G. Suits, X. Zhang, J. Rheinecker, L. B. Harding, and J. M. Bowman, *Science* **306**, 1158 (2004).

61. S. A. Lahankar, V. Goncharov, F. Suits, J. D. Farnum, J. M. Bowman, and A. G. Suits, *Chem. Phys.* **347**, 288 (2008).

62. P. L. Houston and S. H. Kable, *Proc. Natl. Acad. Sci. U.S.A.* **103**, 16079 (2006).

63. A. G. Suits, *Acc. Chem. Res.* **41**, 873 (2008).

64. R. D. van Zee, M. F. Foltz, and C. B. Moore, *J. Chem. Phys.* **99**, 1664 (1993).

65. J. T. Muckerman, *J. Phys. Chem.* **93**, 179 (1989).

66. G. E. Busch and R. K. Wilson, *J. Chem. Phys.* **56**, 3626 (1972).

67. K. A. Trentelman, S. H. Kable, D. B. Moss, and P. L. Houston, *J. Chem. Phys.* **91**, 7498 (1989).

68. D. H. Mordaunt, D. L. Osborn, and D. M. Neumark, *J. Chem. Phys.* **108**, 2448 (1998).

Chapter 6

Collisional deactivation of vibrationally highly excited hydrogen isocyanide (HNC)

6.1 INTRODUCTION

The linear triatomic cyanides, hydrogen isocyanide (HNC) and hydrogen cyanide (HCN), have both received a considerable amount of attention from the experimental [2] and theoretical [3] communities. As depicted in figure 6.1, HNC is the energetically less stable isomer of HCN, with an associated zero point energy difference of around 5,000 cm^{-1} [4]. Additionally, the two species are separated by a calculated isomerization barrier of $\approx$ 11,000 cm^{-1} relative the HNC zero point energy [4].

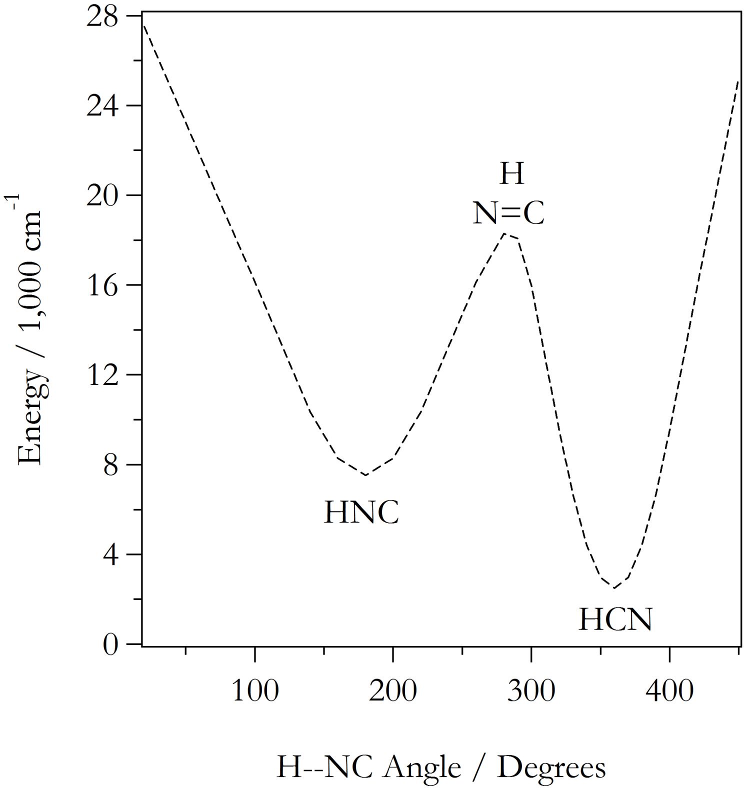

Figure 6.1
A calculated two-dimensional representation of the HCN / HNC potential energy surface when viewed as a function of the H–CN bending angle.

Together, the combined pair form an experimentally (and theoretically) novel system for studying a simple hydrogen migration as well as for modeling simple isomerization dynamics. In terms of a general isomerization process, it is well understood that as the internal energy of a given species increases, the probability and rate of the isomerization reaction likewise increases. In the same way, however, it has been generally observed that (for systems of sufficient molecular density) as internal energy increases the rate of collisional deactivation also increases. As a result, it becomes apparent that conditions which favor isomerization also seem to favor collisional deactivation. In a fundamental sense then, isomerization and collisional deactivation should be viewed as competing processes. One lingering question of course, is how the associated rates of each process compare with one another and whether or not both are significant or if one of the two is expected to dominate.

Furthermore, it is of interest to note that both HCN and HNC have been observed to be present in numerous environments of astrophysical interest including: comets, dark clouds, stars, and even alien atmospheres [5]. The source and abundance ratios of HNC, when compared with HCN, is currently an open question in the astrophysical community. In particular, HNC is often found in concentrations that are equal to or greater than HCN, which is in stark contrast to the calculated (100K) abundance ratio of ca. 1×10^{-30} [6]. Given that stars are well known sources of ultra-violet radiation, coupled with the known presence of astrophysical cyano- containing molecules, suggests a reasonable source for photochemically generated HNC and HCN. If such chemistry were to occur in a molecularly dense environment (such as comets, dark clouds or alien atmospheres), and if collisional deactivation is competitive with isomerization; then different astrophysical environments (depending upon the specific cyano- precursors present) would therefore be expected to yield HNC and HCN in unique abundance ratios.

The primary focus of this paper is the experimental determination of the vibrational to translational (V-T) energy transfer efficiency of vibrationally excited hydrogen isocyanide (HNC). In one regard, this is a continuation of our examination of the 193 nm photolysis of vinyl cyanide [1] in which we observed that the two main dissociation pathways yield hydrogen cyanide (HCN) and vinylidene (H_2CC) (with an upper bound quantum yield of $\Phi = 0.77$) as well as HNC and acetylene (HCCH) ($\Phi = 0.23$). Despite the fact that HNC is found to be only the third most abundant photofragment (following HCN and HCCH respectively), the observed IR spectral signature is remarkably clean (i.e. free from overlapping features) and hence serves as a convenient means of probing energy transfer. In an effort to ensure that we examine effects specific to (V-T) energy transfer, we limit the identity of the collider species employed to the (*relatively*) inert rare-gas atomic series: helium (He), argon (Ar), krypton (Kr) and xenon (Xe).

In what follows, we will examine the collisional deactivation of vibrationally excited HNC through modeling of the observed ν_1 NH and ν_3 NC IR emission stretch modes of HNC. Hydrogen isocyanide, with average internal energies of up to 25 kcal mole^{-1}, is generated through the 193 nm photolysis of vinyl cyanide and collisionally quenched with the rare-gas atomic colliders He, Ar, Kr, and Xe. Time-resolved fittings of the observed emission spectra provide measurements of the HNC average internal energy as a function of the number of rare-gas collisions, which can subsequently be used to derive the average energy lost per collision (e.g. the efficiency of energy transfer). The observed energy transfer efficiencies will then be modeled using the V-T relaxation probabilities of Schwartz, Slawsky, and Herzfeld (SSH)[7], in which the intermolecular interaction energy of the associated complexes can be obtained through fittings of the experimentally measured values. Additionally, *ab initio* calculations, capable of a modeling the various intermolecular interaction energies, will be employed to aid in a quantitative description of the observed collisional deactivation efficiencies.

6.2 EXPERIMENTAL

A more detailed description of the experimental setup has been given elsewhere [14-17]. Briefly, the output from an ArF excimer laser ($\lambda = 193nm, 20Hz, \leq 50mJ/pulse$) (Lambda Physik, LPX 200) was collimated through a photolysis cell mounted with two CaF_2 windows. The sample typically contained 10 mTorr of precursor molecules and 4 Torr of helium (He), argon (Ar), krypton (Kr), or xenon (Xe) bath gas under constant flow conditions. Pressure in the cell was monitored with a capacitance manometer (MKS Baratron, 0-10 Torr). Emission after the photolysis laser pulse was collected perpendicular to the laser propagation axis by a gold–mirror Welsh cell arrangement in the photolysis cell and then collimated and focused into the FTIR spectrometer by two KBr lenses that match the f/4 focusing characteristics of the spectrometer. The spectrometer (Bruker IFS 66/s) was equipped with an interferometer capable of time-resolved step–scan measurements and a mercury cadmium telluride detector (HgCdTe J15D14, *EG&G* Judson Technologies, 500 ns rise time, 750-10 000 cm^{-1} spectral range). The internal cavity of the FTIR was continually flushed with a FTIR purge gas generator (75-45, Parker Balston). The spectral response of the HgCdTe detector was calibrated with a Globar® source, which was modeled as a perfect blackbody.

Interferograms for this work were recorded at 100 ns time intervals averaging 200 laser shots per interferogram point for a total observation window of 20 μs. The time–resolved interferometric signal from the detector was amplified by a fast amplifier (Stanford Research Systems SR445, DC-300 MHz) before reaching the transient digitizer (Spectrum PAD82a, 100/200 MHz), which was triggered by a fast photodiode that monitored the excimer output. Subsequent Fourier transformation of each interferogram yields a time–resolved spectrum at every 100 ns. To further enhance the observed spectral resolution, spectra were synchronously cross correlated in bins of 10 to yield representative spectra spanning 1.0 μs intervals [18-20]. The spectral resolution was typically set at 12 cm^{-1}.

Acrylonitrile ($\geq$99%) (Sigma–Aldrich) was processed with several freeze–pump–thaw cycles before use and purity checked with IR absorption spectroscopy. Helium, argon, krypton, and xenon gas from the supplier (Spectra Gas, research grade, 99.9%) was used directly. Unphotolyzed sample was recollected after each experiment at liquid nitrogen temperature and purified for further use.

6.3 RESULTS AND ANALYSIS

6.3.1 Time-resolved IR emission spectra

Chapter five of this thesis characterized the time-resolved FTIR emission spectra following the 193 nm photolysis of both vinyl cyanide ($H_2CC(H)CN$) and deuterated vinyl cyanide ($D_2CC(D)CN$). Those results are directly related to the current topic of discussion and thus we review those points of highest relevance here. Figure 6.2 highlights the measured time-resolved emission spectra from the undeuterated sample. As was discussed in the previous chapter, there are five distinct emission features which have been characterized as originating from acetylene (HCCH), hydrogen cyanide (HCN), hydrogen isocyanide (HNC), cyanoacetylene (HCC-CN), and the α-cyanovinyl radical (H_2CC-CN) [21] through the following reaction pathways:

$$H_2CC(H)CN \rightarrow HCCH + HNC, \tag{6.1}$$

$$\rightarrow (H_2C = C[^1A_1] + HCN) \rightarrow HCCH + HCN, \tag{6.2}$$

$$\rightarrow HCCCN + H_2, \tag{6.3}$$

$$\rightarrow H_2C = CCN + H. \tag{6.4}$$

Of key importance for the current study, the features originating from HNC with fundamental transitions at 2023 cm^{-1} (ν_3 NC stretch) and 3652 cm^{-1} (ν_1 NH stretch), exhibit partial rotational resolution and are both free of significant overlapping transitions from other photofragments. We note that the ν_3 CN stretch of HCN has a fundamental transition at 2097 cm^{-1} which is in partial overlap with the ν_3 NC stretch of HNC. Furthermore, we have previously shown that photolysis of vinyl cyanide (at 193 nm) produces HCN in an approximate (3:1) ratio with HNC, suggesting that HCN should be contributing to the 2000 cm^{-1} feature. Nevertheless, the CN stretch of HCN has an insignificant transition dipole moment of only 0.001362 Debye [22], hence transitions from the ν_3 CN stretch of HCN will be buried in the noise of our spectra. Thus, despite a negligible HCN contribution, the time-resolved emission spectra following the 193 nm photolysis of vinyl cyanide effectively exhibits a clean HNC signal.

The two clusters of HNC transitions (shown in figure 6.2) exhibit sizable anharmonic shifts (most notably the NH stretch at 3652 cm^{-1}), indicating that HNC is generated vibrationally hot. In prior studies [23], we have shown how spectral modeling of such features (i.e. free from overlap and shifting) can be used as a means of measuring the internal energy content as a function of time. By varying the identity of the collisional collider (and repeating the photolysis reaction), we can gain insight into the energy transfer efficiency of the species of interest. For the current study, we have examined the collisional deactivation of vibrationally excited HNC with the set

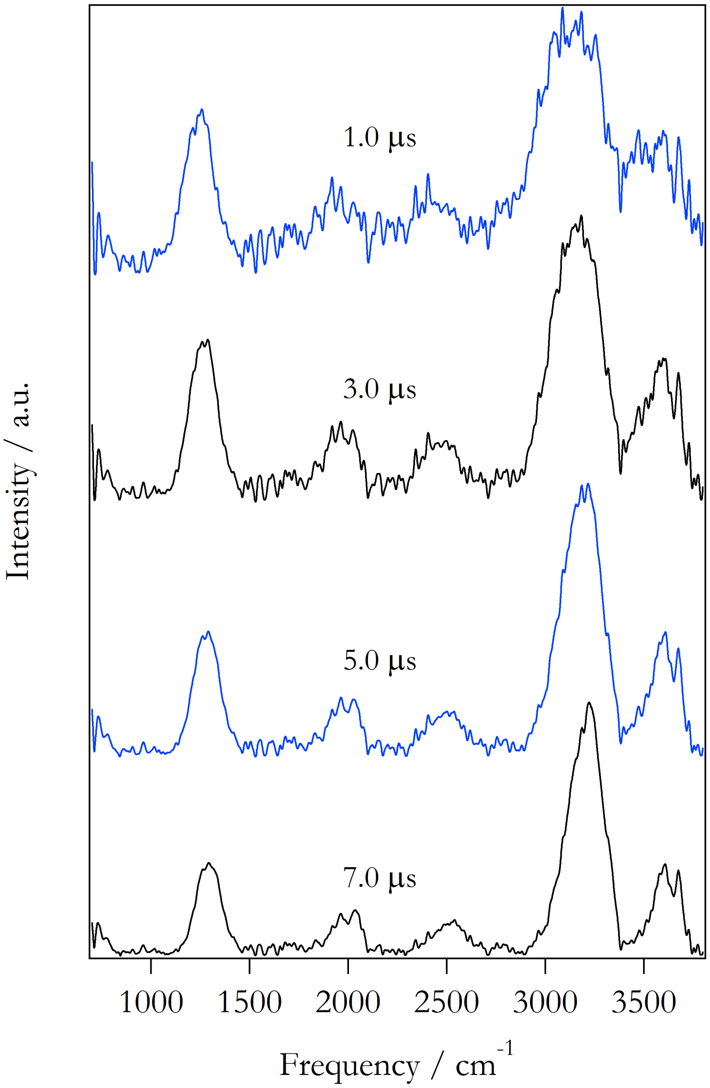

Figure 6.2
Time-resolved infrared emission spectroscopy following the 193 nm photolysis of vinyl cyanide. The spectra exhibit features from acetylene, hydrogen cyanide, hydrogen isocyanide, the alpha cyanovinyl radical and cyanoacetylene.

of rare-gas atoms: helium (He), argon (Ar), krypton (Kr) and xenon (Xe). As expected, the observed emission features following the dissociation are qualitatively invariant with respect to the specific collider species employed. It is only when one considers the time-dependence of the associated features (e.g. intensity and spectral width) that the effect of a given collider is observed.

6.3.2 Measuring the average internal energy $\langle E \rangle$ of HNC

Infrared emission spectroscopy has proven itself time and again as a novel means for monitoring the internal energy content of a given species of interest following either photodissociation or optical pumping [23]. The means of analysis have been described in great detail previously and will only be briefly reviewed. Modeling of the IR emission bands (from a given molecule) begins with the calculation of all of the available ro-vibrational levels up to a physically meaningful upper bound energy. Transition frequencies, permitted by the appropriate selection rules (e.g. $\Delta\nu_k$ = -1, ΔJ = 0, ± 1), are then determined by direct energy difference and assigned intensities largely through a combination of the harmonic scaling rule ($I_{n-1\leftarrow n} = nI_{0\leftarrow 1}$) [24] and Hönl-London factors [25]. To limit the number of necessary fitting parameters, the vibrational manifold of the species of interest is partitioned into evenly spaced energy bins. An assumption of equal probable population of all energy levels per bin then permits the generation of representative bin spectra; composed of the normalized sum of allowed transitions within a given bin. The complete set of bin spectra form a reduced basis set which makes fitting the experimental emission spectra a much more manageable task. In the past, we have found success in fitting spectra through either of two ways: free-form fits in which the bin populations are left as fitting parameters [26], as well as constrained fits in which the bin populations were expressed with analytical functional forms [23]. It has often been observed that high energy populations are typically well represented by Gaussian functional forms while low energy populations are best described with exponential functions.

Maki and Mellau have previously measured the high-resolution emission spectrum of HNC [27] by heating a static HCN cell to a temperature of 1370 K. Subsequent fittings of the resulting spectra lead to the experimental determination of the vibrational spectral constants (ω_i, χ_{ij}, y_{ijk},...) of HNC for levels up to 6,000 cm^{-1} above the zero point energy. Using the experimental fit constants, we modeled the HNC vibrational manifold for energies up to 10,000 cm^{-1} above the ZPE, and calculated a basis set of emission spectra for the ν_1 NH and ν_3 NC stretch modes of HNC. We note that while each of the individual ro-vibrational levels of HNC were determined with both harmonic and anharmonic spectral constants, the allowed IR emission transitions for the calculated spectra were constrained using the rigid–rotor/harmonic oscillator selection rules ($\Delta\nu_{1,3} = -1$; $\Delta l = 0, \pm 1$; $\Delta J = 0, \pm 1$).

The time-resolved HNC emission spectra were fit to a population distribution ($P^j(t)$) using only three variable parameters:

$$P^j(t) = \frac{\alpha_t}{\sqrt{2\pi}} exp\left(\frac{-hcE_j}{k_B T^t_{vib}}\right) + \Phi_t; \tag{6.5}$$

in which for a given time (t), α_t is an intensity scaling factor, Φ_t is a baseline correction, and T^t_{vib} is the vibrational temperature. Figure 6.3 highlights a typical spectral fitting result for the ν_1 NH and ν_3 NC stretch modes of HNC. The key result from each spectral fitting is the associated vibrational temperature (T^t_{vib}). Each temperature describes an ensemble population distribution of HNC and hence relates directly to the average internal energy $\langle E(t)\rangle$. A contour plot highlighting the evolution of the total internal energy (as a function of time) is shown in the inset of figure 6.3. Subsequent two-dimensional plots of the corresponding average internal energies reveal that $\langle E(t)\rangle$ is well described by an exponential functional form; from which it is possible to back extrapolate to the nascent (t=0) HNC internal energy $\langle E(0)\rangle$. For all atomic colliders examined (Rg = {He, Ar, Kr, Xe}), it is observed that HNC is generated with a common nascent internal energy of $\langle E(0)\rangle = 24.5 \pm 1.4$ kcal mole^{-1}. We note that this nascent internal energy is in excellent agreement with the $\langle E(0)\rangle = 24.0 \pm 7.0$ kcal mole^{-1} value measured in the HNC (m/e 27) photoionization spectrum of Blank *et al* [28]. Additionally, it is worth mentioning that the measured nascent internal energy (24.5 ± 1.4 kcal mole^{-1}) falls about 5 kcal mole^{-1} below the calculated barrier of isomerization (29.8 kcal mole^{-1}) to HCN [29]. It is therefore reasonable to suggest

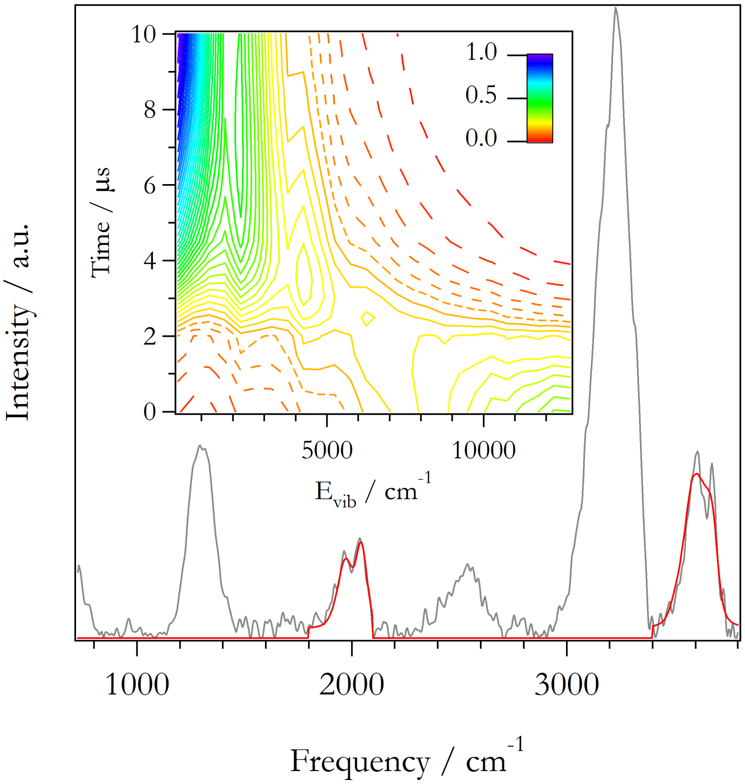

Figure 6.3
Example fitting of the ν_1 NH and ν_3 NC stretch features of hydrogen isocyanide, 13 μs following the arrival of the photolysis pulse. The inset contour plot highlights the HNC internal energy distribution as a function of time.

that, under the current experimental conditions, none of the HNC population will be lost to HCN via isomerization. Subsequently, the common nascent internal energy observed for all atomic colliders, coupled with the close quantitative agreement with the PTS study [28], highlight the accuracy of our modeling of the HNC emission spectra and ultimately provide further confidence in the obtained results.

6.3.3 Determination of $\langle \Delta E \rangle$ as a function of $\langle E \rangle$

Having fit all of the available emission spectra, we thus obtain a time-resolved measure of the average internal energy $\langle E(t) \rangle$ content of HNC. For the current study however, we seek to delineate the various energy transfer efficiencies of HNC with the series of inert atomic collider species. In this regard, as each atomic collider possesses a unique collisional frequency, time alone becomes a poor basis for comparison. Therefore, in an effort to put all of the data on a common footing, we examine the average internal energy as a function of the total number of collisions Z (where Z is related to partial pressure, collisional frequency, and time via $Z = \sum Z_{LJ}^{k} P_k t$). With that said, we note that our reaction cell contains a complex mixture of gases (especially after the arrival of the photolysis pulse), which warrants some discussion before we explicitly define Z.

As outlined previously, the initial gas mixture in the photolysis cell is composed of 4,000 mTorr of the rare-gas collider (He, Ar, Kr, or Xe) and 10 mTorr of the precursor sample, vinyl cyanide. Based upon laser power measurements before and after the gas cell, only about ca. 10% of the vinyl cyanide undergoes photolysis, yielding at most 1 mTorr of any given photofragment. Furthermore, we have previously shown that the two dominant dissociation pathways yield HCN + HCCH

(Φ=77%) and HNC + HCCH (Φ=23%) [1], where the quoted quantum yields represent reasonable upper bound limits. In this context then, there is at most 0.23 mTorr of HNC present in the photolysis cell at any given moment. The partial pressure of the rare-gas atomic collider is therefore calculated to be more than 17,000 times greater than HNC, suggesting that the collisional quenching of HNC should thus be dominated by the rare-gas atomic colliders. This prediction is further justified by the fact that the identity of the atomic collider is the only variation from one experiment to the next. As a result, if the quenching of HNC was not controlled by the atomic collider, each resulting series of time-resolved spectra (with the exception of noise) would be identical.

For a gaseous mixture of (m) different components, the average internal energy of a given species can be expressed in closed form as a sum:

$$\langle E(Z)\rangle = \sum_{m} Z_{LJ}(m) t_{\lambda} P_m \langle \Delta E(Z)\rangle_m, \tag{6.6}$$

in which $Z_{LJ}(m)$ is the Lennard-Jones collisional frequency, t_{λ} is a representative measure of time following the arrival of the photolysis pulse, P_m is the partial pressure, and $\langle \Delta E(Z)\rangle$ is the average energy lost per collision. Following the discussion above, it has been shown that the rare-gas colliders dominate the quenching process and hence (after some rearrangement) equation 6.6 can be greatly simplified down to a single expression:

$$\langle \Delta E(Z)\rangle_{Rg} = \frac{d\langle E(Z)\rangle}{dZ_{Rg}}, \tag{6.7}$$

which shows that under the current experimental conditions, $\langle \Delta E(Z)\rangle$ is simply the instantaneous slope of the $\langle E(Z)\rangle$ vs. Z plot. Figure 6.4 highlights the measured internal energy of HNC as a function of the total number of rare-gas collisions for the combined series {He, Ar, Kr and Xe}. As discussed in the prior section, the experimental $\langle E(Z)\rangle$ vs. Z plots can be described by exponential functions of Z, or more generally as:

$$\langle E(Z)\rangle = \Omega_0 + \sum_{j>0} \Omega_j \times exp\left(-k_j Z\right), \tag{6.8}$$

where the Ω_i terms relate to the magnitude of the average internal energy (in units of cm^{-1}) and the k_i terms describe the associated relaxation rates (in units of reciprocal collision numbers, Z^{-1}). Each of the $\langle E(Z)\rangle$ vs. Z plots of figure 6.4 are well described by single exponential functional forms, thus yielding single deactivation rate constants

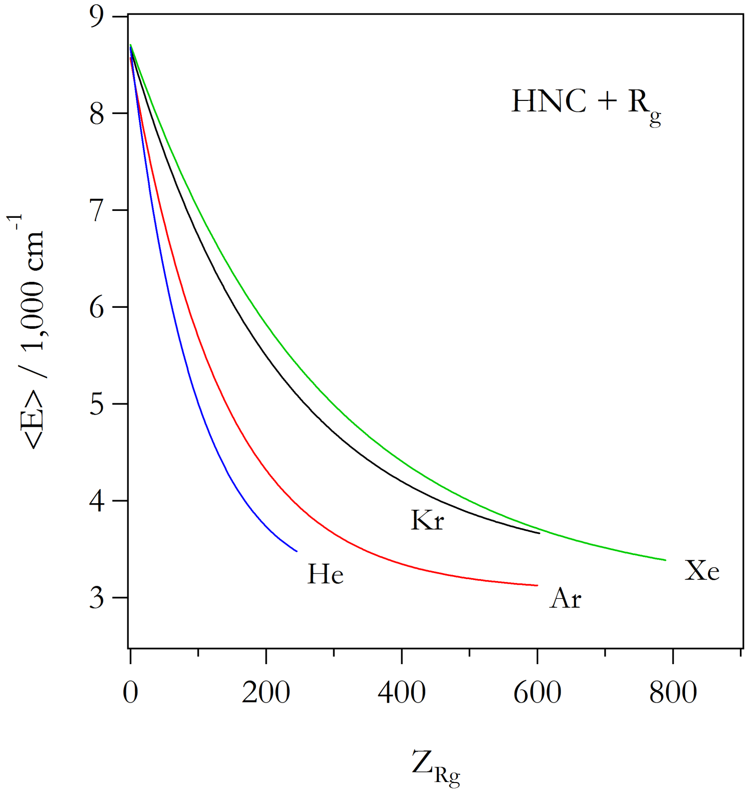

Figure 6.4
Measured average internal energy content of HNC as a function of the number inert atomic collisions, when quenched by He, Ar, Kr and Xe.

for each Rg collider. Fitting constants for the various HNC + Rg systems, including the corresponding Rg relaxation rates as well as the nascent internal energies, have been tabulated in table 6.1. Moreover, the utility of the above functional form (equation 6.8) is that it is readily differentiated, as necessitated by equation 6.7, to yield an expression of the average energy lost per collision:

$$\langle \Delta E(Z) \rangle = -\sum_{j>0} k_j \Omega_j \times exp\left(-k_j Z\right). \tag{6.9}$$

As portrayed in figure 6.5, application of equation 6.9 allows for an experimental examination of the energy transfer efficiency (i.e. $\langle \Delta E(Z) \rangle$) of HNC when collisionally quenched with the rare-gas atoms {He, Ar, Kr, and Xe}. We note that the observed efficiency follows a well-behaved reduced mass trend in which He is found to be the most efficient quencher, followed by Ar, Kr, and finally Xe.

Rg	$k_1 \times 10^2$ / Z^{-1}	Ω_0 / cm^{-1}	Ω_1 / cm^{-1}	$\langle E \rangle_0$ / cm^{-1}
He	1.058	3056.6	5623.6	8680.2
Ar	0.738	3059.3	5513.3	8572.6
Kr	0.447	3300.3	5368.3	8668.6
Xe	0.356	3045.8	5663.4	8709.2

Table 6.1
Fitting results for the $\langle E \rangle$ vs. Z plots for the various HNC + Rg systems highlighting the measured nascent (Z=0) average internal energies as well as the associated HNC + Rg relaxation rate constants (k_1).

Prior studies, from this laboratory [23,30-32] as well as others [33-37], have shown that collisional energy transfer from non-aromatic molecules (with rare-gas atomic colliders) is typically very *inefficient*. Specifically, in the absence of electronic coupling (even at high average internal energies) $\langle \Delta E \rangle$ values typical fall well below 10 cm^{-1} [23,30-37]. Therefore, with observed $\langle \Delta E \rangle$ values greater than 10 cm^{-1} for most energies examined, it is reasonable to infer that vibrational to translational (V-T) energy transfer from HNC is an uncommonly *efficient* process.

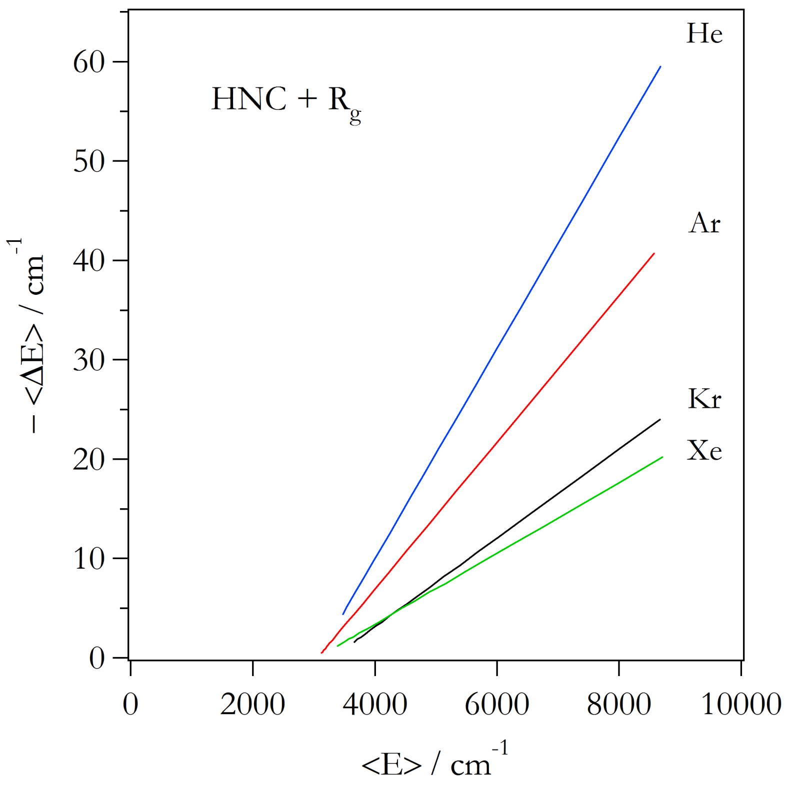

Figure 6.5

Measured results of the average HNC internal energy lost per collision with the various rare-gas colliders (He, Ar, Kr, Xe), as a function of the average HNC internal energy.

6.4 DISCUSSION

6.4.1 Ab initio calculations:

In addition to experimental measurements, *ab initio* calculations were employed to aid in a quantitative description of the results. In general, it is of interest to examine the intermolecular electrostatic interaction of the HNC / Rg complexes as a means for describing the observed energy transfer trends. Specifically, HNC is known to possess a strong permanent dipole moment of 3.05 Debye [38], which would readily polarize the electron cloud of an approaching rare-gas atom and thus result in a dipole-induced dipole attractive interaction. As the polarizabilities of the rare-gas atoms increase with size, it is to be expected that the larger atomic colliders will therefore exhibit stronger interactions. Additionally, further analysis (to be discussed in a later section) based upon the theory of vibrational relaxation of Schwartz, Slawsky, Herzfeld, and Tanczos (SSHT) [7,39] requires knowledge of the associated HNC / Rg interaction energies. As direct experimental energies are not yet available, it is thus necessary to supplement the required values with theoretical energies.

All calculations were carried out on the GAUSSIAN 03 package of programs [40]. In particular, the supermolecule method [41] was used to examine the interaction energy (as a function of bond distance R) for the complete series of HNC / Rg complexes. In an attempt to make the analysis more tractable, only the linear approach orientation of the rare-gas atom / fixed linear HNC fragment (i.e. Rg—H-NC) was examined. We justify this assumption through direct comparison of the prior theoretical examinations of Toczlyowski et al. [42] (HCN, CCSD[T]/aug-cc-pVTZ + (33221)), McDowell [43] (HCN and HNC, MP2/6-311++G(2d,2p)), and Christoffel et al. [44] (HCN/HNC, CISD / aug-cc-pVTZ and aug-cc-pVDZ); in which the linear hydrogen approach was found to contain the global energy minimum for all complexes examined.

For each iteration of the approaching (Rg) atom, two distinct (though coupled) calculations were performed. As an initial step, the bond lengths of the linear

(HNC) fragment were optimized using second-order Møller-Plesset perturbation theory with full core electron correlation [MP2(full)]. Next, using the MP2 optimized HNC geometry, the energy of the total (HNC / Rg) system was then determined with forth-order Møller-Plesset perturbation theory [MP4(full)]. We note additionally that our analysis is focused solely on the relative depth of the attractive interaction. In this regard, all quoted energies are given relative to the energy of the associated HNC / Rg complex at an approximate infinite separation (i.e. $R_{Rg-HNC} = 2{,}000$ Å). For each calculation, the augmented correlation consistent polarized triple zeta basis set (aug-cc-pVTZ) was used to describe all atoms. Additionally, a supplemental (3s3p2d1f) set of bond functions [41] were centered on a ghost atom maintained midway between the approaching rare-gas atom and the hydrogen. Basis set superposition error (BSSE) was treated by employing the counterpoise procedure of Boys and Bernardi [45].

6.4.1.1 HCN interaction energies: CCSD(T) vs. MP4(full)

Using the high-level CCSD(T) calculated potential energy surfaces, Toczylowski et al. [42] were able to generate accurate predictions for the rotational energy levels of the various HCN complexes. The calculated energy levels (as well as the associated bound rotational transitions) of the He, Ar, and Kr complexes were found to be in excellent agreement with prior experimental microwave spectral observations [46-48]. Unfortunately, a comparable set of calculations at the CCSD(T) level of theory, for the HNC series of complexes, are not yet available in the literature. At present, the best (published) potential energy scan for the HNC complexes has been performed by McDowell [43] at the comparably modest MP2/6-311++G(2d,2p) level of theory. In his study, McDowell sought to compare the associated ν_1 (HC /

HN) mode frequency shifts associated with the H(CN) / rare-gas complexes [43], and began by examining the interaction energies for both series of complexes. When compared with the CCSD(T) results of Toczlyowski et al. [42] (for the HCN complexes), the MP2 calculation yields BSSE-corrected interaction energies which are all severely underestimated by a minimum of 40%. It is in this regard that we are compelled to carry out additional *ab initio* calculations of the interaction energies for the set of HNC complexes.

Despite the general availability of the CCSD(T) method in the various quantum chemistry packages [39,49,50], this level of theory (as applied to a potential energy scan at least) is still largely impractical for use by the non-specialist. Nevertheless, as our focus is limited to a single angle of approach (e.g. linear Rg—H-NC), the more computationally thrifty MP4(full) method stands as a reasonable compromise between cost and accuracy. Thus as an initial check of the quality of the calculated MP4 energies, we have re-examined the HCN complexes of Toczlyowski [42] at the MP2(full)//MP4(full) level of theory as outlined above. For all complexes examined, the resulting MP4(full) calculations produced relative HCN interaction energies that were all within -6.5% of the corresponding CCSD(T) values. One notable exception was the HCN / Ne complex for which the MP4(full) calculation produced an interaction energy that was +3.5% deeper than the CCSD(T) value. As noted by Toczlyowski et al. [42], the Ne complex is uniquely sensitive to the size of the basis set employed, and therefore the deviation observed in the MP4 calculation is likely due to an under sampling of the basis set. Nevertheless, the close agreement observed between the remaining complexes, coupled with the fact that the complementary HNC / Ne complex was not examined in our study, suggests that the MP4(full)/aug-cc-pVTZ + (3s3p2d1f) method is suitable for our present purposes.

6.4.1.2 HNC interaction energies: MP4(full)

Following the success of the MP4 calculations with the HCN systems, we were therefore confident in applying the method to examine the associated HNC complexes. Table 6.2 highlights the BSSE-corrected interaction energies for all of the H(CN) / Rg complexes calculated at the MP2, MP4, and CCSD(T) levels of theory. As expected,

Rg–H(CN)	-De / MP2$^{(a)}$	-De / MP4$^{(b)}$	-De / CCSD(T)
He–HCN	18	28	30^{c}
Ne–HCN	14	59	57^{c}
Ar–HCN	79	138	147^{c}
Kr–HCN	104	169	179^{c}
He–HNC	29	43	46^{d}
Ne–HNC	31	–	–
Ar–HNC	132	215	230^{d}
Kr–HNC	170	266	284^{d}
Xe–HNC	–	527	564^{d}

(a) McDowell (Ref. 43) : MP2/6-311++G(2d,2p)
(b) This work : MP4(full)/aug-cc-pVTZ + (3s3p2d1f)
(c) Toczlyowski et al. (Ref. 42) : CCSD(T)/aug-cc-pV(T,Q)Z + (3s3p2d2f1g)
(d) This work : MP4(full) values scaled by +6.5%

Table 6.2
Comparison of the ab initio calculated interaction energies (De) for the series of H(CN) / Rg complexes determined at the MP2 (Ref. 43), MP4, and CCSD(T) (Ref. 42) levels of theory. All energies have been corrected for BSSE and are given in units of cm^{-1}.

the MP4 calculations for the HNC complexes show a distinct enhancement (relative to the MP2 values [43]) with associated well depths (i.e. interaction energies) that are all minimally 30% deeper. Additionally, we note that for all the rare-gas atoms considered, a decidedly stronger interaction is found in the HNC (rather than the HCN) complexes. Specifically, the magnitudes of the HCN interaction energies are all found to scale roughly as 67% of the associated HNC values. In the context of a dipole-induced dipole interaction, such a result is qualitatively reasonable given that HCN has a *slightly* weaker permanent dipole moment of 2.98 Debye compared with the 3.05 Debye value for HNC [38]. Furthermore, it is observed that the relative magnitudes of the various interaction energies, for both series of complexes, scale in a nearly identical fashion. In particular, for the set of Rg atoms {He, Ne, Ar, Kr, and Xe} (when considered relative to the He values); the MP4 energies for the HCN and HNC rare-gas complexes are observed to scale as (1:2:5:6:*) and (1:*:5:6:12), respectively (in which neither HCN / Xe nor HNC / Ne were examined). Thus, assuming that the dominant underlying interaction is common for both series of complexes, such a result provides confidence in the magnitudes of the calculated HNC interaction energies and further justifies their use for a continued analysis in later discussion sections.

6.4.2 Vibrational Relaxation: SSHT theory

As discussed in prior sections, the collisional deactivation of HNC with rare-gas atoms (He, Ar, Kr, and Xe) is observed to obey a well-behaved reduced mass trend in which the lightest collider (He) is found to be the most efficient quencher, followed by Ar, Kr, and finally the heaviest collider (Xe). Such a trend is highly reminiscent of the celebrated SSHT theory [7,39] of vibrational relaxation, and is therefore suggestive of the fact that SSHT theory may prove to be a fruitful means of explaining the observed interactions. The heart of SSHT theory is rooted in the determination of the probability of coupled (though opposing) energetic transitions occurring between two species involved in a bimolecular collision, and described by an impulsive interaction. In short, SSHT describes the probability of an interaction by which one collider species loses some quantity of energy $|\Delta E|$ while the other concurrently gains exactly $|\Delta E|$ of energy. For the current study, SSHT theory can be used to describe the probability that some portion of the vibrational energy of HNC will be converted into translational energy of the Rg collider. When examined over the experimentally sampled range of internal energies, the associated SSHT derived transition probabilities can be used to obtain a prediction of the average energy lost per collision, as a function of average internal energy.

6.4.2.1 Transitioning from $P^{j\leftarrow i}$ to $\langle \Delta E \rangle$:

The mechanics of SSHT theory have been outlined in great detail many times before, as such the interested reader is referred to the original reports [1,2] as well as the numerous review articles which have appeared throughout the years [51-56]. For the discussion at hand, it suffices to say that the probability ($P^{j\leftarrow i}$) of a given collision induced transition in HNC from an initial state $|\nu_1^i \nu_2^i(l)\nu_3^i\rangle$ to a final state $|\nu_1^j \nu_2^j(l)\nu_3^j\rangle$ (by a rare-gas atom R_g) can be described as the product of two separate physical interactions, i.e.

$$P^{j\leftarrow i} = P_{Rep}^{j\leftarrow i}\left(\Delta E, \mu\right) \times exp\left(\frac{-De}{k_B T}\right), \tag{6.10}$$

wherein $P^{j \leftarrow i}_{Rep}(\Delta E, \mu)$ refers to a purely repulsive interaction while the exponential term describes a constant long-range attraction with a corresponding interaction energy (De). It is of interest to note that the purely repulsive component ($P^{j \leftarrow i}_{Rep}(\Delta E, \mu)$) is directly *dependent* upon the initial and final vibrational states through the associated transition frequency (ΔE). In other words, the probability of a transition (as described by the purely repulsive interaction) depends upon the average internal energy content of the donor molecular species (in this case HNC). Conversely, the attractive component of the probability is completely *independent* of the internal energy and therefore behaves as a constant scaling factor that can either enhance or diminish the likelihood of a transition. In this regard, the attractive interaction energy (De) can therefore be left as a variable parameter and used to fit the experimentally measured $\langle \Delta E \rangle$ vs. $\langle E \rangle$ plots.

For a given initial state $|\phi_i\rangle$ (with corresponding energy E_i), there exists a variety of potential downward transitions (based upon the set of selection rules employed) to a set of states $\{\phi_j\}$, each with a specific transition probability $P^{j \leftarrow i}$. In this regard, each state $|\phi_i\rangle$ possesses a total transition probability $P(E_i)$ defined as the sum of probabilities over all allowed transitions:

$$P(E_i) = \rho(E_i)^{-1} \sum_k P^{k \leftarrow i}, \tag{6.11}$$

in which $\rho(E_i)$ relates to the total number of allowed transitions originating from the state $|\phi_i\rangle$. In a similar fashion, the average energy lost per collision for a given state (or series of states), can be directly related to the associated transition frequency (i.e. ΔE) weighted by the probability of that transition. Specifically, for a set of states $\{\phi_i\}$ spanning an energy range $\langle E_k \rangle = (E_k \pm \delta E)$, the average energy lost per collision $\langle \Delta E_k \rangle$ can be defined as the sum over all the allowed transitions weighted by the individual probabilities $P^{j\leftarrow i}$; i.e.

$$\langle \Delta E_k \rangle = N(E_k)^{-1} \sum_{i\,\epsilon\,k} P^{j\leftarrow i} \times \Delta E_i, \tag{6.12}$$

where N(E_k) corresponds to the total number of allowed transitions contained within the average energy range $\langle E_k \rangle$. As described by equation 6.10, the attractive component of the SSHT transition probability is completely independent of the vibrational states considered, and hence is readily extracted from the sum in equation 6.12. Therefore, expanding the probability term in equation 6.12 (and following some simple rearrangement), we find that the average energy lost per collision is likewise separable into repulsive and attractive components; i.e

$$\langle \Delta E_k \rangle = \langle \Delta E_k \rangle_{Rep} \times exp\left(\frac{-D_e}{k_B T}\right), \tag{6.13}$$

where $\langle \Delta E_k \rangle_{Rep}$ refers to the average energy lost based upon the purely repulsive interaction. The utility of equation 6.13 lies in the notion that the attractive term now represents a means of modifying the slope of the calculated $\langle \Delta E \rangle$ vs. $\langle E \rangle$ plots. Thus, in addition to representing a tool capable of fitting the experimental data, equation 6.13 can actually be used to extract experimental values of the HNC / Rg interaction energies.

6.4.2.2 SSHT fittings: (De = $0\ cm^{-1}$)

Before a fitting of the experimental $\langle \Delta E \rangle$ values can be attempted, a necessary initial step is the determination of the SSHT derived values via equations 6.10-13. Specifically, for a given energy range $\langle E_k \rangle$, a corresponding value of $\langle \Delta E_k \rangle$ can be determined. For the current study, the vibrational manifold of HNC was partitioned into evenly spaced (250 cm^{-1}) energy bins (up to a total internal energy of 10,000 cm^{-1}), yielding a series of forty discrete average energy bins. Each of the Rg colliders is initially analyzed in the limit of a purely repulsive interaction (De=0 cm^{-1}), for which application of equations 6.10-13 yield $\langle \Delta E_k \rangle_{Rep}$ values for each of the forty discrete energy ranges. When the series of $\langle \Delta E_k \rangle_{Rep}$ values (for each Rg collider) are plotted as functions of the corresponding average internal energy $\langle E_k \rangle$, a series of well-behaved linear functions are observed. As an initial comparison, both the experimental and SSHT derived $\langle \Delta E_k \rangle$ values were fit to linear functional forms, the resulting slopes of which have been recorded in table 6.3. While the purely repulsive SSHT values were able to qualitatively reproduce the observed reduced mass trend, both the individual magnitudes and corresponding ratios (relative to the He results) of the calculated slopes differed greatly from the experimental values. As exhibited by the associated slope ratios ($\Lambda^{Rg:He}$), SSHT theory (in the limit of a purely

Rg	$\left.\frac{\partial\langle\Delta E\rangle}{\partial\langle E\rangle}\right\|_{SSH}^{\times 10^4}$	$\Lambda_{SSH}^{Rg:He}$	$\left.\frac{\partial\langle\Delta E\rangle}{\partial\langle E\rangle}\right\|_{Exp}^{\times 10^4}$	$\Lambda_{Exp}^{Rg:He}$
He	275.6	1.00	105.8	1.00
Ar	19.7	0.07	73.8	0.70
Kr	9.2	0.03	44.7	0.42
Xe	1.5	0.01	35.6	0.34

Table 6.3
Linear fitting parameters (i.e. slopes) for the purely repulsive (i.e. De=0 cm^{-1}) SSHT as well as experimentally measured $\langle \Delta E \rangle$ vs. $\langle E \rangle$ plots of HNC + Rg. Also shown are the associated ratios ($\Lambda^{Rg:He}$) of the individual rare-gas slopes relative to the corresponding He values.

repulsive interaction) is observed to severely overestimate the relative efficiency of energy transfer in the He-complex. Nevertheless, as discussed previously, introduction and variation of a non-zero attractive interaction can be used to modify the calculated slopes and hence fit the experimentally measured values.

6.4.2.3 SSHT fittings: $(|De| \geq 0\ cm^{-1})$

Despite the fact that $\langle \Delta E \rangle$ is observed to be a linear function of $\langle E \rangle$, a number of issues arise when one attempts a fitting using the SSHT-derived parameters. First and foremost, the experimental and SSHT-derived values disagree upon the energy at which $\langle \Delta E \rangle$ goes to zero (i.e. $\mathrm{E}_{Exp} \approx$ 3,000 cm^{-1} and $\mathrm{E}_{SSHT} = 0\ \mathrm{cm}^{-1}$). One way to circumvent this issue is simply to offset the energy axis of the SSHT-derived values by a constant ≈3,000 cm^{-1}, then perform a *relative* fitting. Under such a method, the absolute magnitude of the calculated $\langle \Delta E \rangle$ values begin to lose their meaning, however the relative slopes of the individual plots remain faithful descriptors of the systems. We note that it is important to exert caution when attempting a fitting routine in which an arbitrary scaling factor is allowed. In particular, if we are no longer constrained by the magnitude of $\langle \Delta E \rangle$, there necessarily exists an infinite set of solutions whose *relative* slopes will match the experimentally measured values. Nevertheless, one useful aspect of this routine is that we are free to force any initial fit value for one (and only one) of the Rg systems. For the present case, we choose to fix the HNC / He interaction energy at the *ab initio* calculated value of -46 cm^{-1}, then fit the remaining systems relative to that initial value. We could have easily chosen to fix any one of the other interaction energies (i.e. Ar, Kr, or Xe) and varied the He result to fit.

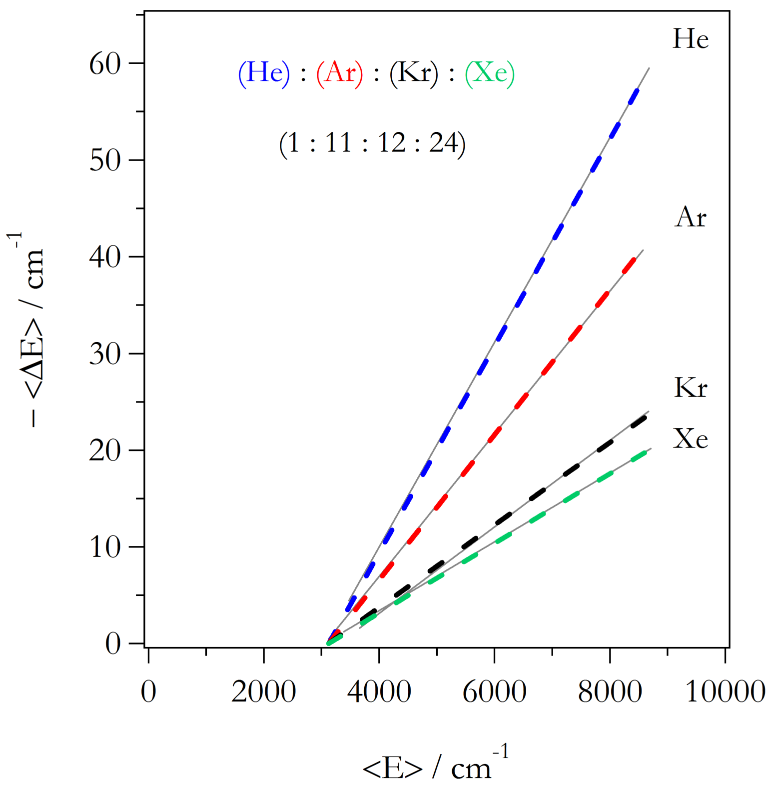

Figure 6.6
SSH(T) assisted fittings of the HNC + R_g $\langle \Delta E \rangle$ vs. $\langle E \rangle$ plots in which the HNC / He interaction energy was fixed at the ab initio determined value of -46 cm^{-1} and the remaining (Ar, Kr and Xe) interaction energies were left as fitting parameters. The magnitude of the SSH(T) calculated $\langle \Delta E \rangle$ values (right axis) are found to be about an order of magnitude greater than the experimentally measured values (left axis). The ratios of the HNC + Rg interaction energies, relative to He, have been determined as (1:11:12:24).

However, given that the He complex necessarily requires the least sophisticated basis set to model, it is reasonable to assume that the He interaction energies will be the most accurate of the series. Consequently, the SSHT *relative* fitting results for all of the HNC complexes, obtained through variation of the associated interaction energies (with a fixed He interaction energy), are presented in figure 6.6.

6.4.2.4 Interaction energies: SSHT vs. Theory

The SSHT measured interaction energies, as recorded in table 6.4, are observed to follow a well-behaved trend in which the larger (more polarizable) atoms exhibit stronger interactions. Furthermore, table 6.5 shows the comparison of the absolute magnitudes of the experimental and SSHT derived $\langle \Delta E \rangle$ values. It is of interest to note that the SSHT derived values are all around an order of magnitude greater than the experimental values. We note additionally that our application of SSHT theory employs harmonically scaled transition dipole moments as solutions for the various vibrational matrix elements appearing in the transition probabilities [57-59]. To that end, as the ν_2 bend of HNC has a notoriously strong fundamental transition dipole moment of 1.04 Debye [60], it is reasonable to expect that SSHT

Rg	-De / Exp (SSHT)	-De / Exp (SSHT)^a	-De / *ab intitio*^{b}
He–HNC	46	46	46
Ar–HNC	516	281	230
Kr–HNC	560	304	284
Xe–HNC	1,147	595	564

(a) Modified SSHT theory: $exp\left(\frac{-De}{k_BT}\right) \rightarrow exp\left(\frac{-2De}{k_BT}\right)$
(b) MP4(full)/aug-cc-pVTZ + (3s3p2d1f) values scaled by +6.5%

Table 6.4
Comparison of the SSHT derived and ab initio calculated intermolecular interaction energies (De) for the series of complexes HNC / Rg. In addition to traditional SSHT theory, interaction energies calculated using a modified version of the attractive component has been includes. All energies are given in units of cm^{-1}.

theory may overestimate the magnitudes of the $\langle \Delta E \rangle$ values. Nevertheless, as the associated matrix elements effectively act as scaling factors of the various transition probabilities, the relative $\langle \Delta E \rangle$ magnitudes (obtained through variation of the identity of the atomic collider) still yield faithful descriptions of the series of systems.

Above all else however, the most interesting aspect of the fitting results is that the SSHT measured interaction energies (with the exception of the He results) are all observed to be around twice as large as the *ab initio* calculated values. Figure 6.7 highlights a comparison of the SSHT derived interaction energies as a function of the *ab initio* calculated values. While a linear trend line is observed, the slope of the measured SSHT values is found to diverge from the perfect correlation fit line by a constant 0.5 factor. The observation of such an anomaly suggests the need for a re-examination of the origins of the SSHT attractive interaction term. In particular, Rapp and Kassal's [53] review portrays the origin of the long-range attractive interaction term as an *ad hoc* addition to the theory, as opposed to resulting from a rigorous *ab initio* derivation. In this regard, it is quite reasonable then to allow a slight modification to the exponential (attractive) term, i.e.

$$exp\left(\frac{-De}{k_B T}\right) \rightarrow exp\left(\frac{-2De}{k_B T}\right), \tag{6.14}$$

as a means of obtaining agreement between the *ab initio* and SSHT-derived interaction energies (De). As expected, when the experimental results are re-fit using relation 6.14, the relative fits (again, employing a fixed He interaction energy) yield interaction energies whose magnitudes are all decreased by nearly half. A more detailed justification for relation 6.14, as applied to the collisional deactivation of a series of polyatomic species, is currently in preparation [61]. Nevertheless, as highlighted

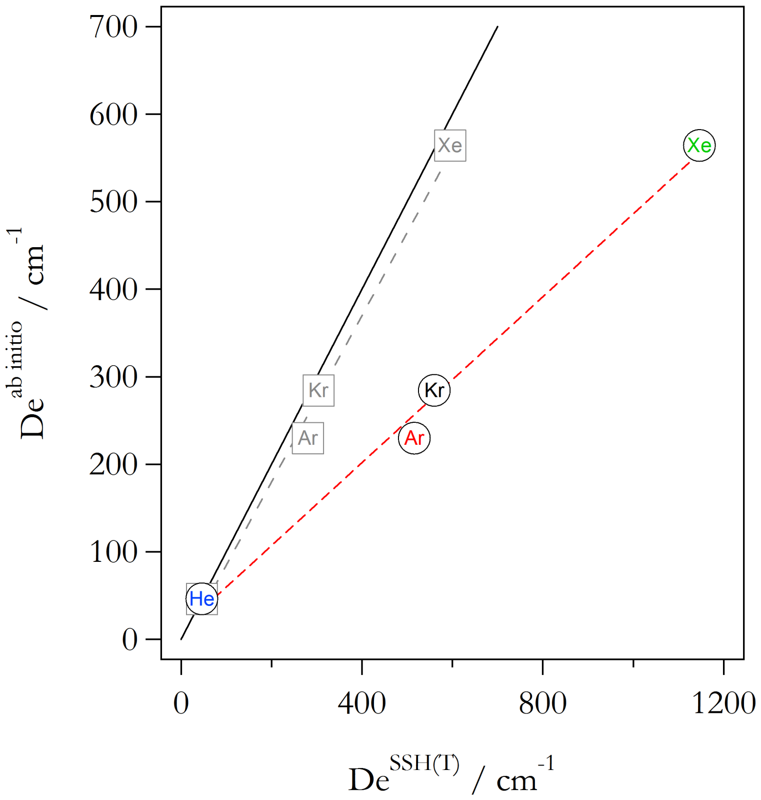

Figure 6.7
Direct comparison of the SSH(T) measured HNC + Rg interaction energies with the ab initio calculated values. The solid black line corresponds to an absolute correlation between theory and experiment. The plot of circles highlights the SSH(T) determined values which employ the classical Tanczos equation where the interaction energy is included via the term {EXP(-De/kT)}. The plot of squares was measured using a modified Tanczos term of the form: {EXP(-2De/kT)}.

in table 6.4 (and figure 6.7), modification of the SSHT attractive interaction term yields experimentally measured interaction energies which are all in near quantitative agreement with the *ab initio* calculated values.

Rg	$\langle\Delta E\rangle$ / EXP	$\langle\Delta E\rangle$ / SSH(T)	Ratio (SSHT / EXP)
He	59.9	651.0	10.9
Ar	40.7	462.9	11.4
Kr	24.0	258.9	10.8
Xe	20.2	220.8	10.9

(*) All $\langle\Delta E\rangle$ values determined at $\langle E\rangle$ = 8,600 cm^{-1}.

Table 6.5
Comparison of the experimentally measured vs. SSH calculated values of $\langle\Delta E\rangle$. It is observed that SSH theory predicts $\langle\Delta E\rangle$ values which are an order of magnitude greater than the experimental measurements.

6.4.3 On the role of polarizability:

As noted above, it is expected that the dominant electrostatic interaction between the HNC molecule and the rare-gas atomic collider is a permanent dipole-induced dipole interaction. Specifically, the potential interaction term should be describable as a function of the product of the permanent dipole moment of the donor molecule with the linear polarizability of the collider atom, as well as inversely proportional to the sixth power of the separation between the two species. If this is in fact the case, both the *ab initio* calculated and SSHT derived interaction energies should scale as linear functions of the atomic polarizabilities. Figure 6.8 highlights a plot of the SSHT derived interaction energies (both the pure result as well as the modification using relation 6.14) as functions of the rare-gas linear atomic polarizabilities. In both instances, a well-behaved linear functional relation is observed, which provides reasonable justification for the dominance of the noted dipole-induced dipole interaction. However, as the sole difference between the pure and modified SSHT values is the magnitude of the interaction energies, the only observed difference is that the slope for the pure SSHT energies is correspondingly larger.

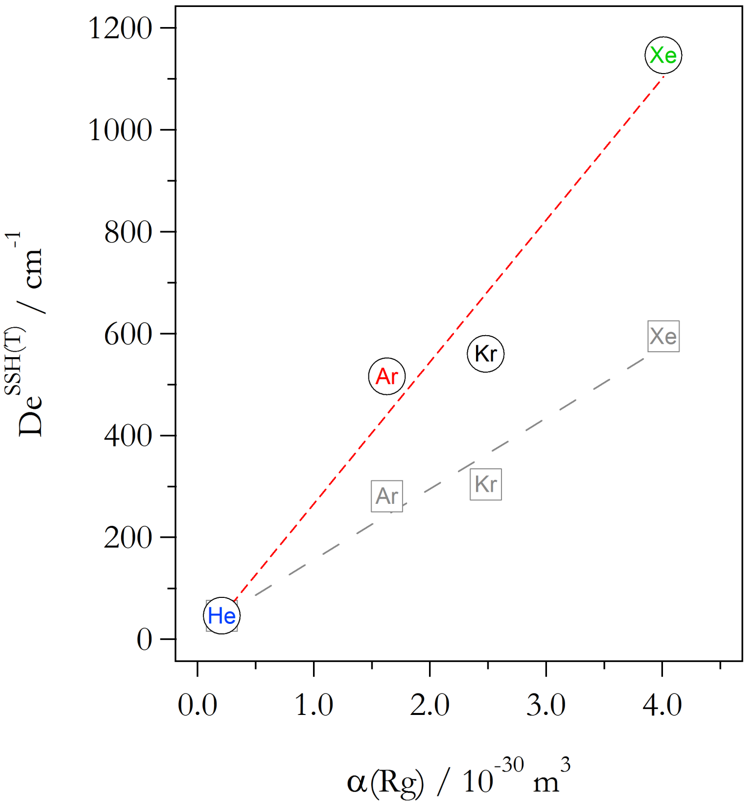

Figure 6.8
Correlation of the SSH(T) measured HNC + Rg interaction energies as a function of the linear polarizabilities of the rare-gas atomic colliders. The circle plot shows the correlation using the classical Tanczos interaction energy equation and the square plot uses the modified (2De) form.

As a result, the observed functional relationship with the atomic polarizabilities cannot be used as a means to argue either for or against the general use of relation 6.14.

Nevertheless, it is of interest to note that the magnitudes of both the calculated *ab initio* and measured SSHT derived $\langle \Delta E \rangle$ values are both observed to decrease for stronger electrostatic interactions (i.e. $\langle \Delta E \rangle_{He} > \langle \Delta E \rangle_{Ar} > \langle \Delta E \rangle_{Kr} > \langle \Delta E \rangle_{Xe}$). The observation of such a relation is contrary to the expectation of a long-lived collision complex. Specifically, given the nature and magnitude of the electrostatic interaction (especially for the larger Rg atoms), the two collision partners could be expected to orbit one another and potentially undergo numerous energy transferring collisions before separating. Under such a scheme, it would be reasonable then to expect that a stronger interaction would hence result in much more efficient energy transfer. As noted however, it is observed that the most efficient (V-T) energy transfer is found for the weakly interacting systems. In this regard then, it is either the case that the true interaction energies are all too weak and hence long-lived collision complexes are simply not forming; or if the energies are sufficiently strong to yield the associated complexes, they are simply not resulting in enhanced energy transfer. In a qualitative sense, such an argument favors the more reasonable (lower magnitude) interaction energies obtained via relation 6.14 by invoking the assumption that complexation is simply unattainable for such weakly interacting systems. Just the same, such a description is ultimately unable to provide a rigorous *ab initio* justification for the suggested modification (relation 6.14) of SSHT theory, but it does nicely showcase the origins of the key intermolecular interaction as a dipole-induced dipole attraction.

6.4.4 Efficient energy transfer:

Vibrational energy transfer has been examined many times before in numerous systems of varying sizes and energetic regimes. It is generally observed that V-T energy transfer is very inefficient, regardless of the average internal energy of the donor species, with average $\langle \Delta E \rangle$ values typically falling well below 10 cm^{-1}. For example, vibrational energy transfer from the series of triatomic species: nitrogen dioxide (NO_2) [23,30,62,63], sulfur dioxide (SO_2) [31,36], as well as carbon disulfide (CS_2) [30,34,35], have all been experimentally examined with a variety of atomic collisional partners. In all three cases examined, minimal $\langle \Delta E \rangle$ values (≤ 10 cm^{-1}) were measured for average energies below the coincident onsets of excited electronic states, even for $\langle E \rangle$ values up to 10,000 cm^{-1}: e.g. $\{NO_2(\tilde{A}^2B_2/\tilde{B}^2B_1)\ \langle E \rangle_0 \approx$ 10,000 / 14,000 cm^{-1}, $SO_2(\tilde{a}^3B_2)\ \langle E \rangle_0 \approx$ 20,000 cm^{-1}, and $CS_2(\tilde{R}^3A_2)\ \langle E \rangle_0 \approx$ 26,000 cm$^{-1}\}$. Once the average internal energy rises above the onsets for the associated lowest excited electronic states, the slopes of the measured $\langle \Delta E \rangle$ vs. $\langle E \rangle$ plots are observed to increase dramatically and adopt new linear trends.

As presented throughout, V-T energy transfer from HNC is found to be an extremely efficient process with $\langle \Delta E \rangle$ values measured well above 10 cm^{-1} for all average energies examined. More specifically, as presented by figure 6.5, enhanced $\langle \Delta E \rangle$ values are observed for all energies with constant linear trends. Based upon the prior triatomic studies listed above, one might be tempted to assert the presence of an extremely low lying excited electronic state which, based upon the observed $\langle \Delta E \rangle = 0$ values, would appear at $\approx$ 3,000 cm^{-1} above the zero point energy of HNC. Nevertheless, the first excited electronic state of HNC ($\tilde{A}^1A''$) is calculated to be 5.8 eV above the zero point level of the ground state [3], well above and beyond the experimentally available internal energy. One alternative possibility could involve coupling to the available ro-vibrational levels of ground state HCN. Given that the zero point energy of HNC lies around 5,000 cm^{-1} above that of HCN [3], there exists a potential for coupling (and hence enhanced energy transfer) for all ground state HNC levels. However, with respect to the numerous theoretical examinations of the HCN / HNC isomerization system, it has been predicted that, for energies less than 11,000 cm^{-1} above the HNC zero point energy, the corresponding wavefunctions will be purely localized in either of the two potential energy wells [4,5]. In other words, for the experimentally allowed HNC internal energies, electronic coupling to HCN should be considered as highly unlikely and therefore should not be viewed as a potential origin of the energy transfer enhancement of HNC.

6.4.5 Astrophysical HNC / HCN abundance ratios:

It has been well established that HCN as well as HNC are both present in the various systems of the interstellar medium [6-11]. Given the presence of ultra-violet (UV) radiation from stars, it is more than reasonable to expect the occurrence of ongoing photochemistry in the variety of astrophysical environments. Specifically, for systems composed of cyano-containing molecules, such as vinyl cyanide, it is quite plausible that photon-induced unimolecular photodissociation will yield vibrationally highly excited HCN and/or HNC. Given that we have already shown that V-T energy transfer from HNC is extremely efficient, compounded by the notion that V-T energy transfer is typically the least efficient process when compared against both vibrational to rotational (V-R) or vibrational to vibrational (V-V) [64], it is likely that both V-R and V-V from HNC will be as efficient (if not more so) than V-T. Furthermore, V-V energy transfer from HCN has already been found to be an efficient process, supposedly due to the presence of a strong permanent dipole moment [1,2]. In this regard then, given that potential astrophysical photochemical systems will be composed of numerous polyatomic species, where in addition to V-T, V-V and V-R will also be possible, it should be expected that any excited HCN / HNC generated should be readily collisionally quenched.

One of the lingering open questions of the astrophysical community pertains to the origin of the comparable HNC / HCN concentrations (measured in the astrophysical medium) for which it was originally expected that HCN should dominate by a factor of around 10^{30} [6-11]. At present, the source of both HCN and HNC is suspected to originate in the electronic dissociative recombination of the $HCNH^+$ ion [12], as isomerization of ground state HCN / HNC is highly unlikely due to the low temperatures of outer space. Given the observation of efficient collisional deactivation of HNC (as well as HCN), in addition to the occurrence of astrophysical photochemistry, the current study provides a provocative alternative origin for the presence of astrophysical HNC as well as the observed abundance ratios. If astrophysical HCN and HNC are both produced predominantly from a single process (i.e. electronic dissociative recombination), it should then be expected that their concentrations would appear in nearly constant ratios, regardless of their physical environment. Alternatively, if the observed isomers originate not from a single process, but rather from general photochemical events involving different cyano-containing species (each of which would necessarily yield HCN and HNC in unique ratios); efficient collisional quenching would provide a means of preserving the nascent abundance ratios. As a result, if collisional deactivation of HNC and HCN are both highly competitive with isomerization, UV photodissociation of various cyano-containing species would necessarily yield variable HNC / HCN abundance ratios, even scenarios in which HNC is more abundant than HCN. Furthermore, as the associated ratios would depend sensitively upon the structure of the given precursor species, they would therefore be completely dependent upon the chemical makeup of the local environment.

6.5 CONCLUSION

We have presented an experimental examination of the V-T energy transfer efficiency of vibrationally highly excited hydrogen isocyanide, collisionally quenched through the rare-gas atomic colliders (He, Ar, Kr, and Xe). A series of time-resolved internal energy distributions were obtained through a modeling of the anharmonic ν_1 NH and ν_3 NC stretch modes, observed in time-resolved emission spectra following the 193 nm photolysis of vinyl cyanide. The average nascent internal energy of HNC was measured to be 24.5 ± 1.4 kcal mole^{-1}, which is in excellent agreement with the value observed in the prior PTS study of Blank et al [28]. The dynamic evolution of the HNC internal energies, as a function of the number of rare-gas collisions, were fit to analytical forms from which the average energy lost per collision (for each inert collider) was determined. It is found that HNC exhibits a well behaved SSH reduced mass trend in which He is observed to be the most efficient quencher, followed by Ar, Kr, and finally Xe. Additionally, it is observed that HNC exhibits uncommonly efficient V-T energy transfer efficiencies in which $\langle \Delta E \rangle > 10\ cm^{-1}$ (up to about 60 cm^{-1} at $\langle E \rangle \approx 9{,}000\ cm^{-1}$) are observed for all internal energies examined. Fitting routines employing vibrational transition probabilities from SSHT theory, showed that the observed reduced mass trend correlates with a monotone increasing interaction energy trend: $|D_e^{He}| < |D_e^{Ar}| < |D_e^{Kr}| < |D_e^{Xe}|$. Furthermore, a slight modification of SSHT theory, in which the attractive energy term is simply doubled, is observed to yield interaction energies which are in near quantitative agreement with *ab initio* calculated values. Moreover, the characterization of efficient collisional deactivation of HNC following the UV photolysis of a cyano-containing species, provides an alternative explanation for the variation of observed abundance ratios of HNC (as compared with HCN) in the astrophysical medium.

Acknowledgement

This work was supported in part by Basic Energy Sciences, U.S. Department of Energy, through Grant No. DEFG 02–86ER 134584.

References:

1. R. Huang, J. Wu, M-. X. Gong, A. Saury, and E. Carrasquillo, *Chem. Phys. Lett.* **216**, 108 (1993).
2. R. Z. Martinez, K. K. Lehmann, and S. Carter, *J. Chem. Phys.* **120**, 691 (2004).
3. B. Gazdy, D. G. Musaev, J. M. Bowman, and K. Morokuma, *Chem. Phys. Lett.* **237**, 27 (1995).
4. Y. Justum, F. Gatti, and X. Chapuisat, *J. Mol. Struct. (Theochem)* **453**, 131 (1998).
5. K. Na, C. Jung, and L. E. Reichl, *J. Chem. Phys.* **125**, 034301 (2006).
6. W. M. Irvine, D. B. Morvan, D. C. Lis, H. E. Matthews, N. Biver, J. Crovisier, J. K. Davies, W. R. F. Dent, D. Gautier, P. D. Godfrey, J. Keene, A. J. Lovell, T. C. Owen, T. G. Phillips, H. Rauer, F. P. Schloerb, M. Seny, and K. Young, *Nature* **383**, 418 (1996).
7. W. M. Irvine, E. A. Bergin, J. E. Dickens, D. Jewitt, A. J. Lovell, H. E. Matthews, F. P. Schloerb, and M. Senay, *Nature* **393**, 547 (1998).
8. W. M. Irvine, J. E.Dickens, A. J. Lovell, F. P. Schloerb, M. Senay, E. A. Bergin, D. Jewitt, and H. E. Matthews, *Faraday Discuss.* **109**, 475 (1998).
9. S. Thorwirth, H. S. P. Muller, F. Lewen, R. Gendriesch, and G. Winnewisser, *A&A* **363**, L37 (2000).

10. P. Schilke, C. Comito, and S. Thorwirth, *ApJ* **582**, L101 (2003).
11. T. Hirota, M. Ikeda, and S. Yamamoto, *ApJ* **594**, 859 (2003).
12. D. Talbi and Y. Ellinger, *Chem. Phys. Lett.* **263**, 385 (1996).
13. R. N. Schwartz, Z. I. Slawsky, and K. F. Herzfeld *J. Chem. Phys.*, **20**, 1591 (1952).
14. D. K. Liu, L. Letendre, and H-.L. Dai, *J. Chem. Phys.* **115**, 1734 (2001).
15. L. Letendre and H-.L. Dai, *J. Phys. Chem. A* **106**, 12035 (2002).
16. G. V. Hartland, W. Xie, D. Qin, and H-.L. Dai, *Rev. Sci. Instrum.* **63**, 3261 (1992).
17. L. Letendre, H-.L. Dai, I. A. McLaren, and T. J. Johnson, *Rev. Sci. Instrum.* **70**, 18 (1999).
18. W. McNavage, W. Dailey, and H-.L. Dai, *Can. J. Chem.* **82**, 925 (2004).
19. M. J. Wilhelm, W. McNavage, R. Groller, and H-.L. Dai, *J. Chem. Phys.* **128**, 064313 (2008).
20. M. J. Wilhelm, M. Nikow, and H-.L. Dai, *J. Mol. Struct.* **883-884**, 242 (2008).
21. L. Letendre and H-. L. Dai, *J. Phys. Chem. A* **106**, 12035 (2002).
22. A. G. Maki, W. Quapp, S. Klee, G. C. Mellau, and S. Albert, *J. Mol. Spectrosc.* **174**, 365 (1995).
23. G. V. Hartland, D. Qin, and H-. L. Dai, *Journal of Chemical Physics* **107**, 2890 (1997).
24. E. B. Wilson, J. C. Decius, and P. C. Cross, *Molecular Vibrations: The Theory of Infrared and Raman Vibrational Spectra* (McGraw-Hill, New York, 1955).

25. R. Zare, *Angular Momentum: Understanding Spatial Aspects in Chemistry and Physics* (Wiley-Interscience, New York, 1988).

26. C. D. Pibel, E. Sirota, J. Brenner, and H-. L. Dai, *Journal of Chemical Physics* **108**, 1297 (1998).

27. A. G. Maki and G. C. Mellau, *J. Mol. Spectrosc.* **206**, 47 (2001).

28. D. A. Blank, A. G. Suits, Y. T. Lee, S. W. North, and G. E. Hall, *J. Chem. Phys.* **108**, 5784 (1998).

29. T. J. Lee and A. P. Rendell, *Chem. Phys. Lett.* **177**, 491 (1991).

30. G. V. Hartland, D. Qin, and H-. L., Dai, *J. Chem. Phys.*, **102**, 8677 (1995).

31. D. Qin, G. V. Hartland, C. L. Chen, and H-. L., Dai, *Z. Phys. Chem.*, **214**, 1501 (2000).

32. M. Zhang (PhD Thesis), Unversity of Pennsylvania (2007).

33. R. G. Hynes and M. G. Sceats, *J. Chem. Phys.*, **91**, 6804 (1989).

34. G. Lendvay and G. C. Schatz, *J. Chem. Phys.*, **98**, 1034 (1993).

35. G. C. Schatz and G. Lendvay, *J. Chem. Phys.*, **106**, 3548 (1997).

36. A. Chimboyo, B. M. Toselli, and J. R. Barker, *J. Chem. Phys.*, **108**, 23836 (1998).

37. S. M. A. Wright, I. R. Sims, and I. W. M. Smith, *Phys. Chem. Chem. Phys.*, **3**, 2203 (2001).

38. P. P. Tennekes, J. Harju, M. Juvela, and L. V. Toth, *A&A* **456**, 1037 (2006).

39. F. I. Tanczos, *J. Chem. Phys.* **25**, 439 (1955).

40. M. J. Frisch *et al.*, GAUSSIAN 03, Revision C.01, Gaussian, Inc., Wallingford, CT, 2004.

41. F-. M. Tao and Y-. K. Pan, *J. Chem. Phys.* **97** 4989, (1992).

42. R. R. Toczylowski, F. Doloresco, and S. M. Cybilski, *J. Chem. Phys.* **114** 851, (2001).

43. S. A. C. McDowell, *Mol. Phys.* **103** 2763, (2005).

44. K. M. Christoffel and J. M. Bowman, *J. Chem. Phys.* **112**, 4496 (2000).

45. S. F. Boys and F. Bernardi, *Mol. Phys.* **19**, 553 (1970).

46. S. Drucker, F-. M. Tao, and W. Klemper, *J. Phys. Chem.* **99**, 2646 (1995).

47. K. Tanaka, S. Bailleux, A. Mizoguchi, K. Harada, T. Baba, I. Ogawa, and M. Shirasaka *J. Chem. Phys.* **113**, 1524 (2000).

48. E. J. Cambell, L. W. Buxton, and A. C. Legon, *J. Chem. Phys.* **78**, 3483 (1983).

49. GAMESS is a package of *ab initio* programs written by M. W. Schmidt, K. K. Baldridge, J. A. Boatz, S. T. Elbert, M. S. Gordon, J. H. Jensen, S. Koseki, N. Matsunaga, K. A. Nguyen, S. J. Su, T. L. Windus, M. Dupuis, J. A. Montgomery, *J. Comp. Chem.* **14**, 1347 (1993).

50. MOLPRO is a package of *ab initio* programs written by H-. J. Werner, P. J. Knowles, R. Lindh, F. R. Manby, M. Schtz, *et al.*, (cf. http://www.molpro.net).

51. J. L. Stretton, *Trans. Faraday Soc.* **61**, 35 (1964).

52. J. T. Yardley, *Introduction to Molecular Energy Transfer, Academic Press, New York, 1980.*

53. D. Rapp and T. Kassal, *Chem. Rev.* **69**, 61 (1969).

54. I. Oref and D. C. Tardy, *Chem. Rev.* **90**, 1407 (1990).

55. G. W. Flynn, C. S. Parmenter, and A. M. Wodtke, *J. Phys. Chem.* **100**, 12817 (1996).

56. B. J. Orr and I. W. M. Smith, *J. Phys. Chem.* **91**, 6106 (1987).

57. J. T. Knudtson and G. W. Flynn, *J. Chem. Phys.* **58**, 1467 (1973).

58. C. N. Xuan, A. Margani, and M. Mastropietro, *J. Chem. Phys.* **106**, 8473 (1997).

59. S. H. Kable and A. E. W. Knight, *J. Phys. Chem. A* **107**, 10813 (2003).

60. M. Nezu, T. Amano, and K. Kawaguchi, *J. Mol. Spec.* **198**, 186 (1999).

61. J. M. Smith, M. J. Wilhelm, M. Nikow, M. Zhang, J. Ma, and H-. L. Dai, *in preparation.*

62. G. V. Hartland, D. Qin, and H-. L. Dai, *J. Chem. Phys.* **100**, 7832 (1994).

63. C. Petrongolo and G. C. Schatz, *J. Chem. Phys.* **112**, 5672 (2000).

64. R. D. Levine, *Molecular Reaction Dynamics*, (Cambridge University Press, Cambridge, 2005).

CHAPTER 7

Conclusions

7.1 SUMMARY

In the preceding chapters, time-resolved Fourier transform infrared emission spectroscopy was employed as a means of characterizing the vibrational energy transfer properties of molecular transients, generated following the 193 nm photolysis of specifically chosen molecular precursors. Along the way, it was determined that two-dimensional correlation analysis [1] was a novel tool capable of enhancing the signal-to-noise ratio (SNR) in a series of time-resolved emission spectra. Specifically, for a repeated series of nearly identical experiments, correlation analysis was found to enhance the common sources of signal while (at the same time) reducing the non-systematic (unique) sources of noise. In particular, correlation analysis was employed in chapters three and four for the purpose of enhancing the SNR of the measured emission spectra of the vibrationally excited ketenyl (HCCO) radical following the 193 nm photolysis of ethyl ethynyl ether.

The enhanced late time spectra, which exhibited partial rotational resolution, lead to the very first experimental determination of the ν_1 CH stretch mode of the ketenyl (HCCO) radical at 3232 cm^{-1}. Additionally, with the aid of anharmonicity constants obtained from an *ab initio* quantum chemical analysis, the early time (high energy) emission spectra of the ν_1 CH stretch mode HCCO were fit and the associated time-resolved average internal energies of HCCO were determined. By careful variation of the corresponding inert collider species, it was thus possible to examine the vibrationally highly excited energy transfer properties of this radical. It was found that, for all internal energies examined, vibrational-to-translational energy transfer from HCCO was extremely efficient, with average energies lost in excess of 50 cm^{-1} for most internal energies. Such a result is highly significant for the field of combustion chemistry given the presence of highly vibrationally excited ground state HCCO following intersystem crossing from an initially prepared population of quartet HCCO [2,3].

Furthermore, our analysis of the 193 nm photodissociation of vinyl cyanide confirmed the generation of hydrogen isocyanide (HNC) as a primary dissociation fragment, in an associated (1 : 3) branching ratio with hydrogen cyanide (HCN). Spectral modeling, along with variation of the employed inert collisional partners, allowed for the first experimental examination of energy transfer from vibrationally highly excited HNC. Comparable to HCCO, energy transfer from HNC was found to be uncharacteristically efficient with average energies lost in excess of 10 cm^{-1} for most internal energies examined. For experimentalists interested in probing general isomerization dynamics, a new and efficient method for generating HNC is just cause for celebration. Additionally, the fact that isolated HNC is generated in quantities comparable to the more stable HCN, compounded by the notion that HNC is readily stabilized through inert collisions, is even more so interesting given that it offers a provocative new solution to the HCN / HNC abundance ratio crisis of the astrophysical community [4]. Furthermore, that a simple modification to the SSH relaxation theory [5] yields quantitatively accurate interaction energies (from TR-FTS measured emission spectra), suggests a new experimental tool for those in the field of weak chemical interactions.

Overall, the recent availability of *ab initio* quantum chemical methods which allow for the routine determination of ro-vibrational anharmonicity constants (χ_{ij}, y_{ijk}, z_{ijkl}, ...) is found to greatly enhance the utility of TR-FTS. Specifically, while the ability to generate and observe highly excited emission from radicals has been around for the last few decades, reasonable means of modeling the observed spectra has generally been elusive. As a direct result, it was often the case that early time (high energy) spectra of radicals simply went un-analyzed [6-9]. Nevertheless, given the advent of this new set of theoretical tools, TR-FTS is now shown to be a capable means of probing energy transfer from vibrationally highly excited radicals.

References:

1. M. J. Wilhelm, M. Nikow, and H. -L. Dai, *J. Mol. Struct.* **883-4**, 242 (2008).
2. D. L. Osborn, D. H. Mordaunt, H. Choi, R. T. Bise, and D. M. Neumark, *J. Chem. Phys.* **106**, 10087 (1997).
3. C-. H. Hu, H. F. Schaefer III, Z. Hou, and K. D. Bayes, *J. Am. Chem. Soc.* **115**, 6904 (1993).
4. D. Talbi and Y. Ellinger, *Chem. Phys. Lett.* **263**, 385 (1996).
5. R. N. Schwartz, Z. I. Slawsky, and K. F. Herzfeld *J. Chem. Phys.* **20**, 1591 (1952).
6. L. Letendre, D. -K. Liu, C. D. Pibel, J. B. Halpern, and H. -L. Dai, *J. Chem. Phys.* **112**, 9209 (2000).
7. L. Letendre and H. -L. Dai, *J. Phys. Chem. A* **106**, 12035 (2002).
8. W. McNavage, W. Dailey, and H. -L. Dai, *Can. J. Chem.* **82**, 925 (2004).
9. M. J. Wilhelm, W. McNavage, R. Groller, and H. -L. Dai, *J. Chem. Phys.* **128**, 064313 (2008).